Pressure-induced second-order phase transition in fluorine

Universidade de Caxias do Sul
Programa de Pós-Graduação em Engenharia e Ciência dos Materiais

Pressure-induced second-order phase transition in fluorine

PhD Thesis

Giovani Luís Rech

July 3, 2023

Caxias do Sul, RS, Brazil

Dados Internacionais de Catalogação na Publicação (CIP)
Universidade de Caxias do Sul
Sistema de Bibliotecas UCS - Processamento Técnico

R296p Rech, Giovani Luís
Pressure-induced second-order phase transition in fluorine [recurso eletrônico] / Giovani Luís Rech. – 2023.
Dados eletrônicos.

Tese (Doutorado) - Universidade de Caxias do Sul, Programa de Pós-Graduação em Engenharia e Ciência dos Materiais, 2023.
Orientação: Cláudio Antônio Perottoni.
Modo de acesso: World Wide Web
Disponível em: https://repositorio.ucs.br

1. Flúor. 2. Física do estado sólido. 3. Estabilidade estrutural. 4. Pressão. I. Perottoni, Cláudio Antônio, orient. II. Título.

CDU 2. ed.: 661.481

Catalogação na fonte elaborada pela(o) bibliotecária(o)
Carolina Machado Quadros - CRB 10/2236

Template

This document was typeset with the help of KOMA-Script and LaTeX using the kaobook class. The credits of this template is due to Federico Marotta and the source code is available at: https://github.com/fmarotta/kaobook

Advisor:	Cláudio Antônio Perottoni

Composition of the Thesis committee:

Altair S. Pereira	Federal University of Rio Grande do Sul
André L. Martinotto	University of Caxias do Sul
Carlos A. Figueroa	University of Caxias do Sul
Felipe H. da Jornada	Stanford University
Naira M. Balzaretti	Federal University of Rio Grande do Sul
Thiago B. da Silva	University of Caxias do Sul

This research was supported by the Brazilian agencies Coordenação de Aperfeiçoamento de Pessoal de Nível Superior - Brasil (CAPES) - Finance Code 001, Programa de Apoio a Núcleos de Excelência (PRONEX), Fundação de Amparo à Pesquisa do Estado do Rio Grande do Sul (FAPERGS) and Conselho Nacional de Desenvolvimento Científico e Tecnológico (CNPq). This research was made possible also thanks to computational resources provided by the Centro de Computação Científica (NCC/GridUNESP), Universidade Estadual de São Paulo (UNESP), Núcleo Avançado de Computação de Alto Desempenho (NACAD) da COPPE, Universidade Federal do Rio de Janeiro (UFRJ), and Centro Nacional de Supercomputação, Universidade Federal do Rio Grande do Sul (CESUP/UFRGS). Thanks are due also to Ney Lemke (Departamento de Física e Biofísica, IBB/UNESP), who granted us access to the NCC/GridUNESP computational resources.

Abstract

The relative stability between the crystal structure of α-F_2, space group $C2/c$, and a hypothesized highpressure phase, space group $Cmce$, was explored using Density Functional Theory at the PBE0+D3(ABC)/TZVP level of theory and further assessed by Quantum Monte Carlo calculations. The analysis of the phonon dispersion spectra reveals that, at ambient pressure, besides the energy difference favoring the $C2/c$ structure, the $Cmce$ phase also presents a dynamical instability near the Γ-point, which disappears with increasing pressure. The unstable vibrational mode can be related to the absence of σ-holes in the fluorine molecule, which renders a repulsive head-to-head interaction between molecules, as opposed to heavier halogens, in which the presence of σ-holes stabilizes the orthogonal $Cmce$ structure. The results show that the pressure-induced phase transition $C2/c \rightarrow Cmce$ is of second-order.

Keywords: fluorine; second-order phase transition; ab initio simulations; solid state physics;

Resumo

A estabilidade relativa entre a estrutura cristalina do α-F_2, grupo espacial $C2/c$, e uma fase hipotética de alta pressão, grupo espacial $Cmce$, foi explorada usando a Teoria da Funcional da Densidade no nível de teoria PBE0+D3(ABC)/TZVP e posteriormente avaliada por meio de cálculos de Monte Carlo Quântico. A análise dos espectros de dispersão de fônons revela que, à pressão ambiente, além da diferença de energia favorecendo a estrutura $C2/c$, a fase $Cmce$ também apresenta uma instabilidade dinâmica próxima ao ponto Γ, que desaparece com o aumento da pressão. O modo vibracional instável pode estar relacionado à ausência de buracos σ na molécula de flúor, o que resulta em uma interação repulsiva cabeça-cabeça entre as moléculas, ao contrário dos halogênios mais pesados, nos quais a presença de buracos σ estabiliza a estrutura ortogonal $Cmce$. Os resultados mostram que a transição de fase induzida pela pressão $C2/c \rightarrow Cmce$ é de segunda ordem.

Keywords: flúor; transição de fase de segunda ordem; simulações ab initio; física do estado sólido;

Aknowlegments

My technical education was shaped by countless hours of studying in a comfortable environment provided to me by my parents, who always created the ideal conditions for me to pursue my passions without worrying about the noise of real-life problems. I want to thank these two incredible people first and foremost, for their unwavering support. However, technical skills gathered through books comprise only a fraction of what makes a human a person. Morals and integrity are taught mainly through example. In this sense, I have always been fortunate to be surrounded by exceptional people from whom I learned to become who I am today. From personal relations and colleagues to teachers and professors.

My mother, Rosmari, has always been my safe haven, the beacon that signals solid ground even amidst chaotic storms. She instilled in me the virtues of maintaining composure and clarity of thought during moments of adversity. And yet, she is one of the kindest and most empathetic people I have ever known. It is from her that I learned the utmost value of Respect, a principle that shall be held at all times, towards everyone. Looking back, I believe that my mother's love of learning, reading, and intellectual pursuits has played a significant role in shaping my own academic passions. I have fond, yet hazy memories of her poring over her philosophy notebooks from university, a sight that has left an indelible impression on my mind.

From my father, Edson, I learned the valuable lesson that being rational and dreaming are not mutually exclusive. He has always maintained a youthful spirit and encouraged me to nurture my curiosity and explore the world around me. As a child, he would allow me to take things apart and conduct experiments, which instilled in me a love for learning and discovery. One of my earliest memories of mathematics is with my father. I remember a late afternoon when we were lying on a bed covered with a yellow and brown quilt. He showed me a right triangle and drew some diagrams on a piece of paper. He then explained to me that the sum of the squares of the two shorter sides is equal to the square of the longest side. Although I didn't comprehend it at the time, I was filled with a sense of curiosity and wonder. It was both exciting and inspiring to know that there were rules governing shapes and that with effort, I could learn and understand them.

Later in life, I met the man who changed my perspective on the world. My husband Isaac showed me how amazing it is to share my life with my best friend. With him, I learned that joy is multiplied and sorrow is divided when shared, a concept that even mathematics cannot fully describe. Isaac is one of those people who radiates joy. Being around him is like finally being able to take a deep breath after a long day. He has shown me a whole new dimension to life and taught me to be a more light-hearted person. He has been and continues to be my rock, the person who never gives up on me, even when I give up on myself. I am eternally grateful for his support through long hours of work and sleepless nights.

Last but not least, in university I met my model of integrity, respect, and professionalism in academia. My advisor Cláudio showed me, through his example, how an incredible professional should

behave, and the ways that a high-level scientist should respect others. His constant pursuit of doing the right thing, either at work or in interpersonal relationships, was a source of inspiration for how I strive to be as a professional. Watching the way in which he can convey complex topics in Thermodynamics and Quantum Mechanics to students, with all the mathematical rigor that these subjects require, in an approachable manner was a memorable experience. His moral fiber is, in my opinion, a reference. Additionally, his attention to detail and adherence to the scientific method always motivated me to do my best. The moments of deep discussion on topics of science and society that we had in the physics laboratory will surely remain forever in my memory.

Agradecimentos

Minha educação técnica foi moldada por inúmeras horas de estudo em um ambiente confortável proporcionado pelos meus pais, que sempre criaram as condições ideais para que eu pudesse seguir minhas paixões sem me preocupar com o ruído dos problemas da vida real. Quero agradecer primeiramente a essas duas pessoas incríveis, pelo seu apoio inabalável. No entanto, as habilidades técnicas adquiridas por meio dos livros compõem apenas uma fração do que torna um ser humano uma pessoa. Valores morais e integridade são ensinados principalmente por meio do exemplo. Nesse sentido, sempre tive a sorte de estar cercado por pessoas excepcionais das quais aprendi a me tornar quem sou hoje. Desde pessoas de relações pessoais e colegas até os professores.

Minha mãe, Rosmari, sempre foi meu refúgio seguro, o farol que sinaliza terreno firme mesmo em meio a tempestades caóticas. Ela me incutiu as virtudes de manter a compostura e a clareza de pensamento durante momentos de adversidade. E ainda assim, ela é uma das pessoas mais amáveis e empáticas que já conheci. É dela que aprendi o valor máximo do respeito, um princípio que deve ser mantido a todo momento, em relação a todos. Olhando para trás, acredito que o amor da minha mãe pelo aprendizado, pela leitura e pelos interesses intelectuais desempenhou um papel significativo na formação das minhas próprias paixões acadêmicas. Tenho lembranças afetuosas, dela folheando seus cadernos de filosofia da universidade, enquanto equilibrava a vida de ser mãe, esposa, trabalhadora e estudante, uma imagem que deixou uma impressão indelével na minha mente.

Com meu pai, Edson, aprendi a valiosa lição de que ser racional e sonhar não são mutuamente exclusivos. Ele sempre manteve um espírito jovial e me incentivou a cultivar minha curiosidade e explorar o mundo ao meu redor. Quando criança, ele me permitia desmontar coisas e realizar experimentos, o que despertou em mim o amor pelo aprendizado e pela descoberta. Uma das minhas primeiras lembranças de matemática é com meu pai. Lembro-me de uma tarde quando estávamos deitados em uma cama coberta por uma manta de quadrados amarelos e marrons. Ele me mostrou um triângulo retângulo e desenhou alguns diagramas em um pedaço de papel. Em seguida, ele me explicou que a soma dos quadrados dos dois catetos é igual ao quadrado da hipotenusa. Embora eu não tenha compreendido na época, fiquei cheio de curiosidade e admiração. Foi emocionante e inspirador saber que existiam regras que governavam as formas geométricas e que, com esforço, eu poderia aprendê-las e entendê-las.

Mais tarde na vida, conheci o homem que mudou minha perspectiva sobre o mundo. Meu marido, Isaac, me mostrou como é incrível compartilhar minha vida com meu melhor amigo. Com ele, aprendi que, quando compartilhadas, a alegria é multiplicada e a tristeza é dividida, um conceito que talvez nem a matemática possa descrever completamente. Isaac é uma daquelas pessoas que irradia alegria. Estar perto dele é como finalmente conseguir respirar fundo depois de um longo dia. Ele me mostrou uma dimensão completamente nova da vida e me ensinou a ser uma pessoa mais leve. Ele tem sido e continua sendo meu alicerce, a pessoa que nunca desiste de mim, mesmo

quando eu desisto de mim mesmo. Sou eternamente grato por seu apoio durante longas horas de trabalho e noites sem dormir.

Por último, mas não menos importante, na universidade conheci meu modelo de integridade, respeito e profissionalismo no meio acadêmico. Meu orientador Cláudio me mostrou, por meio de seu exemplo, como um profissional incrível deve se comportar e as maneiras pelas quais um cientista de alto nível deve respeitar os outros. Sua busca constante por fazer a coisa certa, seja no trabalho ou nos relacionamentos interpessoais, foi uma fonte de inspiração para como eu me esforço para ser como profissional. Observar a maneira como ele consegue transmitir tópicos complexos em Termodinâmica e Mecânica Quântica, com todo o rigor matemático que essas disciplinas exigem, de forma acessível aos estudantes foi uma experiência memorável. Sua integridade moral é, na minha opinião, uma referência. Além disso, sua atenção aos detalhes e adesão ao método científico sempre me motivaram a fazer o meu melhor. Os momentos de discussão profunda sobre temas de ciência e sociedade que tivemos no laboratório de física certamente permanecerão para sempre em minha memória.

Prologue

Amidst my wandering thoughts, darkness engulfs me.

Suddenly, I hear hastened footsteps reverberating in what seems to be a subterranean chamber. When my eyes open, I perceive an aged stone ceiling and a man busily pacing around in the chilly, decrepit room. He is rummaging through heaps of books and tools, collecting a few items. So focused is he that he scarcely notices my awakening.

"Good, you have awakened!" exclaimed the lean man, sporting a conical hat and circular glasses resting upon a sagacious face. His voice was tranquil, uncharacteristic of his energetic movements. *"Have you not heard? The beast has reawakened! Let us move!"* he adds, visibly perturbed.

Bewildered and sensing the urgency of the situation, I hastily rise to my feet, my eyes striving to bring everything into focus. The chamber, circular in shape, is filled with a biting chill and stagnant air. Bubbling jars and peculiar instruments everywhere. At the heart of the chamber lies an immense desk, forged from solid steel and burdened with an array of books and parchment filled with intricate equations. A fine assortment of quills and ink bottles adorns its surface. Adjacent to the desk, a great blackboard bears cryptic symbols, diagrams, and formulae. It is certainly a laboratory. With his lengthy cloak sweeping the stone floor, he admonishes me to follow him.

"Hurry, we have much work and scarce time. This beast is no easy foe", he says, darting between cabinets.

"What must we do?" I inquire.

"We must understand it better. For decades, all have left it to slumber, fearing it. But now, we have no other choice," he replies.

"Very well, but how?" I ask, searching for something to combat this beast. As I approach a corner to retrieve some old, dusty swords, he halts me.

"No, no, no, my dear friend. This beast cannot be defeated with common tools. We require a different tactic. This thing is small but dangerous, for everything it touches bursts into flames," he warns. The man is still focused on gathering his belongings, mostly books, and other unknown objects. He enlists my aid.

"Come, help me with these things. We must utilize all the resources at our disposal. Please grab this crate," he instructs, handing me a wooden container filled with bell-shaped objects crafted from iridescent glass. Inscribed on the side of the crate is the word "Basis."

I stand there, attempting to comprehend the situation. The man reaches for a large jar atop a shelf and mutters to himself,

"I shall take these functional herbs. Hopefully, the hybrid ones will suffice." He seizes the container brimming with dried roots, labeled "Hybrid PeeBeeYee roots."

With the jar tucked under one arm and a stack of books under the other, he strides toward the ponderous wooden door. He glances at me before opening it.

"Are you coming or not?" he queries impatiently. Still reeling from the unexpected events, I hasten after him, clutching the bell-shaped objects. Doubt momentarily seizes me, and I pause to inquire,

"What is this beast called?"

The man, already outside and hastening down the corridor, yells back,

"It is called fluorine!"

Published works

G. L. Rech, A. L. Martinotto, J. E. Zorzi, and C. A. Perottoni. 'Pressure-induced second-order phase transition in fluorine'. In: *Physical Chemistry Chemical Physics* 25 (2023), pp. 9935–9943. DOI: 10.1039/D2CP05635F.

Abstract: The relative stability between the crystal structure of α-F_2, space group $C2/c$, and a hypothesized high-pressure phase, space group $Cmce$, was explored using Density Functional Theory at the PBE0+D3(ABC)/TVZP level of theory and further assessed by Quantum Monte Carlo calculations. The analysis of the phonon dispersion spectra reveals that, at ambient pressure, besides the energy difference favoring the $C2/c$ structure, the $Cmce$ phase also presents a dynamical instability near the Γ-point, which disappears with increasing pressure. The unstable vibrational mode can be related to the absence of σ-holes in the fluorine molecule, which renders a repulsive head-to-head interaction between molecules, as opposed to heavier halogens, in which the presence of σ-holes stabilizes the orthogonal $Cmce$ structure. The results show that the pressure-induced phase transition $C2/c \rightarrow Cmce$ is of second-order.

J. Ben, A.L. Martinotto, G.L. Rech, J.E. Zorzi, and C.A. Perottoni. 'Thermal expansion of continuous random networks of carbon'. In: *Journal of Non-Crystalline Solids* 576 (2022), p. 121260. DOI: 10.1016/j.jnoncrysol.2021.121260.

Abstract: Homogeneous and isotropic continuous random networks (CRNs) of carbon were created spanning a large portion of hybridization space, from sp^3-rich configurations up to 70% sp^2 carbon. For each of these CRNs, the volumetric coefficient of thermal expansion (CTE) was calculated according to the quasi-harmonic approximation using the Brenner potential. The CTE of H-free, sp^3-rich CRNs is similar to that of diamond and almost constant up to about 50% sp^2-C. The CTE at 300 K varies from about $3.5\times10^{-6}K^{-1}$ to $5.5\times10^{-6}K^{-1}$, linearly increasing with the sp^2-C content for CRNs above ca. 40% sp^2-C, in good agreement with previous experimental studies. A small fraction of 10% to 15% of the CRNs, irrespective of composition, exhibit volumetric negative thermal expansion (NTE) over a limited temperature range around 100 K to 200 K.

L.M. Leidens, D. Matté, G.L. Rech, J.E. Zorzi, A.F. Michels, F. Alvarez, C.A. Perottoni, and C.A. Figueroa. 'Different desorption rates prompting an indirect isotopic effect on nanoscale friction'. In: *Applied Surface Science Advances* 7 (2022), p. 100201. DOI: https://doi.org/10.1016/j.apsadv.2021.100201.

Abstract: Friction behavior at the nanoscale may be split into different contributions, including phononic dissipation. Despite the isotopic effect in the phononic component being previously explored, experimental and theoretical approaches determined contradictory conclusions. Here, a desorption-based model is proposed, and it is found to be consistent with previously published experimental data on hydrogenated and/or deuterated amorphous carbon films. Moreover, molecular dynamics simulations showed that a surface coverage difference as low as 5% might promote an effect on friction even greater than that observed experimentally. This happens when reactive defects are created after desorption (prompting carbon dangling bonds), reinforcing the assumption that minor surface differences may be sufficient for the effects observed,

meeting both experimental and theoretical approaches in the same overall trend. Therefore, the phononic dissipation occurs, but the isotopic effect may be indirect, where the desorption rate of hydrogen and deuterium plays a role by exposing carbon dangling bonds, changing the interface of interaction and the nanoscale friction ultimately.

D. Cassol, G. L. Rech, E. Thomazi, C. A. Perottoni, and J. E. Zorzi. 'Influence of an over calcined calcium oxide-based shrinkage-compensating admixture on some properties of a self-compacting concrete'. In: *Matéria (Rio de Janeiro)* 27 (2022). DOI: 10.1590/1517-7076-RMAT-2022-0171.

Abstract: The demand for self-compacting concrete grows continuously due to investments in new infrastructure, upgrades, or replacement of old infrastructure. This type of concrete can mold itself into the spaces intended for it on its own and fill them without the need for any vibration or external compaction. It must achieve three main properties: fluidity, passing ability, and resistance to segregation. Monitoring these properties, the quality, and the increase in the performance of concrete structures is essential to keep up with this growth. In this work, we explore the effect of adding a commercial over calcined calcium oxide-based compound, as a shrinkage-compensating admixture, on the properties of fresh and hardened concrete, particularly on the shrinkage and curing of self-compacting concrete specimens (SCC). Also, an experimental protocol is proposed for the electrical impedance analysis of concrete samples. Fluidity, compression, shrinkage, elastic modulus, and impedance spectroscopy tests were performed, in addition to scanning electron microscopy images. The additive slightly modifies the concrete properties in the fresh state. In hardened concrete, the compressive strength and modulus of elasticity increase, in addition to a reduction in shrinkage with 2.8% of the additive.

G. L. Rech, A. L. Martinotto, N. M. Balzaretti, and C. A. Perottoni. 'Fitting of interatomic potentials by a differential evolution algorithm'. In: *Computational Materials Science* 187 (2021), p. 109929. DOI: 10.1016/j.commatsci.2020.109929.

Abstract: Computer simulation has been increasingly present in the discovery and understanding of materials structure and properties. First-principles simulations, in particular, allow to meaningfully explore the material world without having to resource to experimental methods. Even though their extreme usefulness, first-principle methods tend to be very computer-intensive to the point of being impractical in many situations that are important for the understanding of materials' behavior. As an alternative, computer simulations can be carried out using interatomic potentials (IPs), in which case an analytic mathematical model for the energy of the system is fitted to a set of crystal structure parameters and experimentally determined physical properties by minimizing a cost function. How close the properties calculated using an IP can get of those experimentally determined is limited both by its analytic form and the model's parameters. For compounds with different atomic species, the multidimensional parameter space of the cost function most possibly exhibit a very complex landscape. In these cases, global minimization methods are often required. This work explores the use of a differential evolution (DE) algorithm for the parametrization of IPs for two compounds, namely berlinite ($AlPO_4$) and zirconium tungstate (α-ZrW_2O_8). Several analytic interatomic potentials (including some previously proposed in the literature) were fitted to experimental lattice parameters, atomic positions, and elastic constants. Two-dimensional mappings of the interatomic potential parameters reveal the complex landscape of the cost function for berlinite and α-ZrW_2O_8, which exhibits several local minima, broad plateaus, discontinuities, and, in some cases, strong correlations between

fitting parameters. The differential evolution algorithm was able to navigate the cost function landscape and, giving a sufficiently large population, was capable to found good candidates for the global minimum, despite all the mentioned difficulties. In all cases here explored, the interatomic potentials re-parametrized using DE yield calculated athermal properties in better agreement with the experimental observables as compared to previous results from the literature.

D. Matté, G.L. Rech, L.M. Leidens, J.E. Zorzi, A.F. Michels, C.A. Figueroa, and C.A. Perottoni. 'Molecular dynamics simulations of the isotopic effect on nanoscale friction'. In: *Applied Physics A* 127.9 (2021), p. 657. DOI: 10.1007/s00339-021-04803-3.

Abstract: Computer simulations are becoming increasingly useful for studying friction, enabling the application of controlled conditions and setups that are not usually achievable in physical experiments and ensuring that no other undesirable variable is acting on the system. In this work, molecular dynamics (MD) simulations were used to systematically explore the isotope's mass effect on the phononic contribution to friction by simulating different load conditions, sliding direction, and surface coverage of H-passivated flat [111] single-crystal diamond surfaces. Simulations were performed using the Adaptive Intermolecular Reactive Empirical Bond-Order (AIREBO) potential, including van der Waals interactions. The coefficient of friction was found to be independent of the adsorbate atomic mass for both sliding directions simulated. Furthermore, at least in the simulated conditions, a simple reduction in surface coverage also did not significantly affect the coefficient of friction. A marked increase of friction force was observed only when the passivation layer was modified by introducing highly reactive defects. Accordingly, the results from MD simulations give support to an indirect isotopic effect on friction, but only to the extent that defects created in the passivation layer lead to the formation of highly reactive surfaces.

G. L. Rech and C. A. Perottoni. 'Density functional theory plane-wave/pseudopotential calculations of the equation of state of rhenium in the terapascal regime'. In: *Journal of Physics: Conference Series* 1609.1 (2020), p. 012014. DOI: 10.1088/1742-6596/1609/1/012014.

Abstract: The equation of state (EOS) of hexagonal close-packed rhenium has been previously determined up to 1.5 TPa ($V/V_0 = 0.46$) using all-electron (AE) density functional theory (DFT) including core relativistic effects [Phys. Rev. B 100, 174107 (2019)]. This work focuses on assessing the validity of pseudopotentials at such high-pressures, above 1 terapascal (TPa), by comparing the EOS obtained using plane-wave/pseudopotentials (PW/PPs) with previous AE calculations. Both ONCV pseudopotentials tested (PBE and PBEsol) yield results in good agreement with all-electron calculations. The fitted parameters of the Rose-Vinet EOS, the bulk modulus, B_0 (380(2) GPa and 379(3) GPa for the PBE and PBEsol PPs), and its pressure derivative, B'_0(4.58(2) and 4.59(3) for the PBE and PBEsol PPs), are in good agreement with previous all-electron results ($B_0 = 367(5)$ GPa and $B'_0 = 4.64(3)$). The agreement is worse for the equilibrium volume at zero pressure, V_0 (199.9(2) Bohr3 and 199.2(2) Bohr^3 for PBE and PBEsol PPs, versus 196.7(3) Bohr^3 for AE). Even so, for a given V/V_0 ratio, the pressures estimated using the EOS derived from the PPs and AE calculations are in very good agreement, thus suggesting that the PPs used in this study are valid even at such high compression regime.

G. L. Rech, J. E. Zorzi, and C. A. Perottoni. 'Equation of state of hexagonal-close-packed rhenium in the terapascal regime'. In: *Physical Review B* 100.17 (2019), p. 174107. DOI: 10.1103/PhysRevB.100.174107.

Abstract: All-electron density functional theory calculations were performed aiming to determine the equation of state and the dependence with pressure of the c/a ratio and the anisotropic compressibility for hexagonal-close-packed rhenium. Calculations were carried out up to maximum compression of 0.46, and the resulting total energy versus volume is well described by a Vinet equation of state with $B_0 = 367(5)$ GPa and $B_0' = 4.64(3)$, valid up to 1.5 TPa. The agreement with two recent experimental studies [S. Anzellini et al., Equation of state of rhenium and application for ultra high pressure calibration, J. Appl. Phys. 115, 043511 (2014); T. Sakai et al., High pressure generation using double-stage diamond anvil technique: Problems and equations of state of rhenium, High Pressure Res. 38, 107 (2018)] supports their conclusion that the pressure in previous experiments with a double-stage diamond-anvil cell [L. Dubrovinsky et al., Implementation of micro-ball nanodiamond anvils for high-pressure studies above 6 Mbar, Nat. Commun. 3, 1163 (2012)] was significantly overestimated.

Contents

List of Figures

List of Tables

1 Introduction*

The study of fluorine compounds dates back at least to the early 16th century when the mineral fluorite (Figure 1.1) was described by the German physician and mineralogist Georgius Agricola [9, 10]. Crude hydrofluoric acid was first prepared in the mid-18th century. An almost anhydrous acid was prepared in 1809, and two years later, the French physicist Andre-Marie Ampère suggested that it was a hydrogen compound with an unknown element, analogous to chlorine, for which he suggested the name of fluorine [9, 10]. Even though the existence of this element was well known for many years after that, all attempts to isolate it were unsuccessful and even lethal for some of the chemists who pursued element number 9. Fluorine isolation did not occur until 1886 when the French chemist Ferdinand Frederick Henri Moissan separated the element by electrolysis [9, 11, 12]. Due to its extreme reactivity, isolation of fluorine only occurred 112 years after chlorine isolation by Scheele and about 70 years after the preparation of elemental bromine and iodine [12]. The 1906 Nobel Prize in Chemistry was awarded to Henri Moissan *"in recognition of the great services rendered by him in his investigation and isolation of the element fluorine, and for the adoption in the service of science of the electric furnace called after him"* [13].

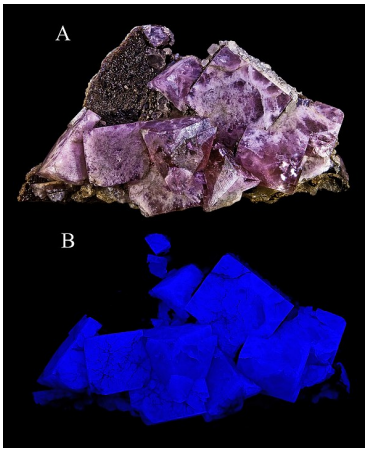

Figure 1.1: Fluorescing fluorite from Boltsburn Mine, Weardale, North Pennines, County Durham, England, UK. (A) under white light and (B) under UV light.
By Didier Descouens - Own work, CC BY-SA 4.0, https://commons.wikimedia.org/w/index.php?curid=7528654

Fluorine forms diatomic molecules (F_2) and is in a gaseous state at room temperature and pressure. At ambient pressure, fluorine

* Ferdinand Frederick Henri Moissan next to the electric furnace of his own design.

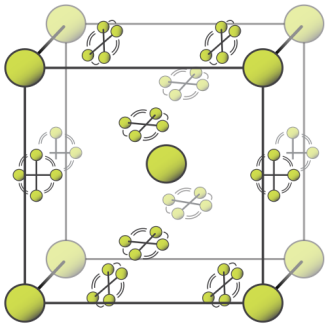

Figure 1.2: Crystalline structure of beta fluorine. The diatomic molecules at the corners and center of the cubic unit cell rotate freely while the molecules on the faces of the cube rotate confined on a plane perpendicular to the face of the unit cell.

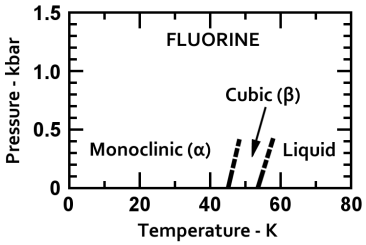

Figure 1.3: Phase diagram of fluorine published in 1975 [20].

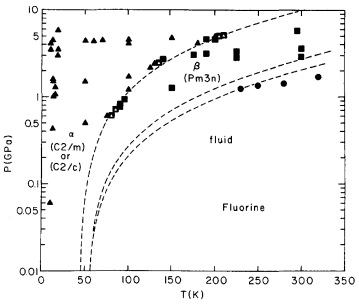

Figure 1.4: Phase diagram of F_2. (△) α-F_2; (□) β-F_2; (combined △ and □) α-β two-phase region; (●) fluid. Dashed lines represent Simon equation fits to the transition lines. Taken from [19]

condenses in a bright yellow liquid at 85 K [9, 14] and solidifies at 53.5 K forming a cubic structure called β-fluorine [15]. This phase is transparent and soft, with a significant molecular disorder. The proposed space group was assumed to be $Pm3n$, although data analysis suggests space group $P\bar{4}3n$ as a possible alternative. There are eight fluorine molecules per unit cell which are in constant rotations around their center of mass, as depicted in Figure 1.2. In the paper in which the crystal structure of β-F_2 was proposed from X-ray diffraction data, the authors comment on the difficulty of the experiment. In their words, the diffraction pattern was *"obtained from one very good single crystal grown with considerable difficulty from one of the best samples"*[15]. This phrase illustrates the hardship which is characteristic of experimental studies with fluorine. At that time, fluorine was the only stable element without a known crystal structure.

At 45.6 K and ambient pressure, fluorine transforms from cubic β-F_2 to a low-temperature monoclinic phase (α-F_2), space group C2/c, with four F_2 molecules per unit cell [16]. This phase is opaque and hard, with layers of fluorine molecules almost in hexagonal close-packing. This solid-solid transition is highly energetic, which caused all the experimental endeavors even more complex. The first determination of the crystal structure of the alpha phase was only possible after a 24h passivation process of the copper sample holder. This avoided *"the earlier difficulties with explosions occurring when solid samples were being cooled through the transition at 45 K"*. A second difficulty was observed when trying to make a fine powder for diffraction from the samples of the alpha phase, as *"any attempt to crush it when in the α form caused an explosion"*[17]. The experimental results revealed that the α phase belonged to the $C2/m$ space group, although $C2/c$ was also a possible space group. A few years later, Pauling supported the $C2/c$ space group by reanalyzing the same experimental data [18]. Investigating elemental fluorine in experiments is particularly challenging due to its high reactivity and low atomic number. For many years, this was basically everything known about the solid phases of fluorine, seen by the phase diagram of fluorine from 1975 in Figure 1.3. In 1987, a Raman study by Schiferl et al. expanded the phase diagram of fluorine up to 6 GPa, whose results can be seen in Figure 1.4 [19].

Both α- and β-fluorine are formed by weakly interacting F_2 molecules. The α-F_2 phase is remarkable for assuming a space

group different from all the other halogens, whose structures belong to the orthorhombic $Cmce$[1] space group [17]. Heavier halogen atoms possess an anisotropic electrostatic potential, a direct consequence of the electron deficiency of the p_z orbital. When a σ bond is formed, a region of positive electrostatic potential appears on the other hemisphere of the atom, called the σ-hole. The positive σ-hole will then interact with negative regions of neighboring molecules [21]. Chlorine, bromine, and iodine assume a structure in which the diatomic molecules arrange themselves in zig-zag chains, mainly stabilized by σ-holes interacting with nearby molecules, counteracting electronic repulsion and originating a slightly more compact crystalline structure. The σ-hole in chlorine, bromine and iodine calculated using the M06-L functional with a LANL2DZdp ECP basis set in the Gaussian09 package is shown in Figure 1.5.

1: The group $Cmca$ (N. 64) was relabeled $Cmce$ in the fourth edition of the International Tables of Crystallography

The σ-hole interaction is much weaker (or even absent) in fluorine, and repulsion is stronger thus making the $C2/c$ more stable for avoiding head-to-head interactions between the diatomic molecules [23], as shown in Figure 1.6. Furthermore, both structures are related by a shear strain along the a axis.

A delicate balance exists between the different energy contributions when comparing the structures with $Cmce$ and $C2/c$ space groups. Results from periodic linear scaling, local second-order Møller–Plesset perturbation theory (p-LMP2) calculations, including ZPE corrections and correlation effects (the latter estimated using the method of increments), suggest that the electrostatic and exchange interactions sum up to a less repulsive cohesive energy in the $C2/c$ structure [23]. On the other hand, correlation interactions go in the opposing direction, making a less repulsive contribution to the $Cmce$ phase. Lastly, the ZPE is lower in the $C2/c$ phase, and the net difference in internal energy between the two phases was reported to amount to only 124 μE_h/atom at zero temperature and pressure [23]. Such a slight difference in energy, added to the fact that the $Cmce$ phase is slightly more compact, makes it reasonable to hypothesize a pressure-induced $C2/c \rightarrow Cmce$ phase transition.

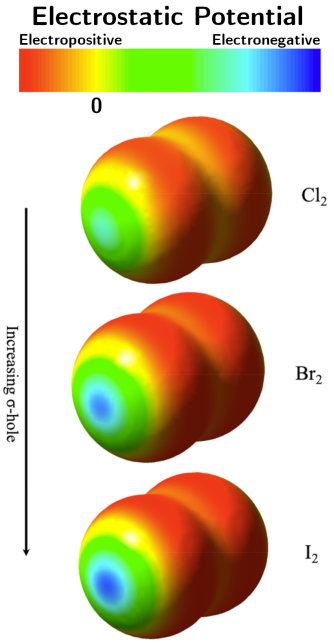

Figure 1.5: Electrostatic potential surfaces mapped onto total electron density for the chlorine, bromine, and iodine diatomic molecules. Adapted from [22]

The transition from α-F_2, $C2/c$ space group, to a high-pressure phase with the $Cmce$ space group, isotypical of the other halogens, has never been observed experimentally. The previously mentioned Raman study found no evidence of a pressure-induced

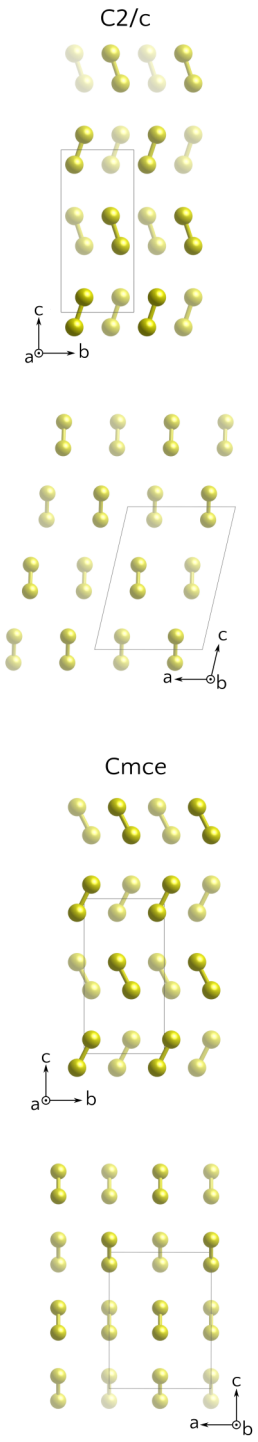

Figure 1.6: Comparison between the crystalline structures of α-F2, space group C2/c, the hypothetic high-pressure phase, space group Cmce. The parallelograms indicate the conventional unit cell. The C2/c structure avoids the head-to-head interaction between the molecules and is related to the Cmce structure by a shear strain along the *a* axis. We have used light shade to convey depth.

phase transition, even though they were particularly interested in observing a phase of $Cmce$ space group. In Schiferl et al.'s words, *"The F_2 vibron shows no anomalous behavior, and F_2 does not go to the typical $Cmce$ halogen crystal structure"*.

Computationally, the $Cmce$ structure shows up recurrently in structure search studies as the stable phase in high pressure and the $C2/c \rightarrow Cmce$ transition pressure estimates vary from 5 up to 70 GPa. The transition from α-F_2 to a high-pressure phase was first investigated using Density Functional Theory (DFT) and a structure-search algorithm by Lv et al[24]. The study successfully confirms the thermodynamically stable $C2/c$ phase at low-pressure, which is more likely the space group for fluorine compared to $C2/m$, especially considering the observed dynamical instability in the calculated phonon spectra of the $C2/m$ structure. At around 8 GPa, C2/c transforms to a high-pressure $Cmce$ phase, remaining stable up to 100 GPa. The electronic band structures and density of states indicate that both $C2/c$ and $Cmce$ are insulators. The nonmetallic property of $Cmce$ fluorine stands in stark contrast to other halogen crystals that possess this space group structure. For instance, pressure-induced metallization occurs in $Cmce$ iodine at 20.6 GPa[25], and molecular $Cmce$ bromine undergoes an insulator-to-metal transition with band overlap at 55 GPa. Even so, the band gap in solid fluorine decreases with pressure, indicating that a transition from an insulator to a metal might be its final fate at high enough pressures. It is worth mentioning that this fluorine study employed the PBE exchange-correlation functional, which is not the best choice for determining the band gap in solids. However, considering that the estimated values are well above 2 eV and the PBE functional is known to underestimate the band gap[26], we have strong indications that fluorine is an insulator in a large range of pressures.

More recently, Olson et al. used a search algorithm that incorporates symmetry and geometric constraints to search for new structures of chlorine and fluorine [27]. Even though their work mainly focuses on chlorine, they found $Cmce$ fluorine becomes stable at 70 GPa, a pressure much higher than Lv et al. suggested. This work, which also employs the PBE XC functional, predicts that the $Cmce$ phase is stable and an insulator up to 2.5 TPa, after which fluorine transitions to a metallic phase of $P4_2/mmc$ space group. For much higher pressures, at 30 TPa, not even fluorine can escape the final destiny of all elements to become an atomic phase. Interestingly,

this final phase, space group $Fddd$, as well as some intermediate phases, seem to become superconductors at temperatures of a few kelvins above 1 [28].

A third estimate for the pressure of transition was placed at 5 GPa in a computational study that employed the SCAN-rVV10 exchange-correlation potential [29]. This work presents particularly bold claims about the nature of the $C2/c$ and $Cmce$ phases of fluorine, such as that, albeit being molecular solids, both phases are metallic, even at ambient pressure, and that increasing pressure induces the formation of σ-holes in the fluorine's molecules. The metallic nature, i.e. non zero electronic density of states at the Fermi level, of this molecular crystal in this latter work seems quite strange and this odd result was not particularly addressed by the authors.

In none of the studies previously mentioned has the nature of the $C2/c \rightarrow Cmce$ transition been explored in greater detail, which is what this work proposes to do.

Two of the works mentioned above employed the Perdew–Burke-Ernzerhof (PBE) exchange-correlation functional in their DFT calculations, with no account for dispersion energy contributions, whereas the third applies the SCAN+rVV10 exchange-correlation functional. Despite the much higher computational cost, we chose the hybrid functional PBE0 (including a contribution from an exact Hartree-Fock exchange term) to investigate the $C2/c \rightarrow Cmce$ phase transition in fluorine, as it has been successfully used in the computer investigation of fluorine before [30]. In this functional, 25% of the exchange energy is calculated exactly using Hartree–Fock theory. Furthermore, a computationally efficient way to account for the missing long-range correlation interactions in standard DFT is to add, a *posteriori*, an energy dispersive term that is dependent solely on the interatomic distances. Grimme's DFT-D3 is one of these methods, which includes dipole-dipole, dipoles-quadrupoles, and three-body dipolar Van der Waals interactions in an expression with fixed empirical dispersion coefficients [31]. The combination of dispersion corrections and this hybrid functional has shown a good trade-off between accuracy and performance [32]. An additional step towards including correlation effects in first-principles calculations of solids is to resort to Quantum Monte Carlo (QMC) methods [33, 34]. Diffusion Monte Carlo (DMC), in particular, has been shown to be well suited to classifying

different polymorphs of molecular crystals according to their relative stability [35, 36].

In this work, hybrid functional DFT calculations is applied to solid molecular fluorine at zero pressure and temperature to assess the relative stability of these two candidate structures, which is further checked by DMC calculations. Finally, the nature of a possible pressure-induced phase transition between these two structures is explored using group-theoretical tools and DFT calculations.

Theoretical Digression

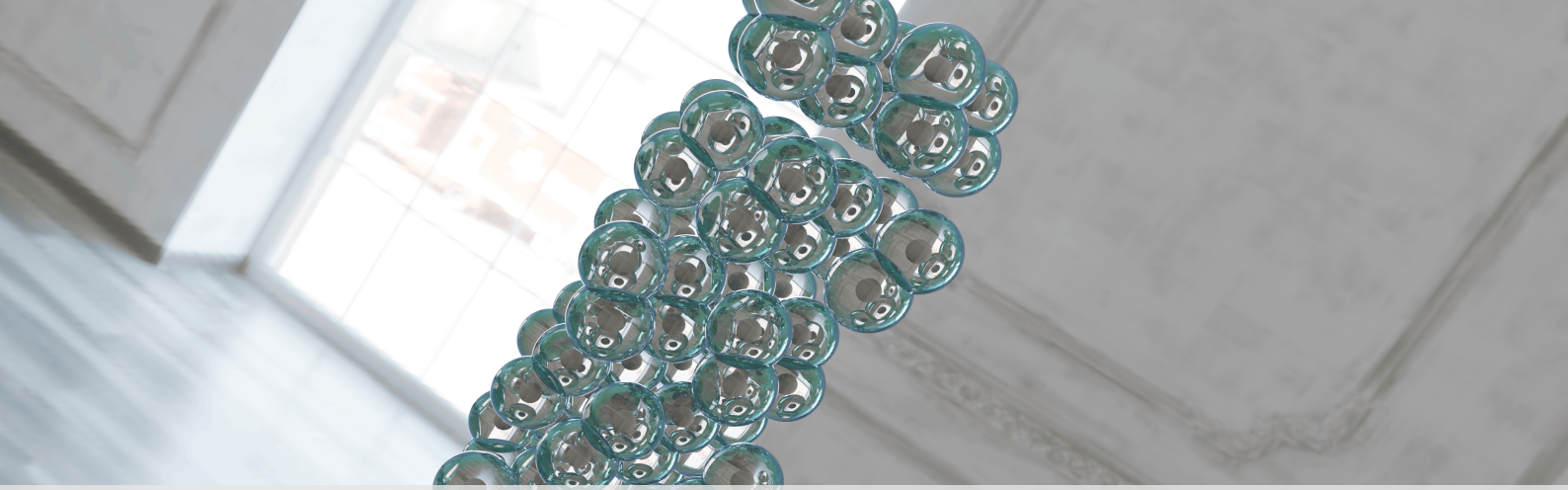

2 Setting the stage

Already know the mathematics? No problem!

The part titled "Theoretical Digression" offers a summary of the formalisms utilized in this study and is optional for those who are already familiar with it.

We start with the foundational postulate of quantum mechanics, which states that a wavefunction, denoted as Ψ, exists for any (chemical) system. By applying appropriate operators to Ψ, we can obtain the observable properties of the system. The Schrödinger equation is the cornerstone of theoretical chemistry, where an operator acts on Ψ to yield the system's energy, denoted as E. This equation can be expressed as an eigenvalue equation:

$$\hat{H}\Psi = E\Psi \tag{2.1}$$

where $\hat{H}$ is the Hamiltonian operator, Ψ is the wave function (eigenfunction for a given Hamiltonian) and E is the energy of the system. The typical form of the Hamiltonian operator considers five contributions to a system's total energy: the kinetic energies of the electrons and nuclei, the attraction of the electrons to the nuclei, the repulsion between nuclei, and the repulsion between electrons. In more complicated situations such as an external electric or magnetic field, considering the relativistic effects, etc., other terms are required in the Hamiltonian. So, the Hamiltonian can be expressed in atomic units as;

Atomic units

Atomic units are a system of natural units frequently employed in *ab initio* simulations of materials including electronic structure calculations. They are designed to simplify the equations and expressions used in these calculations by setting fundamental physical constants to unity. In atomic units, the electron mass (m_e), the electron charge (e), the reduced Planck constant ($\hbar$), and the Bohr radius (a_0) are all equal to 1. Then, the Coulomb constant ($\frac{1}{4\pi\epsilon_0}$) also becomes 1, and we define the unit for the energy, called Hartree ($E_h = \frac{\hbar^2}{m_e a_0^2}$). Consequently, the equations describing the behavior of electrons and nuclei become much simpler.

Biased notation

The notation $\Psi(x)$ is biased towards the position representation of the wavefunction. The wavefunction should be thought of as a property of the system that can assume several representations expressed as functions over different scalar fields, such as position (and spin), momentum, and even energy. None of these representations carry more or less information. The use of Dirac notation might reduce this bias, in which the wavefunction is written as the ket vector $|\Psi\rangle$. A great and concise formalism of quantum mechanics that praises the use of Dirac's notation can be found in the lectures notes of Professor R.G. Littlejohn [37]

$$H = -\sum_{i=1} \frac{1}{2}\nabla_i^2 - \sum_A \frac{1}{2M_A}\nabla_A^2 - \sum_i \sum_A \frac{Z_A}{r_{i,A}} + \sum_i \sum_{j>i} \frac{1}{r_{i,j}} + \sum_A \sum_{B>A} \frac{Z_A Z_B}{r_{A,B}} \tag{2.2}$$

The above equation is in atomic units for simplicity. Its terms represent the kinetic energy of electrons, the kinetic energy of nuclei, the coulomb attraction between electrons and nuclei, repulsion between electrons, and repulsion between nuclei, respectively. The indices i and j run over the electrons, and A and B run over the nuclei. The wave function Ψ describes the system and takes as variables the coordinates in configuration space x of N electrons and M nuclei in the system, leading to the following equation:

$$\hat{H}\Psi(x_i, \ldots, x_N, x_A, \ldots, x_M) = E\Psi(x_i, \ldots, x_N, x_A, \ldots, x_M) \tag{2.3}$$

1: The mass of hydrogen's nucleus is 2000 times greater than the mass of the electron

At this point, we may introduce our first approximation. Nuclei have a mass much larger than the mass of the electron[1]. As such, we may regard the second term of the Hamiltonian as negligible. This is called the Born-Oppenheimer approximation, in which the electrons, being much lighter than the nuclei, are assumed to adjust instantaneously to the nuclear positions. This assumption enables the decoupling of the electronic and nuclear Schrödinger equations. The electronic wavefunction is then solved within the fixed nuclear framework, which originates the external potential. Furthermore, by assuming that the positions of the nuclei do not change, the last term of the Hamiltonian (2.2) becomes a constant and might be disregarded as well (a constant added to an operator will have no practical effect other than to add a shift to all energy values). Under this approximation, the Schrödinger equation takes the form

$$\hat{H}\Psi(x_i, \ldots, x_N) = E\Psi(x_i, \ldots, x_N) \tag{2.4}$$

with the Hamiltonian

$$H = -\sum_{i=1} \frac{1}{2}\nabla_i^2 - \sum_i \sum_A \frac{Z_A}{r_{i,A}} + \sum_i \sum_{j>i} \frac{1}{r_{i,j}} \tag{2.5}$$

and the nuclear positions are simply parameters of the equations.

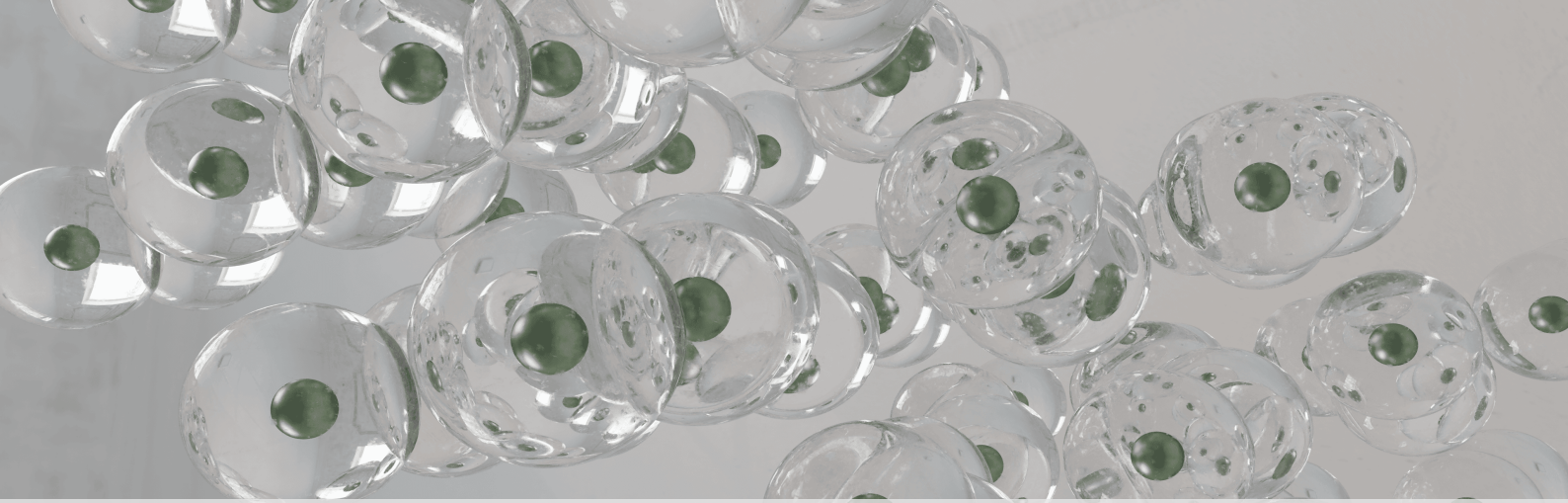

3 The Hartree-Fock method

The primary objective of the Hartree-Fock method is to solve the electronic Schrödinger equation to understand the electronic behavior of a system and determine its ground-state wavefunction and energy. This is achieved by expressing the Hamiltonian as a sum of single-particle operators known as the Fock Hamiltonian H_F:

$$H = \sum_i H_F(x_i) \tag{3.1}$$

In equation (2.5), the first and second terms are already in the form of single-particle operators. However, the last term involves interactions between all electrons and is more challenging to handle. To address this, instead of computing individual electron-electron repulsion terms, we introduce an effective potential, denoted as V^{HF} or the Hartree-Fock potential, which takes into account the repulsion experienced by the electron i due to the presence of all the other electrons:

$$H_F = -\frac{1}{2}\nabla_i^2 - \sum_A \frac{Z_A}{r_{i,A}} + V_i^{HF} \tag{3.2}$$

By employing the Fock operator, we can decompose the unsolvable many-body electronic Schrödinger equation into a set of solvable one-electron equations.

$$H_F \chi_i = \epsilon_i \chi_i \tag{3.3}$$

Here, χ_i represents single-particle wavefunctions, also known as spin-orbitals or atomic orbitals, which depend on the three spatial components and a spin component. Further discussion on the Hartree-Fock potential will be provided later. The motivation behind this decomposition is to express the overall wavefunction Ψ as a product of individual single-particle wavefunctions:

$$\Psi(x_1, x_2, \ldots, x_N) = \chi_1(x_1)\chi_2(x_2)\cdots\chi_N(x_N) \tag{3.4}$$

Although this form is convenient, it fails to satisfy the antisymmetry principle, which is a fundamental requirement for describing fermions. According to this principle, the wavefunction of fermions should exhibit antisymmetry upon interchanging any set of space-spin coordinates. In the context of electrons, the coordinates x_i represent the configuration space, encompassing the three spatial coordinates and the spin. The spin of an electron can assume two distinct eigenvalues: -1/2 and +1/2, corresponding to the alignment of the spin relative to an arbitrary axis. These two spin types are commonly denoted as α (+1/2) and β (-1/2) spins, respectively. Furthermore, they are orthonormalized, which means their inner product is zero when the spins are different and equal to one when they are the same. The typical form of a spin-orbital is a product involving a spatial orbital, denoted as $\phi(r_i)$, and the spin function denoted as σ. This can be expressed as:

$$\chi(x_i) = \phi(r_i)\sigma \tag{3.5}$$

where r_i denotes the spatial coordinates. In order to comply with the antisymmetry principle, we need that

$$\Psi(x_1, \ldots, x_i, x_j, \ldots, x_N) = -\Psi(x_1, \ldots, x_j, x_i, \ldots, x_N \tag{3.6}$$

To fulfill these requirements, we can employ specific linear combinations of Hartree products. It is important to note that if a

wavefunction is valid, its linear combinations are also valid. Let us consider a two-electron system as an example. If electron one occupies the χ_i spin-orbital and electron two occupies the χ_j spin-orbital, we have:

$$\Psi(x_1, x_2) = \chi_i(x_1)\chi_j(x_2) \tag{3.7}$$

and, on changing the electrons

$$\Psi(x_2, x_1) = \chi_i(x_2)\chi_j(x_1) \tag{3.8}$$

To meet the antisymmetry requirement, we can construct a linear combination of these trial wavefunctions:

$$\Psi(x_1, x_2) = \frac{1}{\sqrt{2}}\left[\chi_i(x_1)\chi_j(x_2) - \chi_i(x_2)\chi_j(x_1)\right] \tag{3.9}$$

where the coefficient $\frac{1}{\sqrt{2}}$ serves as a normalization factor. It is worth noting that exchanging the electrons results in a sign change of the wavefunction. This combination can be represented as a determinant:

$$\Psi(x_1, x_2) = \frac{1}{\sqrt{2}}\begin{vmatrix}\chi_1(x_1) & \chi_2(x_1)\\ \chi_1(x_2) & \chi_2(x_2)\end{vmatrix} \tag{3.10}$$

Generalizing to N electrons we arrive at what is called the Slater determinant

$$\Psi(x_1, x_2, \ldots, x_N) = \frac{1}{\sqrt{N!}}\begin{vmatrix}\chi_1(x_1) & \chi_2(x_1) & \cdots & \chi_N(x_1)\\ \chi_1(x_2) & \chi_2(x_2) & \cdots & \chi_N(x_2)\\ \vdots & \vdots & \ddots & \vdots\\ \chi_1(x_N) & \chi_2(x_N) & \cdots & \chi_N(x_N)\end{vmatrix}, \tag{3.11}$$

Slater determinants offer a convenient approach for constructing wavefunctions using single-particle orbitals. This is due to a key property of determinants: the interchanging of two rows in the determinant matrix leads to a sign change. In this context, each row corresponds to an electron, and each column represents a spin-orbital.

The Hartree product represents a wavefunction where the electrons are completely uncorrelated, while the anti-symmetrized Slater determinant introduces a type of correlation among the electrons. This quantum mechanical phenomenon, called the "exchange" interaction, arises from the process of antisymmetrization and will contribute to the total energy of the system. Another important aspect of expressing electrons in orbitals using Slater determinants arises when we attempt to place two electrons in the same orbital simultaneously (i.e. $\chi_1 = \chi_2$). In such a case, two columns of the determinant matrix become identical. A fundamental property of determinants is that when this occurs, the determinant becomes zero, resulting in $\Psi(x_1, x_2) = 0$. This phenomenon corresponds to the Pauli exclusion principle.

The Hartree-Fock method makes an assumption that the behavior of electrons can be described by a Slater determinant. This assumption implies that each electron moves independently of all others, except for the Coulomb repulsion it experiences due to the average positions of all electrons. In the Hamiltonian, the Coulombic repulsion is incorporated through the Hartree potential, which consists of two components:

$$V^{HF}(x_1) = \sum_{j}^{N} \left(\hat{J}_j(x_1) - \hat{K}_j(x_1) \right) \tag{3.12}$$

The first component, denoted as $\hat{J}$, is known as the Coulomb operator. It can be expressed as follows:

$$\hat{J}_j(x_1) = \int \left| \chi_j(x_2) \right|^2 \frac{1}{r_{12}} \mathrm{d}x_2 \tag{3.13}$$

This term represents the average local potential at position x_1, resulting from the charge distribution of the electron in the orbital

χ_j. It is important to note that we sum over all the other orbitals. Sometimes, this first term is referred to as single-electron integrals. The second component of V^{HF} accounts for the exchange contribution and is purely a quantum mechanical effect. It can be defined in terms of its action on a spin-orbital [1]. Mathematically, it is given by:

1: The Coulomb term also acts on a spin-orbital, but we can omit χ_i in the operator expression because we do not integrate over its coordinates.

$$\hat{K}_j(x_1)\chi_i(x_1) = \int \chi_j^*(x_2)\frac{1}{r_{12}}\chi_i(x_2)\mathrm{d}x_2\chi_j(x_1) \tag{3.14}$$

The exchange operator, also referred to as bi-electronic integrals, accounts for the correlation between electrons due to their indistinguishability and the quantum mechanical requirement of antisymmetry for the total wave function of a many-electron system. It describes the effect of swapping the positions of two electrons and measures the change in the electronic energy resulting from this swap.

In summary, the Hartree-Fock method assumes the independence of electron motion while incorporating the Coulomb repulsion through the Hartree potential, which consists of the Coulomb operator $\hat{J}$ and the exchange term $\hat{K}$. The Coulomb operator describes the average local potential resulting from the charge distribution of electrons, while the exchange term accounts for the quantum mechanical effect of electron exchange, reflecting the indistinguishability of electrons and the requirement of antisymmetry in the wave function.

So, as we see, the Hartee-Fock potential is dependent on the spin-orbital which, in turn, needs V^{HF} to be calculated. This is solved iteratively by an initial guess for the potential, from which we calculate the spin-orbitals and obtain a new Hartree-Fock potential. This is repeated until convergence. This approach is called a Self-Consistent Field calculation and it is also used in Density Functional Theory.

One-electron Hamiltonian

The one-electron Hamiltonian is an operator that gathers only the operations related to a single electron in the Fock Hamiltonian

$$\hat{h} = -\frac{1}{2}\nabla_i^2 - \sum_A \frac{Z_A}{r_{i,A}}$$

We can express the Fock Hamiltonian in equation (3.2) in an alternative form, using a one-electron Hamiltonian denoted as $\hat{h}$ and incorporating the Hartree-Fock potential, which comprises the Coulomb and exchange operators. The resulting expression

is

$$\left[\hat{h}(x_1) + \sum_{j \neq i} \hat{J}_j(x_1) - \hat{K}_j(x_1)\right] \chi_i(x_1) = \epsilon_i \chi_i(x_1) \tag{3.15}$$

It is worth noting that upon realizing that

$$\left[\hat{J}_i(x_1) - \hat{K}_i(x_1)\right] \chi_i(x_1) = 0 \tag{3.16}$$

we can simplify the expression further to obtain

$$\left[\hat{h}(x_1) + \sum_{j} \hat{J}_j(x_1) - \hat{K}_j(x_1)\right] \chi_i(x_1) = \epsilon_i \chi_i(x_1) \tag{3.17}$$

The Variational Method

The variational method is an approach used to approximate the ground state wavefunction of a quantum mechanical system. It involves constructing a trial wavefunction that depends on a set of parameters, and then minimizing the energy of the system with respect to these parameters. The principle behind the variational method states that the energy of the trial wavefunction will always be greater than or equal to the true ground state energy. By optimizing the parameters, typically the spin-orbitals, the variational method allows us to approximate the ground state wavefunction within the constraints of the Hartree-Fock approximation.

This form is commonly used to represent the Hartree-Fock equations. To approximate the ground-state wavefunction, we solve these equations using the variational method. By finding the energy at which the minimized eigenvalue corresponds to the ground state, we obtain the ground-state Hartree-Fock wavefunction. The energy is obtained by calculating the expectation value of the Hamiltonian.

In conclusion, it is important to acknowledge the various approximations made in the Hartree-Fock method. First, the Born-Oppenheimer approximation is employed, assuming negligible nuclear motion compared to electrons due to the vast mass difference. Second, we have not addressed relativistic effects, which become more significant for heavier atoms but are generally less relevant for lighter elements like fluorine. Third, we assume the availability of a complete representation of spin-orbitals, although in practice, these functions are often expressed as finite linear combinations of basis functions (more details on this will be discussed later on Chapter 5).

Fourth, the restriction to wavefunctions generated by a Slater determinant should be noted. In the original quantum mechanical problem, the goal is to find the wavefunction that describes the system's ground state, possessing the minimum energy among all possible wavefunctions. In the Hartree-Fock theory, however, we seek the wavefunction of minimum energy within the subset that can be described by a Slater determinant. Consequently, the

Hartree-Fock ground-state wavefunction will not be identical to the true ground-state wavefunction.

Fifth, an important approximation is the omission of the Coulomb correlation. The energy contribution of the Coulomb correlation, often referred to as "electronic correlation", is sometimes defined to be the difference between the actual total energy and the energy of the Hartree-Fock solution. This effect, which arises from the collective influence of all electrons on the motion of a single electron, contributes only about 1% to the total energy, but plays a crucial role in capturing phenomena like London dispersion, which hold particular significance in molecular crystals. Nevertheless, there are several methods that build upon the Hartree-Fock solution to account for the electronic correlation. These methods are collectively called post-Hartree-Fock methods and include Quantum Monte Carlo, Configuration Interaction, Møller–Plesset perturbation theory, among others.

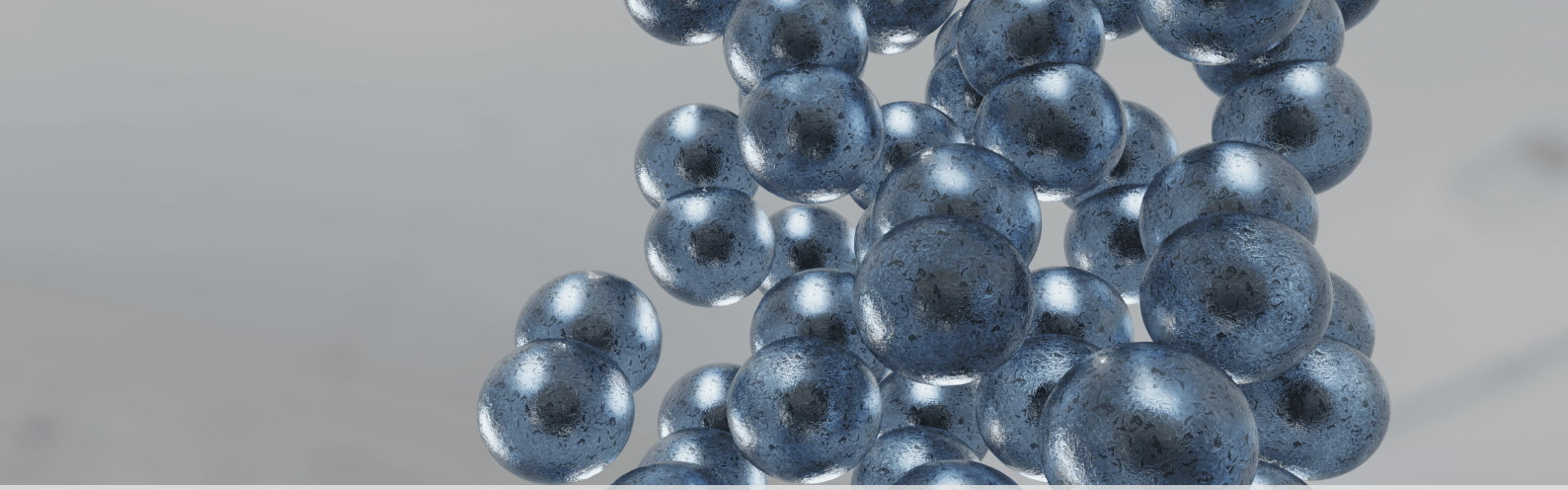

4 Density Functional Theory

Density Functional Theory (DFT) is a powerful theoretical framework in quantum mechanics used to study the electronic structure of many-body systems. It has become a popular method in various fields of physics, chemistry, and materials science, as it allows for accurate and efficient calculations of the electronic properties of molecules, solids, and nanostructures.

The wavefunction

$$\Psi(\mathbf{x}_1, \cdots, \mathbf{x}_N) : \mathbb{R}^{3N} \mapsto \mathbb{C}$$

where $\mathbf{x}_i$ is the three-component spatial position of electron i, and N is the number of electrons in the system.

General quantum mechanics presents a direct map between the wavefunction and the energy of a system. The properties, given as derivatives of the energy, are, therefore, also mapped from the wavefunction. In fact, the wavefunction can be thought of as this mathematical object that contains everything that there is to know about the system (although its physical interpretation is still debatable). The wavefunction Ψ is a complex-valued function over all the possible positions of the electrons in the system $\mathbb{R}^{3N}$, where N is the number of electrons in the system, and the 3 comes from the three spatial coordinates. So, the wavefunction takes the $3N$ spatial position variables and maps them to a unique complex number.

The electron density

$$\rho(\mathbf{r}) : \mathbb{R}^3 \mapsto \mathbb{R}$$

where $\mathbf{r}$ is the coordinates of a point in space.

The fundamental concept in DFT is the electron density, which is a key quantity that characterizes the electronic structure of a system. The electron density is a function of only three spatial coordinates that maps to a real number. Unlike traditional wavefunction-based methods, such as Hartree-Fock theory, DFT does not explicitly compute the many-electron wavefunction, but instead focuses on the electron density as the fundamental variable. The central idea is that the ground-state energy of a system can be determined solely by the electron density, bypassing the need to calculate the full many-electron wavefunction. In a way, it tries to find the same answer by asking a different question. The equivalence between

solving the many-body problem to the electron density is assured by the Hohenberg-Kohn theorems, explained below. This was a huge discovery that opened the gates for the quantum description of systems much larger than the ones that could be described by other methods.

4.1 The First Hohenberg-Kohn Theorem

The first Hohenberg-Kohn theorem establishes a one-to-one correspondence between the external potential of a many-electron system and its ground-state electron density. Formally, the theorem states:

Theorem 4.1.1 (First Hohenberg-Kohn Theorem) *For a given external potential $V_{ext}(\mathbf{r})$ that confines the electrons in a many-electron system, there exists a unique ground-state electron density $\rho(\mathbf{r})$ that minimizes the total energy of the system.*

The external potential represents the influence of external forces or fields acting on the electrons in a many-electron system. It arises from the interaction of the electrons with their surroundings, such as, but not limited to, an external electric field generated by the atoms' nuclei in a molecule, or crystal lattice in a solid. It affects the behavior and arrangement of electrons within the system, influencing their energy levels and spatial distribution.

In practical terms, the external potential can be described as a scalar function of position $V_{ext}(\mathbf{r})$, where $\mathbf{r}$ represents the spatial coordinates. This potential accounts for the average interaction of the electrons with the external environment and is typically treated as an input parameter in DFT calculations. The electrons in the system respond to the external potential by rearranging themselves to attain a state of minimum energy.

If we think of the electron density as a property of the system, it is not surprising that there's a map between each possible external potential to a wavefunction. And from each possible wavefunction to an electron density. The other way around, however counter-intuitive, is also true. The first Hohenberg-Kohn (HK) theorem, first formulated by P. Hohenberg and W. Kohn in 1964, states that a ground-state electron density is uniquely mapped to a single wavefunction and a uniquely defined external potential (and the

ground-state energy of the system) [38]. Since there is a one-to-one correspondence $V_{ext} \leftrightarrow \Psi \leftrightarrow \rho$, we can construct a direct map between V_{ext} andρ. Compared to the wavefunction, the electron density is a much simpler mathematical object that maps only three spatial variables (a point in space) to a real number. The beauty of this approach is that despite being much simpler, the electron density contains all the information needed to describe the ground-state properties of a many-electron system, just like the wavefunction.

This direct mapping between the wavefunction and the electron density also allows for the expression of any property, traditionally described as an expectation value $\langle \Psi | \hat{O} | \Psi \rangle$ involving operators and the many-body wavefunction, as a functional of the electron density $O\left[\rho(\mathbf{r})\right]$. In DFT, each observable property corresponds to a functional that, given the ground-state electron density as input, provides the value of that property as an output.

Not the first use of the electron density!

Since the early 1920s, the Thomas-Fermi theory has been used as an approximation to calculate electronic energy based on electron density distributions. However, its application in chemistry and materials science was limited due to its inability to accurately predict chemical bonding. Nonetheless, the theory considered interactions between electrons in an external potential and established an implicit relationship between this potential and the electron density. Although the theory provided a rough solution to the many-electron Schrödinger equation, it remained unclear whether there was a direct connection between the theory and whether knowledge of the ground-state density alone could uniquely determine the system. This mystery was finally resolved by Hohenberg and Kohn. Their proof is remarkably simple, almost trivial, which raises the question of why it took approximately 40 years from the time Thomas and Fermi first utilized density as a fundamental variable before their approach was firmly grounded in physics. [39].

4.2 The Second Hohenberg-Kohn Theorem

The second Hohenberg-Kohn theorem takes us a step closer to a more practical approach to Density Functional Theory. It reveals a significant aspect of the functional that yields the total energy. The theorem states:

Theorem 4.2.1 (Second Hohenberg-Kohn Theorem) *The unique functional that returns the ground-state total energy when applied to the ground-state density, returns a higher value for any other density.*

This theorem implies a systematic procedure for determining the ground-state density by minimizing the total energy functional. Consequently, given an external potential V_{ext}, such as a crystalline atomic arrangement, the ground-state energy $E_0[V_{\text{ext}}]$ is minimized by the true ground-state electron density $\rho(r)$ of the system. The true ground-state energy is, then, a functional of the electron density, written as

$$E_0 = E_0[V_{\text{ext}}] = \min_{\rho(r)} E_0[\rho(r)] \tag{4.1}$$

where the minimization is taken over all possible electron densities ρ that are normalized to the total number of electrons:

$$\int \rho(\mathbf{r}) d\mathbf{r} = N, \tag{4.2}$$

This allows us to calculate the ground-state energy by minimizing the total energy functional with respect to the electron density.

One may question, as I did, the necessity of a formalism for the second theorem, as it appears to be a consequence of the first theorem. The first theorem ensures that for any electron density that is given as input to the energy functional, we obtain a unique value for the energy. Furthermore, it guarantees that only the specific ground-state electron density yields that particular value for the ground-state energy. However, it does not provide information on how the functional values vary with different densities. By itself, the first theorem allows the possibility that another electron density, not the ground-state density, could generate a functional value lower than that produced by the ground-state density. The second theorem reassures us that the minimum value of the functional is obtained only when the ground-state density is used, thereby making the energy obtained by the minimization of the functional the ground-state energy of the system. Consequently, the second Hohenberg-Kohn theorem indicates that once the minimum of the energy functional is found, the ground-state electron density has been determined.

4.3 The Kohn-Sham Equations

Although the HK theorems provide a theoretical foundation for DFT, it does not provide a practical way to compute the electron density $\rho(r)$ for a given system. To make DFT practical, the Kohn-Sham (KS) equations were introduced by W. Kohn and L. J. Sham in 1965 [40]. The KS equations are a set of equations that translates the original many-electron problem onto a electron density formed by a system of non-interacting electrons moving in an effective potential. The KS equations consist of two parts: the first part involves solving for a set of one-electron wavefunctions, called the KS orbitals, that reproduce the electron density of the system, and the second part involves solving for the effective potential that is consistent with the KS orbitals.

The KS orbitals are obtained by solving the following set of eigenvalue equations:

$$\hat{H}_{\mathrm{KS}}\psi_i(\mathbf{r}) = \epsilon_i\psi_i(\mathbf{r}) \tag{4.3}$$

where $\psi_i(\mathbf{r})$ represents the ith KS orbital, ϵ_i represents the corresponding KS energy, and $\hat{H}_{\mathrm{KS}}$ is called the Kohn-Sham Hamiltonian. And from the KS orbitals, the electron density is given by:

$$\rho(\mathbf{r}) = \sum_{i=1}^{N} |\psi_i(\mathbf{r})|^2 \tag{4.4}$$

1: The Born-Oppenheimer approximation has been made.

The missing element is the Kohn-Sham Hamiltonian, which in atomic units is given by [1]:

$$H_{KS} = T + V_{\mathrm{Hartree}} + V_{\mathrm{ext}} + V_{\mathrm{XC}} \tag{4.5}$$

$$= \nabla^2 + \int \frac{\rho(\mathbf{r}')}{|\mathbf{r} - \mathbf{r}'|}\mathrm{d}\mathbf{r}' + \sum_{I=1}^{N} \frac{Z_I}{|\mathbf{r} - \mathbf{R}_I|} + \frac{\partial E_{\mathrm{XC}}\,[\rho]}{\partial \rho} \tag{4.6}$$

Don't get confused with terms!

The set of KS orbitals ψ_i is often called the "wavefunction" in the context of DFT computing codes. This is not the wavefunction Ψ that we get from the Schrödinger equation and may be viewed here simply as a mathematical tool that bear no physical meaning. KS orbitals only represent a noninteracting reference system which has the same electron density as the real interacting system. That being said, there are cases where the KS orbitals resemble the Hartree-Fock orbitals (which do have physical meaning) and might be a good basis for qualitative interpretation of molecular orbitals [41].

where the first term is the kinetic energy, the second term also called the Hartree potential, represents the classical Coulomb interaction with the electron density, the third term represents the external potential originating from the N nuclei, and the fourth term represents the exchange-correlation (XC) potential. The first, second and third terms represent contributions of a single particle to the energy, and many-body and correlation contributions in both the kinetic energy and Hartree energy are included in the exchange-correlation energy. This way, this formalism presents an exact translation of the Born-Oppenheimer many-body problem to the electron density problem.

The XC functional E_{XC} is the most important and challenging part of DFT, as it accounts for the many-body effects of electron-electron interactions. The exact form of $E_{\mathrm{xc}}[\rho(\mathbf{r})]$ is unknown and must be approximated in practical DFT calculations.

4.4 Self-Consistent Field calculations

At this point, one may have noticed that the Hamiltonian depends on the electron density, which in turn is obtained from the KS orbitals calculated using this same Hamiltonian. This interdependence is solved in a self-consistent manner, in what is called a Self Consistent Field (SCF) calculation. The general recipe for this is presented in Figure 4.1 and works as follows:

1. Choose an initial guess for the electron density (often taken as the density of a related system or a superposition of atomic densities).
2. Use the chosen density to construct the Kohn-Sham Hamiltonian.
3. Solve the Kohn-Sham equations, which are a set of eigenvalue equations for a set of single-particle orbitals. These equations incorporate the exchange-correlation potential, which describes the interactions between the electrons.
4. The solutions of the Kohn-Sham equations give a set of

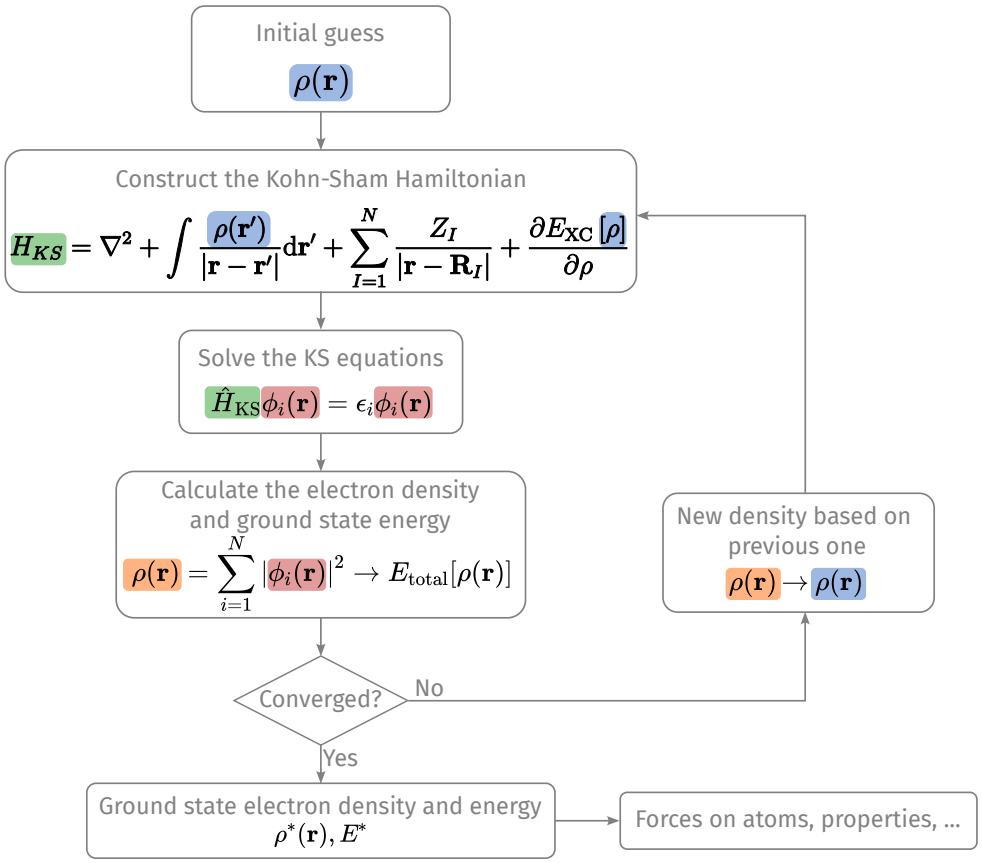

Figure 4.1: Diagram presenting the Self Consistent Field calculation in Density Functional Theory.

eigenvalues and eigenfunctions. These eigenvalues represent the energy levels of the electrons, and the eigenfunctions are the wavefunctions of the electrons in the system.

5. Use the eigenfunctions to calculate a new electron density.
6. Compare the new electron density with the previous guess. If they are not the same within a chosen tolerance, update the guess by mixing the previous guess and the new density. The mixing parameter is typically chosen to be small to ensure convergence.
7. Repeat steps 2-6 until the electron density converges to a self-consistent solution.

Convergence is typically determined by a threshold for the change in the density between iterations (a change in energy and forces between iterations). Once the self-consistent electron density has been obtained, various properties of the system can be calculated, such as the total energy, electron density distribution, forces on atoms, and the electronic structure. The practical implementation of DFT requires the discretization of the Kohn-Sham equations on a grid or in a basis set, depending on the chosen numerical approach. The choice of grid or basis set, as well as the convergence criteria for self-consistency, can affect the accuracy and efficiency of DFT calculations.

This KS approach has become the most widely used method in DFT and has enabled calculations of electronic properties of systems ranging from atoms and molecules to solids and surfaces.

4.5 The Exchange-Correlation Functional

The XC functional $E_{\text{xc}}[\rho(\mathbf{r})]$ in Equation 4.6 is the most important and challenging part of DFT, as it accounts for the many-body effects of electron-electron interactions. However, the exact form of $E_{\text{xc}}[\rho(\mathbf{r})]$ is unknown and must be approximated in practical DFT calculations.

There are various approximations that are commonly used in DFT to approximate the XC functional. The most widely used approximation is the Local Density Approximation (LDA), which assumes that the XC energy per electron at a given point in space depends only on the electron density at that point, and is the same as that of a homogeneous electron gas with the same density

[40, 42]. The LDA has been found to be reasonably accurate for many systems, especially for systems with slowly varying electron densities.

Another commonly used approximation is the Generalized Gradient Approximation (GGA), which takes into account not only the electron density at a point, but also the gradient of the electron density, to approximate the XC energy per electron [43]. The GGA provides a more accurate description of the XC effects compared to LDA, and it has been widely used in many DFT calculations.

In addition to LDA and GGA, there are many other more sophisticated approximations, such as meta-GGA functionals that incorporate higher-order derivatives of the electron density, and hybrid functionals that combine LDA or GGA with a fraction of Hartree-Fock exchange. These advanced functionals can provide improved accuracy for specific types of systems or properties, but they also come with increased computational costs. It's important to note that the choice of XC functional can have a significant impact on the results of DFT calculations, and the accuracy of the results depends on the appropriateness of the chosen XC functional for the specific system under study. Therefore, it is crucial to carefully select an appropriate XC functional for a given problem, and to validate the results against experimental or higher-level theoretical data whenever possible. If the main goal of the simulation is structural properties, one can, for example, compare the lattice parameters of a crystalline structure optimized with the XC functional with lattice parameters determined using experimental techniques, such as X-ray diffraction or neutron powder diffraction. On the other hand, if the focus of the simulation is on energy levels and band gaps, one could compare such calculated properties with ionization potentials determined experimentally.

Among the hybrid XC functional is PBE0. Being a hybrid functional, it combines some fraction of the exact exchange calculated using Hartree-Fock with the semi-local exchange-correlation functional PBE. The PBE0 functional was proposed by Perdew, Burke, and Ernzerhof, and is a modification of the PBE functional, which belongs to the GGA class [43–45]. PBE0 uses a fraction of the exact exchange to improve the description of the exchange interaction, while still using the semi-local PBE functional for the correlation interaction. The fraction of exact exchange is controlled by a mixing parameter, α, which ranges from 0 to 1. When $\alpha = 0$, PBE0 reduces

to the standard PBE functional, while when $\alpha = 1$, PBE0 becomes the pure exchange functional. The most common value for α is 0.25, which is the value used in this work.

Density functional theory exchange-correlation functionals encompass both the exchange and correlation effects within the electron density. However, the treatment of the Coulomb correlation, which is the classical electrostatic interaction between electrons, is not explicitly included in standard DFT functionals.

4.6 Grimme's D3 dispersion correction

While the Hartree-Fock approach completely neglects the Coulomb correlation, DFT presents an improvement. The exchange-correlation functional combines the exchange and correlation contributions into a single term that accounts for the effects of electron-electron interactions. The exchange part of the functional captures the quantum mechanical exchange interaction, which arises due to the antisymmetry of the electron wavefunction. And the correlation part accounts for the electron-electron correlation effects, which are associated with the repulsion between electrons.

While DFT functionals incorporate correlation effects to some extent, they typically do not explicitly include the long-range Coulomb correlation. This limitation arises from the approximation used in standard DFT functionals, which is typically based on the local density approximation (LDA) or the generalized gradient approximation (GGA). These approximations focus primarily on the local electron density and do not fully capture the long-range behavior of the Coulomb interaction.

The Grimme's D3 method [46] is a widely used dispersion correction scheme employed in density functional theory (DFT) calculations to account for long-range van der Waals (vdW) interactions. This method extends the previous D2 [47] method by incorporating three-body terms, which account for the non-additivity of the vdW interactions among three atoms. The D3 method adds a correction term to the total energy of the system, which is expressed as:

$$E_{total} = E_{DFT} + E_{disp} \tag{4.7}$$

Here, E_{DFT} represents the DFT energy calculated using a standard DFT functional, and E_{disp} is the dispersion energy correction. The dispersion energy is calculated by

$$E_{disp} = -\frac{1}{2}\sum_i \sum_j \left[s_6 \frac{C_6^{ij}}{r_{ij}^6} f_6^d(r_{ij}) + s_8 \frac{C_8^{ij}}{r_{ij}^8} f_8^d(r_{ij}) \right] - \frac{1}{6}\sum_i \sum_j \sum_k \frac{C_9^{ijk}}{r_{ijk}^9} f_9^d(r_{ijk}, \theta_{ijk}) \tag{4.8}$$

where $f_n^d(r_{ij})$ is the damping function that depends on the interatomic separation r_{ij}, and $C_n^{ij(k)}$ are the dispersion coefficients for the atom pairs and trios. The damping functions assure a smooth transition between the semilocal correlation computed by the XC functional and the long- and midrange correlation calculated by the D3 method. s_n are functional-dependent scaling factors (for PBE0, $s_6 = 1.0$ and $s_8 = 1.2177$. The dispersion coefficients are estimated from first principles by TD-DFT (Time-dependent density-functional theory) computation of the dynamical polarizability for model hydrides of all elements and using the Casimir-Polder integration. [47].

In a crystal lattice, the infinite sum is evaluated in direct space near the atom and in reciprocal space beyond a threshold radius, which makes the series convergent. This approach approximates the very computationally demanding estimation of many-body long-range electronic effects to a simple sum of terms, which can be almost instantaneously computed in almost any computer. However, we do have to pay a price for this great gain in computational times. These methods need some predetermined input parameters to calculate the van der Waals interaction. Besides that, the complex many-body interactions are treated outside the DFT framework and therefore the ground state wavefunction and ground state density do not contain non-local correlation effects. For fluorine, the dispersion constants are $C_6 = 7.2$, $C_8 = 122.8$, and $C_9 = 2574.3$

5 Basis sets

In the field of *ab initio* calculations, a fundamental aspect of making Hartree-Fock or Density Functional Theory calculations applicable is the choice of basis sets. They are used to represent the electronic wavefunctions in a form suitable for computers.

A basis set is a collection of functions used to approximate the wavefunctions of electrons in a system. These functions serve as building blocks for expanding the electronic density. In DFT, they are used in the expasion of the Kohn-Sham wavefunctions, while in Hartree-Fock they are used to expand the spin-orbitals.

5.1 Types of Basis Sets

There are two main types of basis sets commonly employed: plane wave basis sets, and localized or atom-centered basis sets. Each type has its own advantages and limitations, making them suitable for different types of systems and calculations.

Plane wave basis sets are commonly used for periodic systems, such as crystals, due to their ability to accurately represent extended electronic states. These basis sets utilize periodic boundary conditions and employ plane waves as the basis functions. The use of plane waves requires the inclusion of a sufficiently large number of wavevectors to accurately describe the electronic structure.

Localized basis sets are often employed for molecular systems, where the electronic states are more localized around the atomic

This explanation is guided by the lecture notes for the European Summer School "Ab initio modeling in solid-state chemistry", Torino, September 2000, by Mike Towler

nuclei. These basis sets consist of localized functions centered on each atom, such as Slater-type orbitals (STOs), Gaussian-type orbitals (GTOs) or numerical atomic orbitals (NAOs). Localized basis sets allow for a more efficient representation of the wavefunctions, particularly in systems with localized electronic density.

This work uses an atom-centered basis set. Even though we are dealing with a crystalline solid, the phases of fluorine studied here are composed of aggregated fluorine molecules. This could somewhat justify this choice, but the truth is that our preliminary studies using a hybrid exchange-correlation functional and Quantum Espresso, which uses a plane wave basis set, have shown to be extremely inefficient and have very slow convergence. This was one of our motivations to use CRYSTAL17, which demonstrated a more efficient algorithm for PBE0 at the time.

5.2 Gaussian basis sets

Slater-type orbitals have the exponential dependence $e^{-\zeta r}$ and are very close in their mathematical expression to the real atomic orbitals:

$$\varphi^{STO} = N r^{n-1} e^{-\zeta r} Y_{lm}(\Theta, \Phi) \tag{5.1}$$

Here, N is a normalization factor. The exponent ζ controls the spatial extent of the orbital. The coordinates r, Θ, and Φ correspond to the spherical coordinates. The angular part of the wavefunction is described by the function Y_{lm}, which determines the orbital's shape. In this equation, the classical quantum numbers principal, angular momentum, and magnetic are denoted by n, l, and m, respectively.

When it comes to approximating the wavefunction, although STOs provide better representation near the atomic nuclei, Gaussian-type functions (GTFs), are more commonly used. This preference arises from the fact that GTFs allow for faster computational implementations. Gaussian-type functions have the exponential dependence $e^{-\alpha r^2}$:

$$\varphi^{GTF} = N Y_{lm}(\Theta, \Phi) r^l e^{-\alpha r^2} \tag{5.2}$$

When performing calculations in quantum chemistry, particularly for many-electron systems, one often needs to evaluate many multidimensional integrals. These integrals can be computed more efficiently and more quickly if Gaussian functions are used, rather than Slater functions.

A key factor is that the product of two Gaussian functions is another (scaled and shifted) Gaussian function, which greatly simplifies the calculation of integrals. With Slater functions, the product is not a Slater function, which makes the integrals more complicated and computationally intensive. These GTFs will be further grouped to form a Gaussian-type Orbital (GTO) in what is called a contraction scheme. For further details on this, please refer to Appendix A.

To expand the wavefunctions (the ψ_i in DFT and χ_i in HF), we express them as linear combinations of predetermined functions

$$\psi_i = \sum_{\mu} c_{i,\mu} \varphi_{\mu} \tag{5.3}$$

Notice that once we have chosen our basis set $\{\varphi\}$, the variational problem both in DFT and HF in essence involves varying the coefficients c that minimizes the expectation value for the energy. In theory, this expansion is exact, but in practice, one must choose a finite number of functions for the basis, which introduces some error, called the finite basis set error.

Don't get confused with terms!

In many contexts in the field of computational quantum chemistry the terms "Gaussian-type functions" (GTFs) and "Gaussian-type orbitals" (GTOs) are used interchangeably. In this text, however, GTOs are used to refer to the functions built from a group of GTFs, which in other places might be called "contracted Gaussian-type orbitals" (cGTOs). Gaussian-type functions, in turn, might be called Gaussian primitives.

5.3 Gaussian basis sets in periodic systems

For periodic systems, the basis functions are actually Bloch wave functions (BFs), denoted as ϕ_μ, constructed from these GTOs. These BFs incorporate a phase factor that depends on the wave vector $\mathbf{k}$, which determines the frequency and direction of oscillation

$$\phi_\mu(\mathbf{r};\mathbf{k}) = \frac{1}{\sqrt{N}} \sum_{\mathbf{t}} \varphi_\mu^{\mathbf{t}}(\mathbf{r} - \mathbf{r}_a - \mathbf{t}) e^{i\mathbf{k}\cdot\mathbf{t}} \tag{5.4}$$

where $\varphi_\mu^{\mathbf{t}}$ represents the basis function φ_μ, which is localized at the position $\mathbf{r}_a$ in the original unit cell and translated into neighboring cells. The sum over $\mathbf{t}$ includes lattice translation vectors, allowing

the basis function to extend over the entire crystal lattice. In the periodic system context, equation (5.3) is rewritten as

$$\psi_{i\mathbf{k}} = \sum_{\mu} c_{i,\mu,\mathbf{k}} \phi_{\mu\mathbf{k}}(\mathbf{r}) \tag{5.5}$$

and $\psi_{i\mathbf{k}}$ may be called a crystalline orbital. It is important to note that the basis set of Bloch functions theoretically extends infinitely due to the continuous nature of the wave vector $\mathbf{k}$. However, in practical calculations, the problem is solved using a finite set of $\mathbf{k}$ points (defined by "shrinking" factors in most codes). This set of wave vectors is chosen in order to have the property that no two of them are equivalent, but every possible $\mathbf{k}$ vector has its equivalent in the chosen set. This set is called the first Brillouin zone. Therefore, by restricting the calculations to vectors in the first Brillouin zone, we are representing the entire infinite lattice without repetition.

A note should be made that, from the perspective of a user of a computational chemistry code, there's no difference between the input of basis functions for isolated molecules and crystalline systems, as the construction of the Bloch waves basis set is performed internally. Usually, the user will only have to provide a set of parameters (that might be taken from the literature in most cases) that define these basis functions.

5.4 Basis sets nomenclature

When discussing Gaussian basis sets, it is common in the literature to use certain terms that somewhat reflect the historical development of these bases. A traditional classification involves distinguishing between "core" basis functions and "valence" basis. Core functions typically consist of Gaussian-type orbitals with large exponents (more localized), while valence functions with smaller exponents (more diffuse). However, it is important to note that this classification is inherited from Slater orbitals and does not hold much significance in this context. We should always keep in mind that these basis functions do not represent atomic orbitals. In fact, the "core" functions may contribute significantly to the

highest occupied valence orbitals. Some classifications used are the following:

Minimal Basis Sets: The early Gaussian contractions were derived by least-square fitting to Slater orbitals. The number of Gaussian-type orbitals (GTOs) used to represent a single Slater orbital, known as "zeta," served as a measure of the set's quality. A minimal basis set, or single zeta basis set, contains a single basis function corresponding to each occupied atomic orbital. It represents the smallest set that can be reasonably used in any calculation.

Double-zeta (DZ) and Triple-zeta (TZ) Basis Sets: Double-zeta basis sets involve considering two basis functions for each atomic orbital, replacing each GTO of a minimal basis set. These basis functions differ in their orbital exponents. For instance, double-zeta sets employ two functions for H or He, ten functions for Li to Ne, and so on. Similarly, triple-zeta basis sets follow the same principle but employ three basis functions with varying orbital exponents.

Split-Valence (V) Basis Sets: Since valence electrons play a significant role in bonding, it is common to represent valence orbitals using a larger number of basis functions, than the number used for core orbitals. These basis sets are known as split-valence basis sets and typically use two GTOs for each valence atomic orbital and one GTO for each inner-shell atomic orbital. The inclusion of different orbitals with varying spatial extents allows the electron density to adjust appropriately to the molecular environment. The letter V denotes split-valence sets. For example, DZV represents a basis set with one contraction for core orbitals and two contractions for valence orbitals. It is worth noting that assigning more basis functions to valence orbitals does not necessarily mean incorporating more GTFs or primitives. Generally, core orbitals are represented by long contractions consisting of numerous GTFs to accurately capture the cusp of the s-type function at the nucleus.

Polarization (P) Basis Functions: While basis sets might be enough to describe orbitals of isolated atoms, when they are perturbed, their orbitals will typically need more "freedom" (more functions) to describe the distortion. Let us take the hydrogen atom as an example. When isolated, the basis function needed to describe its occupied orbital is just the 1s GTO.

However, in the presence of an electric field, the charge distribution becomes distorted and loses its spherical symmetry due to polarization. In this case a single 1s GTO is no longer suitable to describe this orbital, which needs the original 1s GTO plus a p-type function. The same happens in a chemical environment, so more basis functions might be added to describe this effect. For example, d-type functions which are not occupied in first-row atoms, play the role of polarization functions for the atoms from Li to F (that's why you will see a d-type GTO in the basis set used in this work). The 'zeta' terminology is often complemented with a description of the polarization functions. Thus, DZP means double-zeta plus polarization, TZP for triple-zeta plus polarization, and TZVP means a triple-zeta split valence polarized basis set.

Methods

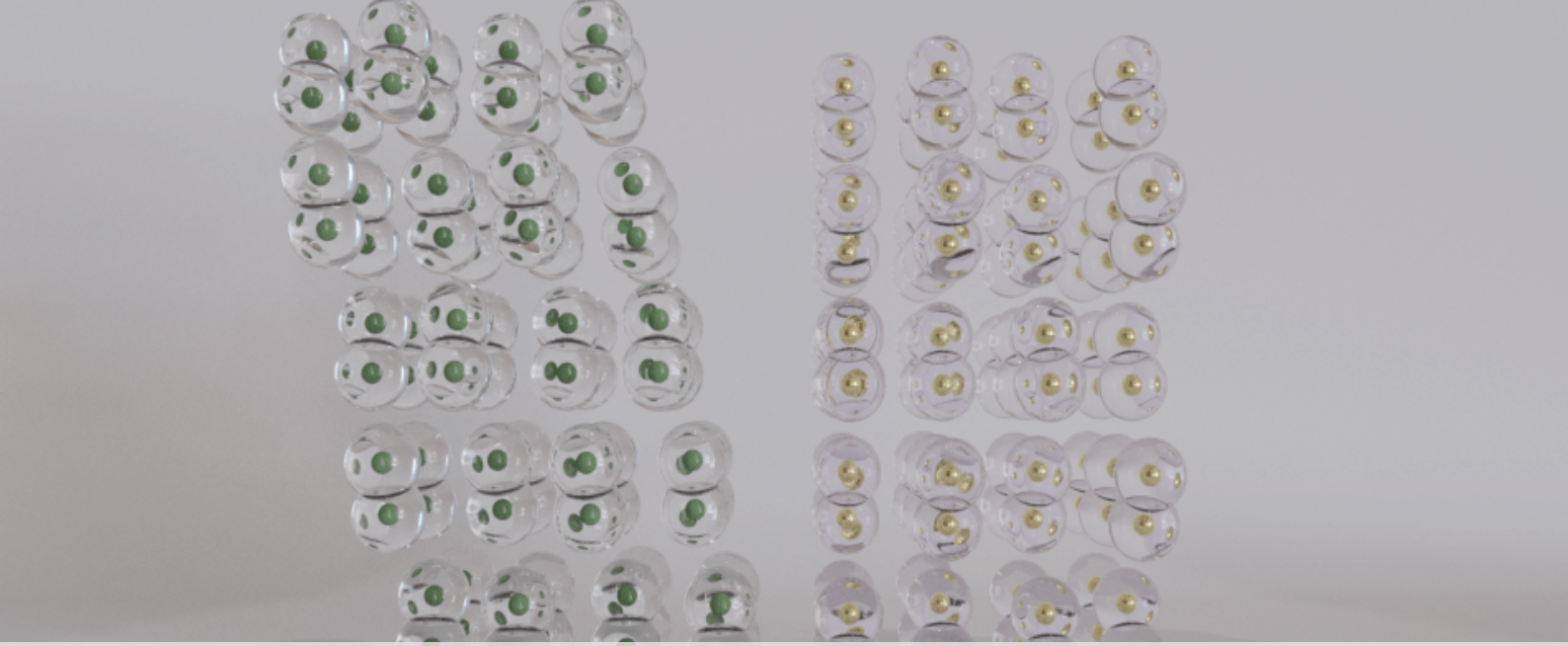

6 Overview

An overview of the general sequence of calculations and analysis performed in this work is presented in Figure 6.1.

A The investigation of static properties began with constant-pressure structure optimizations for both the $C2/c$ and $Cmce$ phases. The energy calculations were performed using Density Functional Theory (DFT) with the PBE0 hybrid exchange-correlation functional. The long-range dispersion effects, which are particularly significant in a molecular solid, were included using Grimme's D3 method.
The configurational energies of the optimized structures were used to evaluate the static stability of each phase at different pressures. The wavefunctions at zero pressure were used as input for Diffusive Monte Carlo calculations to obtain a more accurate assessment of static stability and dispersive energy.

B Subsequently, a quasi-harmonic vibrational analysis was performed using a supercell approach with 300 atoms. This analysis involved calculating the static energy for small atomic displacements in the supercell using DFT. The vibrational frequencies and phonon dispersion spectra were then obtained to evaluate the dynamic stability of each structure. The zero-point energy was calculated from the vibrational frequencies and added to the static energy to obtain the internal energy.

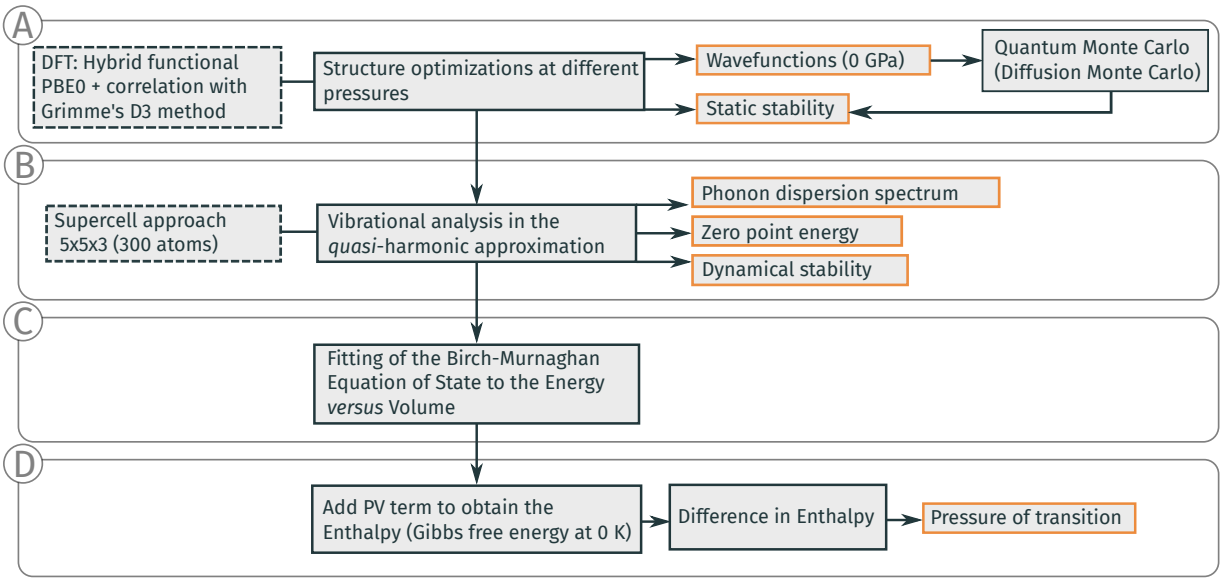

Figure 6.1: Diagram presenting the overall sequence of calculations and analysis performed in this work.

C The Birch-Murnaghan equation of state was fitted to the internal energy versus volume, which provided the pressure-volume-energy relationship for each phase. It should be noted that the pressure calculated from the equation of state is different from the pressure imposed during structure optimization. The pressure during optimization is estimated using configurational energy gradients, while the pressure calculated through the equation of state includes vibrational contributions in the form of zero-point energy.

D The equations of state were used to obtain a continuous function of internal energy U as a function of pressure. Adding the PV term resulted in the continuous enthalpy H (or Gibbs free energy at 0 K) as a function of pressure for each phase. Finally, we determined the enthalpy difference ΔH by subtracting the equations and estimated the pressure of transition by solving $\Delta H = 0$.

Further details on the conditions used in the calculations are given in the following sections.

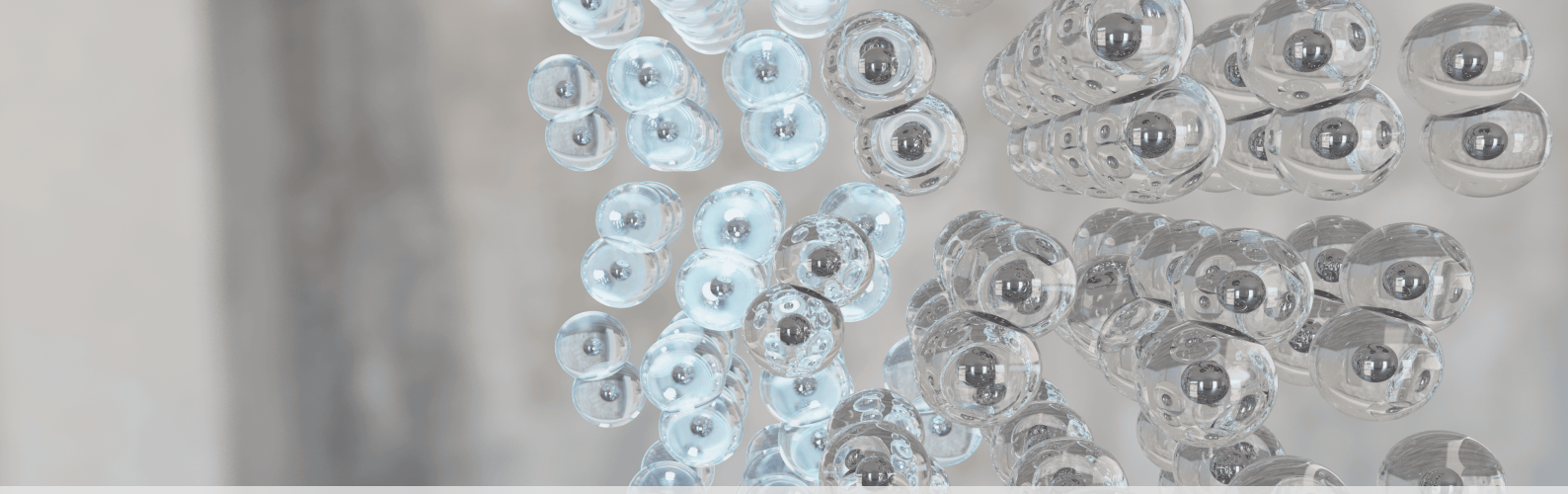

7 Computational details

All DFT calculations were performed using CRYSTAL17, using the def2-TZVP polarized triple-zeta-valence Gaussian basis set, and the hybrid PBE0 exchange-correlation functional [45, 48, 49] plus Grimme's D3+ABC dispersion correction, including three-body terms [31, 46, 47]. Grimme's D3 method adds a dispersive energy that is parameterized on atomic distances and angles, including two- and three-body terms. This approach has shown to be suited for van der Waals complexes as well as for intramolecular noncovalent interactions, and is extensively and successfully used in simulations of molecules, molecular complexes, and molecular solids [32].

This set of methods is hereby referred to as PBE0+D3(ABC)/TZVP. Overall, given the minute difference in energy between the two studied structures, we have used very tight convergence and tolerance parameters, and high-density sampling and integration grids. These criteria are further explained below.

7.1 Convergence tests

Convergence tests were performed to evaluate the effect of the main CRYSTAL settings for structure optimization on the α-F_2 $C2/c$ crystal structure, namely the tolerance on the gradient, the tolerance on the atomic displacements, and maximum trust radius. The optimization convergence is tested for the root-mean-square (RMS) and the absolute value of the largest component of both the gradients and the estimated atomic displacements. The tolerance for the largest component of the gradient and atomic displacements is 1.5 times the tolerance on their respective RMS. When

these four conditions are all satisfied at a time, the optimization is considered complete. The potential energy surface (PES) of molecular crystals often exhibits a flat landscape, so very tight tolerances on the gradient must be used. Otherwise, the algorithm may converge prematurely. Also, for this reason, we imposed a limit on the maximum trust radius allowed in search of the minimum in the potential energy surface. This parameter is essential for optimizing the structure of molecular crystals having a flat energy hypersurface. The trust region is the region of the objective function (the potential energy, in our case) that will be approximated by a simpler (usually quadratic) model. The step size of the optimization algorithm (changes in lattice parameters and atomic positions in our case) varies inversely proportional to the curvature (the Hessian, in higher dimensions) at the current position on the energy hypersurface. In flat regions with small curvature, the step size tends to be large, and the algorithm may miss a minimum due to an oversized step. The optimization convergence tests were performed using the experimentally determined structure for α-F_2 [30] relaxed using the default CRYSTAL17 optimization parameters as the starting point.

7.2 Static stability

We chose very strict optimization parameters, determined in the convergence tests, for the optimization of the crystal structure of fluorine $C2/c$ and $Cmce$ phases. Namely 10^{-5} a.u. for the tolerance on the RMS of the gradient, 10^{-4} a.u. for the tolerance of the RMS of atomic displacements, 10^{-11} E_h for the tolerance of primitive cell energy change between optimization cycles, and a maximum trust radius of 0.01. Notice that the default value for this parameter is 4.0.

We used the following conditions in the self-consistent field cycles for the calculation of the static energies. Threshold for convergence on the total energy of 10^{-12} E_h. An extra-extra-large pruned integration grid using the Becke method [50], which consists of 99 radial points and 1454 angular points in the regions relevant for chemical bonding. This is a very large and accurate grid that guarantees accurate integration of the exchange-correlation potential when derivatives of energy have to be computed [51].

We used the following parameters to control truncation and the accuracy of the calculation of the bielectronic Coulomb and Hartree-Fock exchange series. For the Coulomb series, we used 10^{-10} for both the penetration and overlap thresholds for Coulomb integrals. For the exchange series, we also used 10^{-10} as the overlap threshold for the HF exchange integrals, and 10^{-20} and 10^{-40} as the threshold of the other two series that compose the exchange-correlation term of the energy [51]. Finally, we used a sampling integration grid in reciprocal space of 11×11×5 that follows the Monkhorst-Pack scheme. Please see the Supplementary Material for details on how these criteria are translated into CRYSTAL17 input parameters.

These conditions were chosen to ensure an energy convergence within 1.5 μE_h/atom, which is actually smaller than the expected accuracy of DFT calculations (see below). Furthermore, these same conditions were also employed in obtaining the parameters of the Birch-Murnaghan equation of state for each fluorine crystal structure.

7.3 Quantum Monte Carlo

Diffusion Quantum Monte Carlo calculations were performed using the CASINO code [35, 52]. A trial QMC wave function was obtained by multiplying the determinant of single-particle orbitals from a DFT/PBE0 calculation by a Jastrow correlation factor [33, 35]. Density functional theory calculations were performed using CRYSTAL17 and the previously optimized $C2/c$ and $Cmce$ crystal structures. The single-particle determinant used to start the QMC calculations was obtained with the PBE0 exchange-correlation functional. Calculations were performed using the Trail and Needs Dirac-Fock pseudopotential [53]. The corresponding aug-cc-pVTZ-CDF correlation consistent Gaussian basis set had its outermost diffuse d function removed [54, 55].

The Jastrow factor allows including correlation effects on the ground state energy by considering contributions from isotropic electron-electron and electron-nucleus terms (u and χ terms), isotropic electron-electron-nucleus (f term), and plane-wave expansion term (p term). Calculations were performed using an expansion order of ten for the u and χ terms, three for the f term, and seven reciprocal lattice vectors in the p term expansion [35]. The trial wave function was optimized by minimizing the

variational Monte Carlo (VMC) total energy variance over 10^6 electron configurations. Finally, DMC calculations were performed for 2x2x2 (32 atoms, 85000 and 94000 diffusion Monte Carlo steps for the $C2/c$ and $Cmce$ structures, respectively) and 3x3x3 supercells (108 atoms, 52000 DMC steps for both structures), and from these results, the DMC total energies for the $C2/c$ and $Cmce$ structures were extrapolated to the infinite size limit. All calculations were performed using a time step of 0.003 atomic units.

7.4 Dynamical stability

The dynamical stability of the $C2/c$ and $Cmce$ fluorine structures were assessed by calculating the phonon dispersion spectra at different pressures along a chosen reciprocal space path [56]. The Brillouin zones of both lattices are presented in Figures 7.1 and 7.2. Calculations were performed using the supercell approach, with the primitive cell expanded by 5, 5, and 3 copies along the a, b, and c crystallographic axis, respectively.

Phonon frequencies were calculated by finite displacements of the atoms by 0.003 Å in this $5 \times 5 \times 3$ supercell. The integration sampling in this supercell is performed on a Monkhorst-Pack grid with shrinking factors chosen in order to maintain a density of points of 0.2 $2\pi/$Å[57].

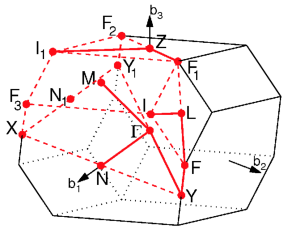

Figure 7.1: Brillouin zone for the C-centered monoclinic lattice, to which belongs the α phase of fluorine, $C2/c$ space group. Taken from [56]

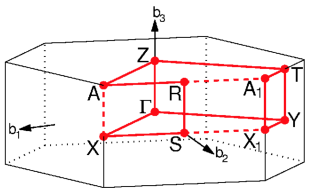

Figure 7.2: Brillouin zone for the C-centered orthorhombic lattice, to which belongs the hypothesized high-pressure phase of fluorine, $Cmce$ space group. Taken from [56]

Results and Discussion

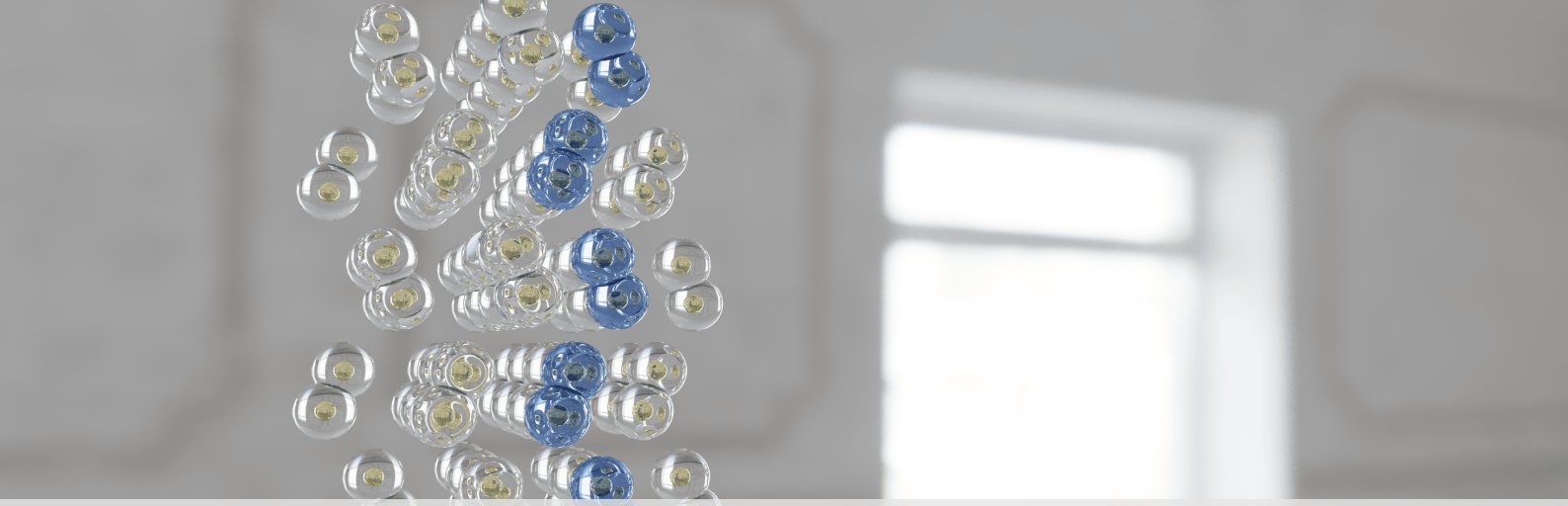

8 Results and Discussion

8.1 Crystal and electronic structure

The crystal structure optimizations performed at constant pressure have resulted in structures that align well with the experimentally observed α-F_2 phase at ambient pressure and the theoretically predicted $Cmce$ phase at higher pressures A comparison is presented Table 8.1.

Table 8.1: Lattice parameters and atomic positions of the $C2/c$ and $Cmce$ phases obtained from the structure optimization using DFT compared to experimental (α-F_2, $C2/c$) and theoretical structures from other works. The Wyckoff positions in both phases are in the $8f$ site.

		Theoretical			Experimental	
		This work	Ref. [24]	Ref. [29]	Refs. [17, 18]	Ref.[30]
$C2/c$	P (GPa)	0	0	0	Ambient	Ambient
	T (K)	-	-	-	23	10
	a (Å)	5.334	5.4009	5.494	5.50(1)	5.4780(12)
	b (Å)	3.166	3.2657	3.364	3.28(1)	3.2701(7)
	c (Å)	7.300	9.4781	7.113	7.284(1)	7.2651(17)
	β (°)	102.94	133.55	103.41	102.17(2)	102.088(18)
	x	0.2744	-1.10808	0.2662	0.285	0.2740(14)
	y	0.3181	0.07600	0.3263	0.317	0.315(2)
	z	0.0920	-0.09642	0.0961	0.0997	0.0942(12)
$Cmce$	P (GPa)	5	20	50		
	T (K)	-	-	-		
	a (Å)	4.586	4.3115	4.052		
	b (Å)	3.117	2.8812	3.683		
	c (Å)	6.331	5.8363	5.75		
	x	0.0000	-0.5000	0.0000		
	y	-0.4012	0.3799	0.1096		
	z	0.4028	1.39328	0.3975		

It is notable the discrepancy in the c parameter estimated using DFT with the PBE exchange-correlation functional, as reported by Lv et al. [24]. The elongated c parameter can be primarily attributed to an increased β angle. It appears that this difference is caused by a different choice of the repeating unit in the lattice by Lv et al. When adopting a unit closer to the one implemented in this work, the c and β parameters approach values of 7.69 Å and 112°, respectively. Refer to Figure C.1 for a schematic representation illustrating this point.

The characterization of the electronic structure of the material, at a more generalized level, can be accomplished by examining the band structure and the density of states, which are depicted in Figure 8.1. One significant feature common to both phases is a direct band gap at the Γ point. This suggests that an electronic transition could potentially occur without the need of momentum transfer from the crystal lattice.

Electronic band broadening

The broadening of electronic bands in response to increased pressure stems from three principal mechanisms. Firstly, an increase in pressure leads to a reduction in interatomic distances. This reduction results in a greater overlap of wavefunctions between neighboring atoms, offering electrons more possibilities to transition between states that were originally localized to particular atoms, which is translated into a broader range of energy. Secondly, pressure-induced deformations within the solid modify the energy landscape of the external potential. This alteration can introduce new permissible energy levels. Finally, from the viewpoint of quantum mechanics, constricting the space in which electron wavefunctions are confined increases their kinetic energy. This is a consequence of the Heisenberg Uncertainty Principle and contributes to the further broadening of energy bands.

The reduction in crystal dimensions with increasing pressure results in the expected broadening of the electronic band, as observed in the density of states. Additionally, the phase transition led to an increase in crystal symmetry, causing the overlap of bands that were separated in the $C2/c$ phase. This is particularly evident when comparing the Z-F_1 path in $C2/c$ with the Z-T path in $Cmce$, or the Z-I_1 ($C2/c$) with the Z-A path ($Cmce$). These paths are somewhat comparable (see Figures 7.1 and 7.2).

Generally, a material is characterized as a conductor if it shows non-zero occupation at the Fermi level and an absence of a band gap, a result of overlapping valence and conduction bands. Prior computational studies established that fluorine possesses a band gap of 2.58 eV at 6 GPa, and 2.28 eV at 100 GPa for the $C2/c$ and $Cmce$ phases, respectively [24]. It is noteworthy that these results were obtained using the PBE exchange-correlation functional, which is known to underestimate the band gap. For comparison, we also estimated the band gap using this same functional for the $C2/c$ phase at zero pressure and found a value of is 3.2 eV. A more accurate estimation of the band gap can be obtained using the hybrid PBE0, which results in 7.24 eV for the $C2/c$ phase at zero pressure, and 7.16 eV for the $Cmce$ phase at 5 GPa. Clearly, both phases are insulators.

Despite our results being fundamentally different from those reported by Tantardini et al. [29], they are in total alignment

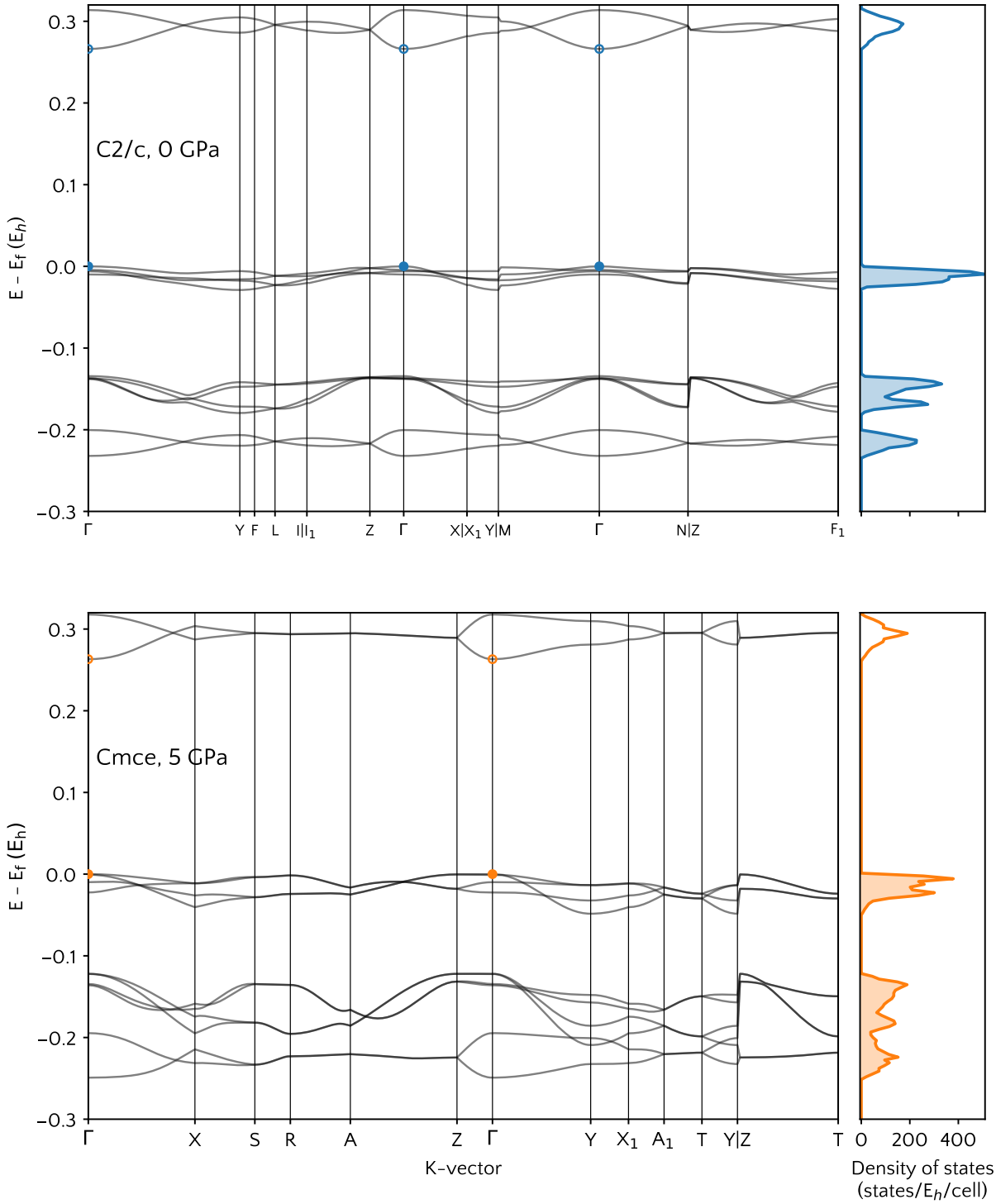

Figure 8.1: Electronic band structures and density of states for the $C2/c$ phase at 0 GPa and $Cmce$ phase at 5 GPa. In the band plots, filled circles indicate the maximum of the valence and open circles indicate the minimum of the conduction bands.

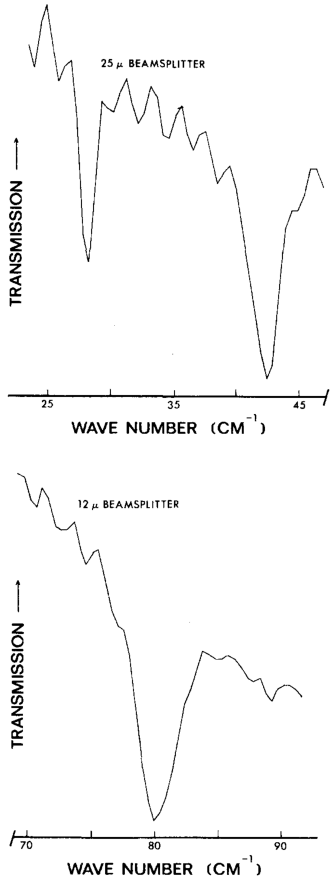

Figure 8.2: Far infrared spectra of α-F_2 measured at ambient pressure and 20 K. Taken from Niemczyk et al. [58].

with the scarce experimental data available for the alpha phase of fluorine and the theoretical findings previously mentioned. Meyer et al., in one of the pioneering studies on fluorine phases, observed that *"(...) fluorine become hard, brittle, and opaque when they transform from their high-temperature forms to lower-temperature forms, fluorine acquiring, not surprisingly, a slight yellowish tint"*[17]. No mention is made of anything resembling a metallic solid. Furthermore, metals typically display, at best, very broad infrared absorption bands due to their high free-electron density and substantial electrical conductivity. Contrarily, the alpha phase of fluorine shows well-defined infrared absorption bands, as depicted inFigure 8.2, providing yet another strong indication against the metallic nature.

The reduction in crystal dimensions with increasing pressure causes the expected spread in the electronic band, as is evident in the density of states. Furthermore, the increase in crystal symmetry in the phase transition caused the superposition of bands that were split in the $C2/c$ phase. Most notably comparing the Z-F_1 path in $C2/c$ with the Z-T path in $Cmce$; or the Z-I_1 ($C2/c$) with the Z-A path ($Cmce$). These paths are somewhat comparable (see Figures 7.1 and 7.2)

8.2 Static stability

Total energies from Density Functional Theory rarely have an accuracy better than 3 mE_h, and one cannot assuredly increase this accuracy systematically [59]. Nevertheless, a DFT calculation can be used as a good starting point for other techniques aiming to increase total energy accuracy by a rigorous account of the correlation energy. Accordingly, taking the structures optimized at the DFT/PBE0+D3(ABC)/TZVP level of theory, Diffusion Monte Carlo (DMC) calculations were performed to determine, with higher accuracy, the difference in static energy between the $C2/c$ and $Cmce$ phases.

Figure 8.3 presents the average local energy, the reference energy, and the best estimate of energy as the Diffusion Monte Carlo progresses. At the beginning of the simulation, the best estimate of the energy falls from the initial value (from the trial wavefunction) to around the correct ground-state energy in what is called the

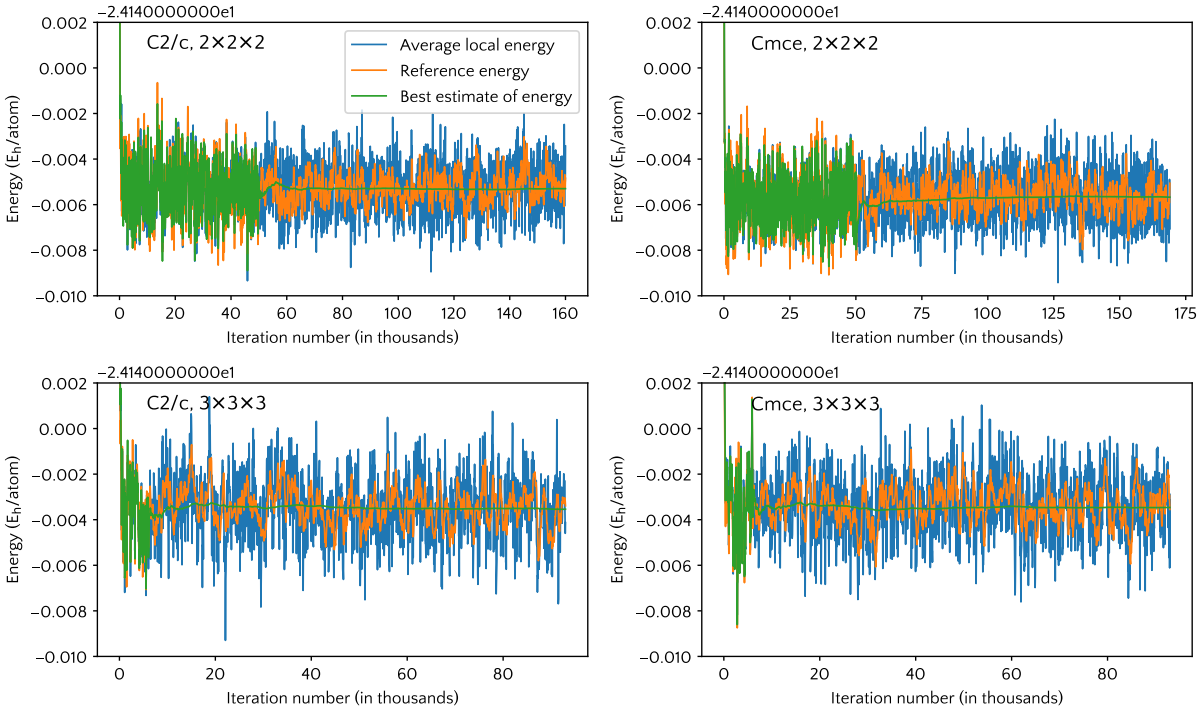

Figure 8.3: Evolution of energy as the Diffusion Monte Carlo simulation progresses for the four simulations performed. The estimated energy and respective error in each case is determined by the mean and standard deviation of the best estimate of energy during the statistics-acummulation phase.

equilibration phase. Following the equilibration is the statistics-accumulation phase. At this stage, the best estimate of energy will be very close to the correct value and we allow the simulation to propagate in order to accumulate enough energy data to estimate the DMC energy with a sufficiently low error bar. The energy and error are obtained from the best estimate of energy during the statistics-accumulation phase (green curve in Figure 8.3). From the energies and the inverse of the supercell size of the different simulations, it is possible to extrapolate the energies to the infinite cell size, shown in Figure 8.4

The DMC difference in static energy between fluorine $Cmce$ and $C2/c$ crystal structures, at zero pressure and temperature (without zero-point energy contribution), amounts to 270(130) μE_h per F atom, thus giving further evidence that the $C2/c$ phase is indeed the α-F_2 lowest energy structure.

For comparison, the difference in static energy at the DFT+D3(ABC)/TZVP level of theory is 40 μE_h/atom. The difference reported by Mattsson et al. (i.e., the difference between cohesive energies, not considering the vibrational ZPE) is 65 μE_h per F atom [23]. This last result was obtained by comparing the cohesive energies of a $C2/c$ structure,

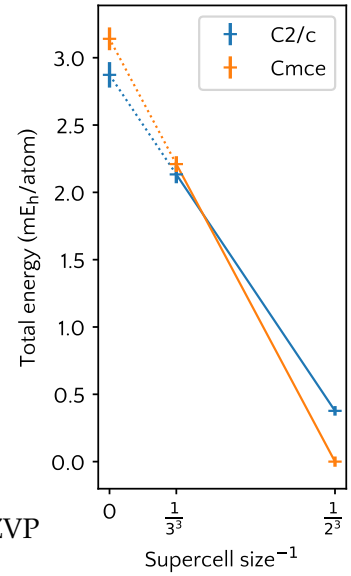

Figure 8.4: Extrapolation of the energies to the infinite cell size. Vertical bars at the data points are the error bars representing one standard deviation.

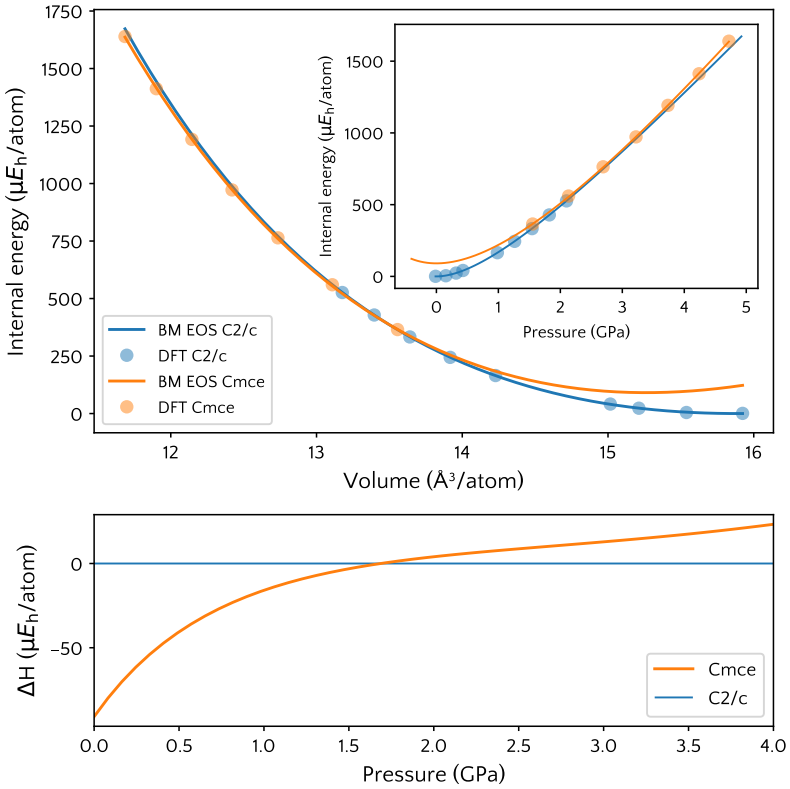

Figure 8.5: (Top) Internal energy *versus* volume as calculated at the DFT+D3(ABC)/TZVP level of theory, and the fitted Birch-Murnaghan equation of state (BM EOS) for C_2/c and $Cmce$ F_2. The inset shows the pressure-volume relationship according to the fitted EOS. (Bottom) Difference in enthalpy between the two fluorine phases. The $C2/c$ structure is used as a reference. In both panels, the pressure scale was determined by the respective equation of state of each phase.

as determined experimentally, and a $Cmce$ structure extrapolated from the other halogens and optimized by a p-LMP2 calculation (maintaining the intramolecular bond length fixed). Hence, part of the difference with the present DMC result might be ascribed to using different structures. Anyway, as we shall see, the fluorine $Cmce$ structure exhibits a dynamical instability at zero pressure, thus suggesting that the $Cmce$ crystal structure actually corresponds to a saddle point in the solid fluorine configurational space, which makes the comparison of static energies at 0 GPa of lesser importance.

Figure 8.5 exhibits the internal energy (static energy plus zero point energy in the *quasi*-harmonic approximation) for $C2/c$ and $Cmce$ α-F_2, optimized for a range of pressures up to 1.7 GPa for $C2/c$ and from 1.0 GPa up to 4.0 GPa for $Cmce$, as a function of volume and pressure. These ranges of pressure were limited by the particularities of the system, as we shall see in the following sections.

Fitting of the Birch-Murnaghan equation of state (EOS) [60, 61] to the internal energy *versus* volume data for the $C2/c$ phase yields an equilibrium volume $V_0 = 15.89(2)$ Å^3/atom, and a bulk modulus and its first derivative with pressure $B_0 = 6.38(5)$ GPa and

$B_0^{'} = 6.1(2)$, respectively. Fitting the EOS to the $Cmce$ phase results in an equilibrium volume $V_0 = 15.2(2)\,\text{Å}^3/\text{atom}$, a bulk modulus $B_0 = 10.3(1)\,\text{GPa}$, and first derivative of the bulk modulus with pressure $B_0^{'} = 4.0(1)$. The bottom panel of Figure 8.5 presents the difference in enthalpy between the two structures as a function of pressure, as calculated using the fitted EOS.

The static energies of both structures become equal at around 2.7 GPa, accompanied by the spontaneous transition during the optimization (see details below). When accounting for the zero-point energy to compose the internal energy, there is, in fact, no transition, as the internal energy of the $Cmce$ is higher than the internal energy of $C2/c$ for all the range of pressures evaluated. Finally, when adding the PV term to the internal energy to compose the enthalpy (or the Gibbs free energy at 0 K), the equilibrium between the two phases occurs at 1.6 GPa, as determined by the EOS.

We can improve this estimate by considering the Quantum Monte Carlo results, which were incorporated into the EOS by shifting the curves such that the energy difference at P = 0 GPa corresponds to the difference obtained from the Quantum Monte Carlo calculations. This is equivalent to fixing the E_0 parameters in the equations of state such that $E_{0,Cmce} - E_{0,C2/c}$ equals the QMC result. The resulting difference in enthalpy as a function of pressure is presented in Figure 8.6

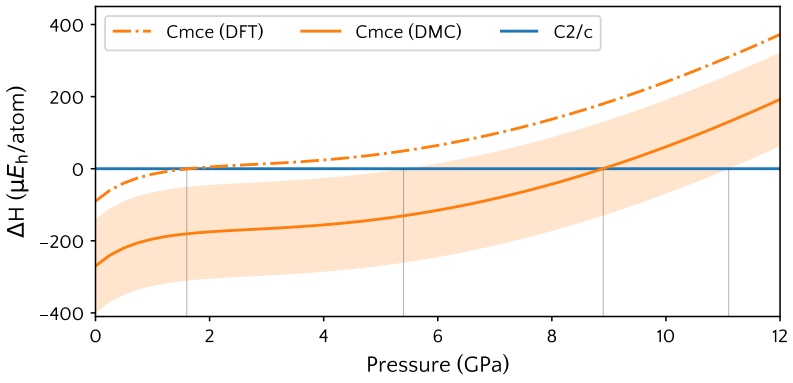

Figure 8.6: Difference in enthalpy between the two fluorine phases as determined by DFT and using the QMC result. The shaded area represents the uncertainty carried from the QMC result. The $C2/c$ structure is used as a reference. The pressure scale was determined by the respective equation of state of each phase.

By considering the Quantum Monte Carlo energy difference, the equilibrium between the two phases occurs at 8.9 GPa, which constitutes our best estimate for the $C2/c \rightleftharpoons Cmce$ transition pressure at zero temperature. A more comprehensive consideration of long-range correlation effects with diffusion Monte Carlo naturally results in a larger difference in energy between the two phases

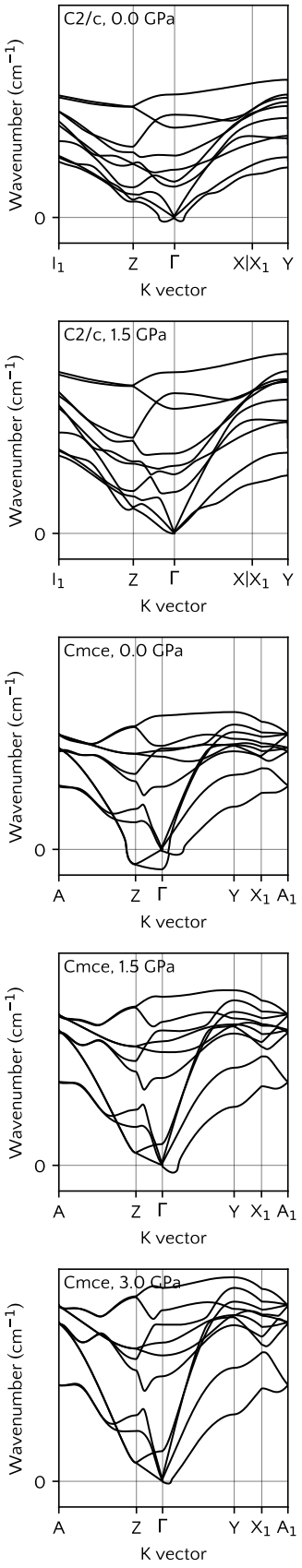

Figure 8.7: Evolution with pressure of the phonon dispersion spectra for the fluorine $C2/c$ and $Cmce$ structures.

when compared to density functional theory, since dispersion effects are generally attractive. This, in turn, results in a shift in the pressure of transition towards higher values. The uncertainty in the QMC result renders a range in pressure from 5.4 GPa to 11.1 GPa, represented by the shaded area in Figure 8.6. It's important to note that this adjustment implicitly assumes the correlation energy causes a constant shift in the energy difference across all pressures, which does not accurately reflect actual physical systems. To account for this, a Quantum Monte Carlo simulation would need to be run for each pressure evaluated, a task that was not accomplished for being too computationally demanding.

8.3 Dynamical stability

The dispersion spectra of fluorine $C2/c$ and $Cmce$ structures optimized at different pressures are presented in Fig Figure 8.7 (a more comprehensive dispersion plot is presented in Figures C.5 and C.6). While the phonon spectra for the $C2/c$ structure indicate this phase is stable at least up to 1.5 GPa, the $Cmce$ phonon spectrum at 0 GPa has a portion of an acoustic branch and an optical branch, along the Γ-Z direction, which exhibits imaginary (negative) frequencies, thus signaling a dynamical instability. This dynamical instability is possibly caused by the repulsive head-to-head interaction of the F_2 molecules in different molecular layers.

Indeed, the potential energy curve for displacements along the eigenvector of the Au-symmetry, Γ-point mode of imaginary frequency, depicted in Figure 8.10, shows that this head-to-head configuration corresponds to an energy maximum (a saddle point in the configurational energy landscape).

This vibrational mode corresponds to a shear sliding of the central layer of F_2 molecules. Furthermore, pressure stabilizes this head-to-head configuration, thus making the fluorine $Cmce$ structure dynamically stable with increasing pressure. More specifically, the frequency of the mode at Γ becomes positive above 0.5 GPa. At this pressure, however, the energy potential is highly anharmonic, and a proper description in the *quasi*-harmonic approximation is only possible above 1.0 GPa. This fact imposes a lower limit on the pressure range for which we evaluated the internal energy of the $Cmce$ phase. A comparison of the potential energy as a function

of the deformation along this mode and its respective harmonic potential at different pressures, and without an energy shift can be found, respectively, in Figure 8.8 and Figure 8.9.

In Figure 8.9 it is interesting to notice that with increasing pressure, the potential well exhibits a subtle tendency of becoming flatter. This tendency in made clearer in Figure C.7, in which the gradient of the energy with respect to displacement along the this eigenvector is plotted against displacement. We can observe that, for a given displacement, the gradient seem to reach a maximum around 0.5 GPa and then decrease. If interpreted as a component of the force along this shear direction, we see a decrease in the resistance to the shear movement between the molecular layer. This phenomenon was not further investigated.

One could argue that the unstable mode seen below 0.5 GPa is an indication of poor structure optimization. As a reminder, the structure optimization searches for a combination of lattice parameters and atomic positions of the space group in which the energy gradient vanishes, and that is precisely what was found. The structure found corresponds to the set of parameters and atomic positions that minimizes the potential energy under the constraints imposed by the $Cmce$ space group. The calculation of the vibrational frequencies involves the second derivative of the energy relative to atomic displacements that are not restricted to the same constraints of the space group used in the optimization. It is, therefore, reasonable to theoretically observe an optimized structure with dynamical instabilities. This, however, does not represent a thermodynamically stable structure and will not be empirically observed.

In heavier halogens, the intermolecular head-to-head configuration is stabilized by the electrostatic attraction between the positive σ-hole of one molecule and the negative charge density of the neighboring molecule, lowering the energy of the central configuration of Fig. 8.10 which thus becomes a minimum [23]. In $Cmce$ fluorine, at 0 GPa, this head-to-head interaction is mostly repulsive because of the absence of σ-holes in the F_2 molecules. However, this repulsive interaction is reduced by a slight shear displacement of the molecular planes. This can be observed both in the atomic displacements along the eigenvector of the unstable Au-symmetry mode (as seen in the off-center structures in Fig. 8.10) and in the $C2/c$ structure (see the bottom row of Fig. 1.6). Therefore, the

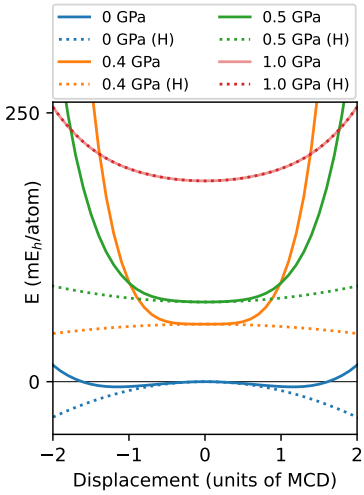

Figure 8.8: Potential energy *versus* displacement along the eigenvector of the Γ-point mode of imaginary frequency for the orthorhombic $Cmce$ fluorine structure at different pressures. H stands for harmonic. MCD stands for Maximum Classical Displacement [51].

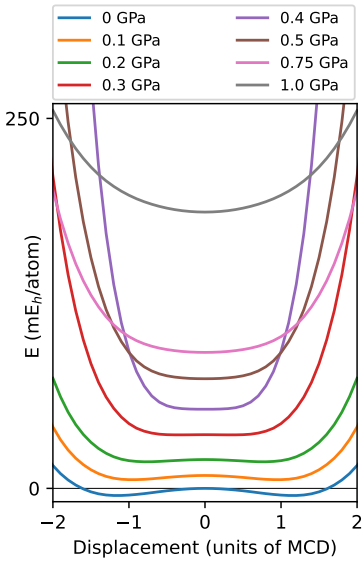

Figure 8.9: Potential energy *versus* displacement along the eigenvector of the Γ-point unstable mode for the orthorhombic $Cmce$ fluorine structure at different pressures.

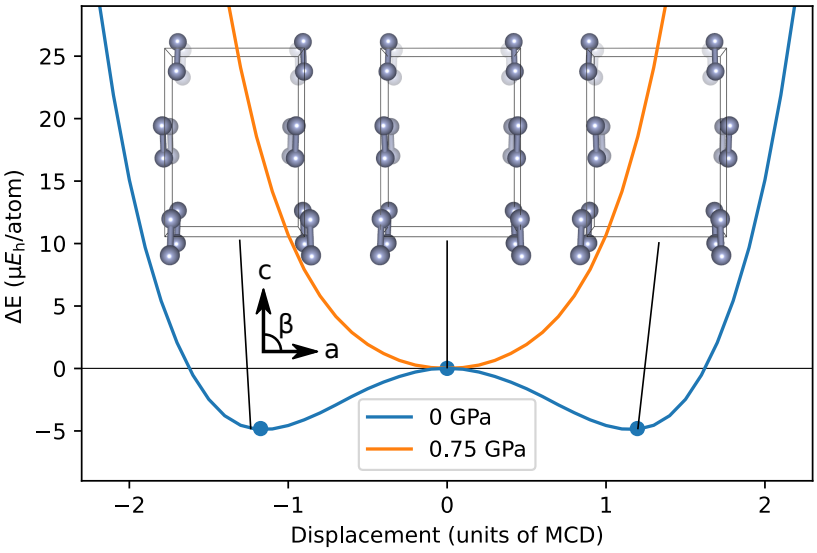

Figure 8.10: Potential energy *versus* displacement along the eigenvector of the Γ-point mode of imaginary frequency for the $Cmce$ fluorine structure at zero and 0.75 GPa. The atomic displacements depicted in the diagrams were exaggerated in order to make them clearer. MCD stands for Maximum Classical Displacement [51]. Both curves were shifted in order to match the central point to the reference energy.

evidence suggests that the dynamical instability of the fluorine $Cmce$ phase at 0 GPa is ultimately a manifestation of the lack of σ-holes on the fluorine molecule.

The Z point, coordinates (0,0,½), in the first Brillouin zone also exhibits dynamical instabilities. This wave vector is perpendicular to both a and b lattice axis and the wave-like distortions of the crystal are perpendicular to the c axis. In other words, all unstable modes in the Γ-Z path correspond to shear deformations of the molecular layers that render the head-to-head interaction between F_2 molecules. The depiction of the crystalline structure with eigenvectors for these modes is presented in Figure 8.11.

We built electrostatic potential maps of F_2 molecules in the crystalline structure of $C2/c$ at 0 GPa and $Cmce$ at 5 GPa, shown in Figure 8.12, in order to verify if the increase in pressure could have caused the development of sigma holes and, thus, explain the stabilization of the $Cmce$ structure at high pressures. The electrostatic potential (ESP) was plotted on an electronic charge density isosurface of 0.04 $a_0{}^{-3}$. We did not observe any significant change in electrostatic potential on the poles of the diatomic molecules where σ-holes are observed in chlorine, bromine, and iodine. Indeed, at moderate pressures, we don't expect any major changes in the electronic density of fluorine, the most electronegative element of the periodic table. We are currently unaware of what could cause this stabilization.

For reference, Figure 8.13 shows the electrostatic potential around the halogens' diatomic molecules calculated using the Parametrization Method 6 (PM6) in MOPAC2016, and using DFT in with the

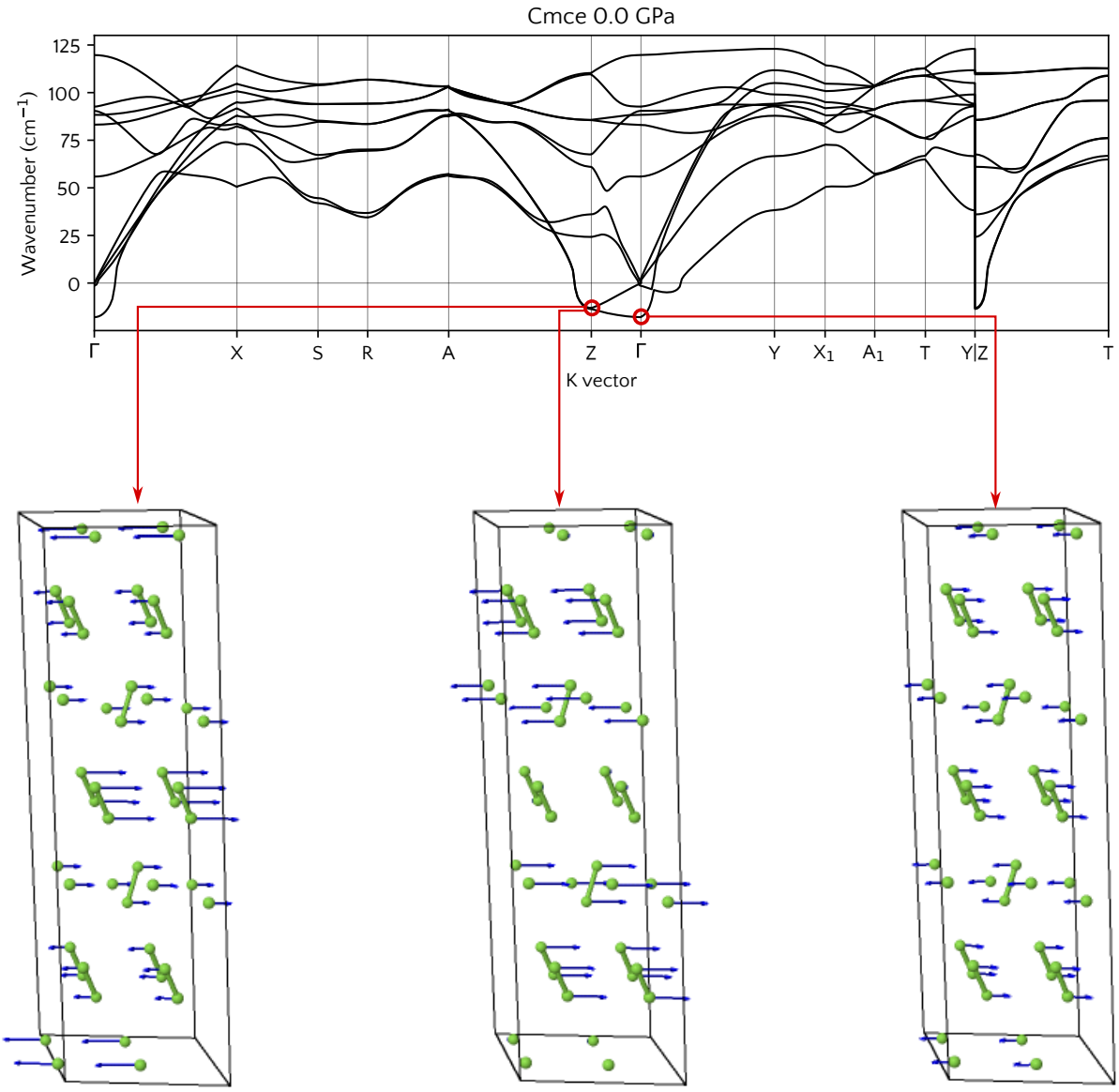

Figure 8.11: Phonon dispersion spectra for the fluorine *Cmce* structure at 0 GPa with representations of their eigenvectors on an expanded $1 \times 1 \times 2$ primitive cell. All eigenvectors have null c (z) components, meaning that they represent oscilations of pure shear deformation between the layers of molecules. It should also be noted that the fluorine atoms in their respective molecule move as a single entity.

B3-LYP exchange-correlation functional and the def2-QZVP basis set [62]. The potentials are mapped on a surface constructed as a union of atom-centered spheres. The radii of these spheres are equal to the respective van der Waals radius + 1 Å. If such a surface is constructed in the crystalline structure of fluorine, the volumes will intersect high-density regions of neighboring atoms.

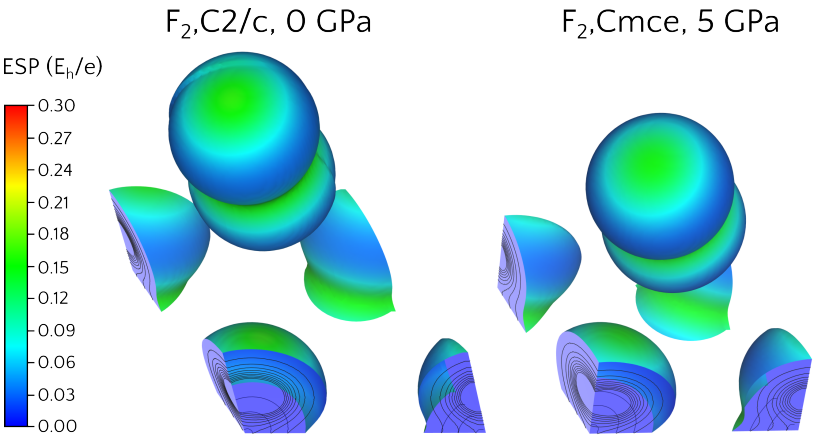

Figure 8.12: Electrostatic potential (ESP) mapped on a $0.04\,a_0^{-3}$ electronic density isosurface of the fluorine diatomic molecules in the α phase ($C2/c$, 0 GPa, left) and the hypothesized high-pressure phase ($Cmce$, 5 GPa, right).

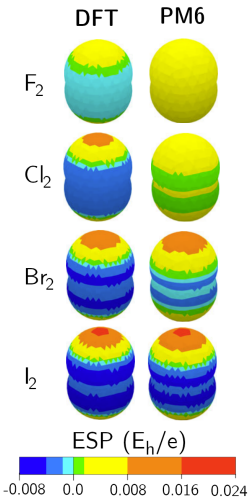

Figure 8.13: Electrostatic potential (ESP) calculated with DFT and PM6 for the halogens. Adapted from [62]

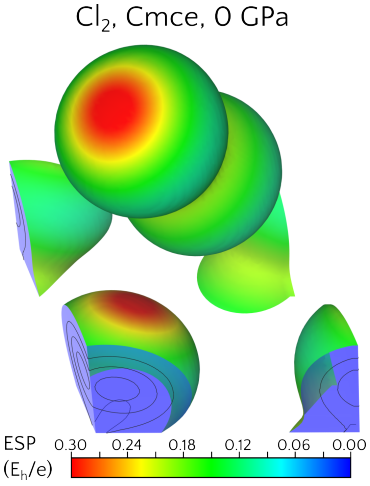

Figure 8.14: Electrostatic potential (ESP) mapped on a $0.04\,a_0^{-3}$ electronic density isosurface of chlorine, $Cmce$

In order to provide a more appropriate and direct comparison with the next heavier halogen, we calculated the electronic density and electrostatic potential for chlorine, $Cmce$ space group, optimized under the same conditions used for fluorine. We used the same exchange-correlation functional, the same D3(ABC) correlation correction, and the same type of basis set. Figure 8.14 presents the calculated potential also on a $0.04\,a_0^{-3}$ isosurface. Notice that the electrostatic potential color scales in Figure 8.12 and Figure 8.14 are the same. While both chlorine and fluorine exhibit more positive regions on the poles of the diatomic molecules, chlorine possesses a more positive region. Notice that this positive region in fluorine has the same electrostatic potential as the equatorial region of the bond. In chlorine, the polar region presents a more positive ESP.

Finally, we have observed small negative portions of several branches in all dispersion plots. Namely, the Z-Γ-X path for $C2/c$ at zero pressure, the Z-Γ path for $C2/c$ at 1.5 GPa, and the Γ-Y path at pressures 0.0 GPa, 1.5 GPa and 3.0 GPa. These are numerical artifacts from the supercell approach used.

8.4 Pressure-induced phase transition

The space group $C2/c$ is a subgroup of $Cmce$ and the $C2/c \rightleftharpoons Cmce$ transition fulfills the conditions for a second-order phase transition [63–65]. Accordingly, the $C2/c$ fluorine crystal structure may evolve continuously towards the $Cmce$ structure as pressure increases. In fact, in the constant-pressure optimizations, the $C2/c$ phase gradually collapses into the $Cmce$ space group for pressures higher than 1.7 GPa (see Fig. 8.15), essentially precluding the direct comparison of the energies over all the pressures range in the

analysis of this pressure-induced phase transition. Notice that this spontaneous transition to $Cmce$ imposes an upper limit on the pressure range for which we can explore the $C2/c$ phase.

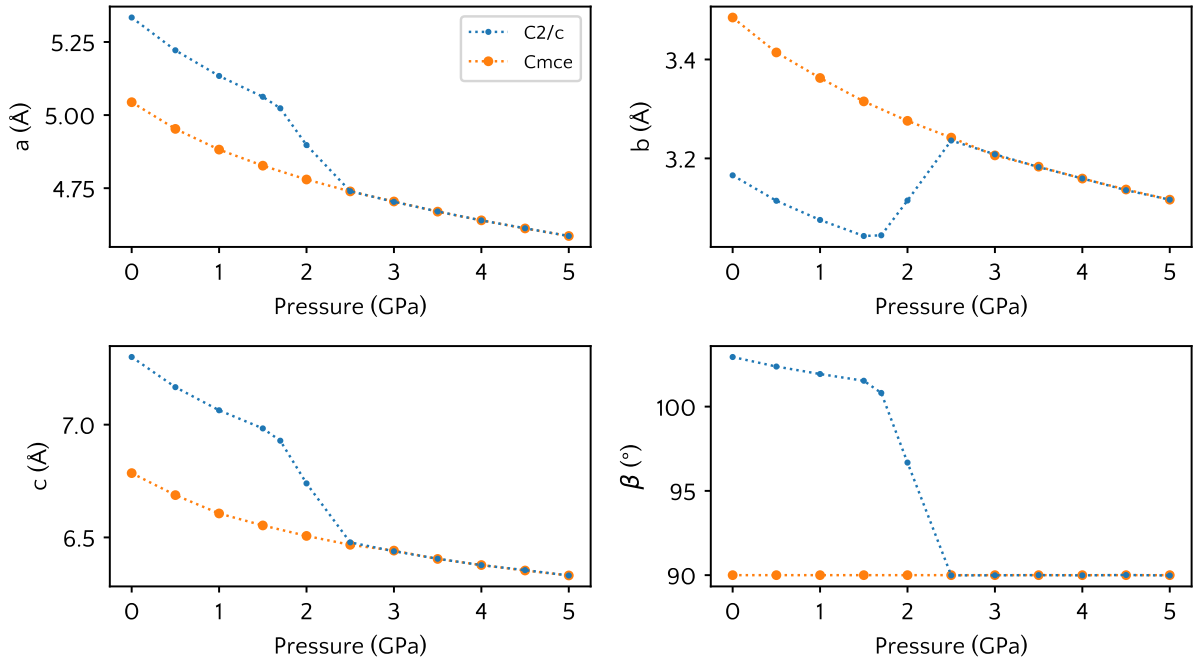

Figure 8.15: Fluorine lattice parameters as a function of the pressure imposed in the structure optimizations. The dotted lines are a guide to the eyes.

The order parameter for the $C2/c \rightleftharpoons Cmce$ transition is the spontaneous strain ϵ_{13}, which is the symmetry-breaking strain given by [66, 67]

$$\epsilon_{13} = \frac{1}{2}\left(\frac{c_{C2/c}}{c_{Cmce}}\cos\beta_{C2/c}\right) \tag{8.1}$$

where $c_{Cmce}(c_{C2/c})$ is the lattice parameter of the orthorhombic (monoclinic) phase along the c-axis, and $\beta_{C2/c}$ is the interaxial angle in the monoclinic structure. The spontaneous strain ϵ_{13} is represented as a function of pressure in Fig. 8.16, along with ϵ_{11}, ϵ_{22}, and ϵ_{33}, which are the non-symmetry-breaking spontaneous strains. The order parameter goes to zero at about 2.5 GPa. This analysis is made by considering solely the static enthalpy (with no zero-point energy) and the pressure imposed in the optimization. A more complete description of the order parameter for this transition would require structure optimizations minimizing the Gibbs free energy.

There is a close resemblance between the shear deformation behind the $C2/c \rightleftharpoons Cmce$ transition and the lateral displacement of

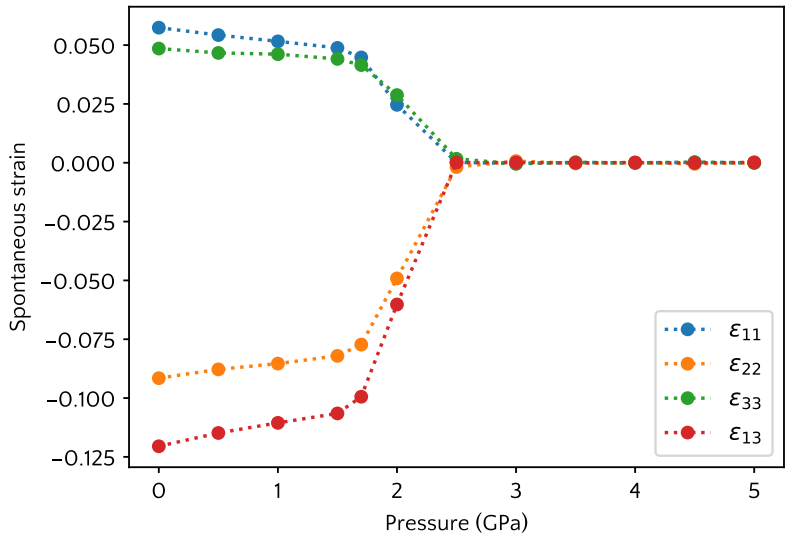

Figure 8.16: Fluorine spontaneous strains as a function of pressure. dotted lines are a guide to the eyes.

molecular F_2 layers characteristic of the eigenvector of the unstable Γ-point mode represented in Fig. 8.10, which suggests this latter may be considered a soft-mode associated to this pressure-induced phase transition. The other unstable modes in the Γ-Z are also associated with shear deformations of the molecular planes, though with wavelengths that exceed the lattice parameter c, and, therefore, we can apply the same rationale.

8.5 Raman spectra

The Raman spectra of the two fluorine phases were simulated to verify how easily the proposed phase transition would be detected by high-pressure Raman spectroscopy. Figure 8.17 shows the non-resonant, polycrystalline Raman spectra calculated for the fluorine $C2/c$ and $Cmce$ crystal structures optimized at 1.5 GPa, a pressure at which both phases are dynamically stable. These spectra were obtained considering the atomic motions as purely harmonic. These spectra are also compared to the experimental Raman spectrum of α-F_2 at 12 K and 1.5 GPa using a laser with wavelength in the visible light [19]. The Raman spectra of α-F_2 in the $C2/c$ and $Cmce$ structures exhibit two main peaks in the range of approximately 100 and 150 cm^{-1}. In the $C2/c$ phase, the calculated peaks primarily differ in their relative intensities and are slightly shifted towards higher Raman shifts compared to the experimental Raman spectrum. Despite these differences, the calculated spectrum shares the same number of peaks and a similar profile to the experimental result.

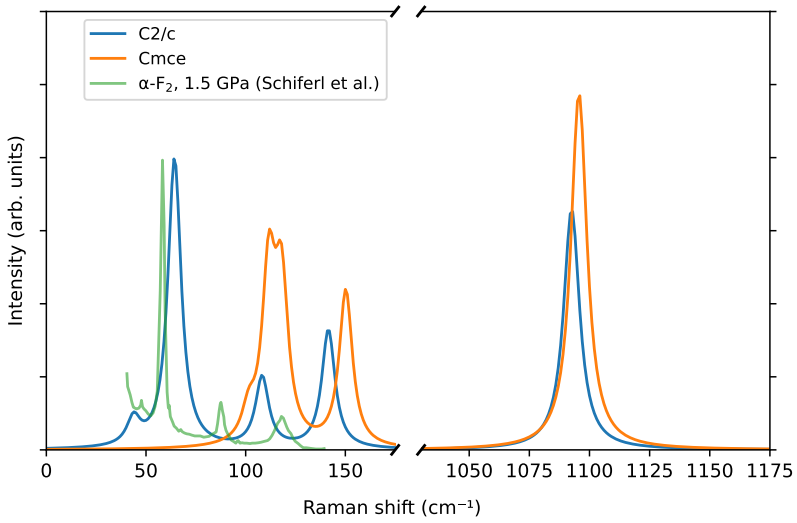

Figure 8.17: Calculated Raman spectra at 1.5 GPa for the $C2/c$ and $Cmce$ fluorine crystal structures and the experimental Raman spectrum of α-F_2 at 1.5 GPa and 12 K, as measured by Schiferl *et al.* [19].

The primary distinction between the Raman spectrum calculated for the $C2/c$ and $Cmce$ structures is the presence, in the former, of a strong Raman peak assigned to a librational mode at 64 cm^{-1} (slightly less for the experimental result). Indeed, the Raman spectra of the $Cmce$ and $C2/c$ fluorine structures are sufficiently different that a pressure-induced phase transition between these two structures would be promptly detected in the experimental study in which the Raman spectrum of fluorine was measured up to 6 GPa at temperatures as low as 10 K [19]. Therefore, the experimental observation that the fluorine Raman spectra at this thermodynamic conditions still exhibit the Raman peak assigned to the low-frequency librational mode of the C2/c suggests that 6 GPa as a lower limit for the pressure of $C2/c \rightarrow Cmce$ phase transition at that temperature. This discrepancy between the observed stability of the fluorine $C2/c$ structure near 10 K up to 6 GPa in the experimental Raman study and the $C2/c \rightarrow Cmce$ phase transition at about 1.6 GPa determined by the equations of state in this work may have its origin in the lack of the anharmonic contributions in our calculations, as well as a better method for accounting for the long-range correlation effects.

The F_2 stretching mode frequency is very similar in both structures (confirming the dispersion spectra), meaning that this mode does not significantly contribute to the Gibbs free energy difference between the competing structures. For this reason, the vibrational contribution to the Gibbs free energy difference is almost entirely determined by the fluorine libration modes, which, in turn, strongly depends on the correct account of dispersive interactions. Therefore, from the computational point of view, the equilibrium between

the fluorine $C2/c$ and $Cmce$ phases considering both the ZPE and vibrational entropy would require an accurate description of these dispersive effects. Long-range dispersion interactions are included in a parametrized, semi-empirical way at the PBE0+D3(ABC) level of theory. Although quantum Monte Carlo (QMC) calculations can precisely capture the dispersive contribution, their computational expense renders them unfeasible for calculating the extensive set of vibrational frequencies necessary to accurately estimate ZPE and vibrational entropy. Furthermore, in this particular case of fluorine, the dynamical instability of the $Cmce$ structure at low pressures suggests the need to go beyond the *quasi*harmonic approximation to allow incorporating the vibrational contribution to the Gibbs free energy.

9 Conclusions

Based on DFT calculations on the PBE0+D3(ABC)/TZVP level of theory and QMC calculations, further evidence is given that α-F_2 crystallizes into a $C2/c$ structure at 0 K and 0 GPa. Phonon dispersion analysis suggests that α-F_2 assumes the $C2/c$ structure not only because it is the lower energy structure but also because of a dynamical instability of the competing $Cmce$ structure. Furthermore, the observed dynamical instability of the $Cmce$ structure can be related to the absence of σ-holes in the F_2 molecules. The repulsive head-to-head intermolecular electrostatic interaction in fluorine destabilizes the $Cmce$ structure. The molecular arrangement in the $C2/c$ structure, on the other hand, reduces this head-to-head interaction and, accordingly, makes the $C2/c$ structure dynamically stable. In heavier halogens, the presence of σ-holes in the diatomic molecules' poles contributes to making the head-to-head intermolecular electrostatic interaction attractive and dynamically stabilizes the $Cmce$ crystalline structure.

We observed that α-F_2 spontaneously and continuously collapses into the $Cmce$ space group in the range from about 1.7 GPa to 2.5 GPa by performing constant pressure structure optimizations. The order parameter for the $C2/c \rightleftharpoons Cmce$ second-order transition also goes to zero near 2.5 GPa. It is worth noticing that by doing structure optimizations at constant pressure, we are minimizing the static enthalpy, i.e., the enthalpy at 0 K without ZPE contribution. When considering the enthalpy (static energy + zero-point energy + PV term), the equilibrium occurs at 1.6 GPa. The inclusion of the Quantum Monte Carlo energy difference places the equilibrium at

8.9 GPa, which is our best estimate for the pressure of transition between these two fluorine phases in the athermal limit. Other energy contributions, however small, should change the estimated transition pressure, as the energy differences between the phases are subtle. Therefore not much should be read into this pressure value. Nevertheless, the mechanisms involved in this transition, as well as its second-order nature, should hold even for a more in-depth treatment of the energy contributions.

The rigorous calculation of the equilibrium line between the $C2/c$ and $Cmce$ structures in the fluorine P-T phase diagram could be further pursued by using modern methods of free-energy difference calculation, including anharmonic effects. However, these calculations are made particularly complicated by the need to accurately include the contribution from long-range dispersion interactions, which are only approximately accounted for in DFT calculations, thus making this entire endeavor extremely challenging.

Appendix

A

Contraction schemes of Gaussian Basis*

Gaussian Basis functions are essential mathematical tools for approximating complex orbital behaviors of atoms in materials simulations. However, their application can be computationally taxing. The computational complexity of handling integrals over basis functions increases significantly with the number of functions in the basis set, which poses a drawback to the efficiency of the calculations. Therefore, the idea of basis set compactness comes into play, which aims at creating as accurate a representation of the orbitals as possible, using the fewest basis functions. Our ideal basis set comprises localized functions resembling atomic orbitals, but our chosen Gaussian functions do not correspond closely to exact Hartree-Fock (HF) atomic orbitals.

To achieve this, we often use a 'contraction' strategy. The Gaussian-type basis orbitals are formed from a linear combination of individually normalized primitive Gaussian functions $\varphi_j(\mathbf{r})$, each with identical center and angular quantum numbers, but different exponents. This mathematical expression can be represented as

$$\phi_i(\mathbf{r}) = \sum_j^L d_j \varphi_j(\mathbf{r}) \tag{A.1}$$

where

$$\varphi_j(\mathbf{r}) \equiv \varphi(\mathbf{r}; \alpha, l, m) = N_{lm}(\alpha) r^l Y_{lm}(\theta, \phi) \exp\left(-\alpha_j r^2\right) \tag{A.2}$$

where L is the length of the contraction, α_j are the contraction exponents, d_j are contraction coefficients. The primitive Gaussians

* This explanation is guided by the lecture notes for the European Summer School "Ab initio modeling in solid-state chemistry", Torino, September 2000, by Mike Towler

are denoted in terms of real spherical harmonics including a normalization constant. Through careful selection of these parameters, one can achieve desired properties in the resulting basis functions, such as reasonable cusp-like behavior at the nucleus, similar to Slater functions or Hartree-Fock (HF) atomic orbitals. By doing this, integrals involving such basis functions reduce to sums of integrals involving the Gaussian primitives. Even though many primitive integrals may need to be calculated for each basis function integral, these integrals are much cheaper to calculate and there's an overall gain in performance.

Moreover, since these contracted basis functions are better at describing the orbitals, this approach significantly reduces the number of orbital coefficients in the wavefunction (i.e. we get away with using fewer terms in Equation (5.3)). For instance, in a STO-3G basis, where three Gaussian primitives create a contracted function that resembles a Slater-type orbital, the size reduction from the primitive basis is a factor of 3. This corresponds to a nominal reduction factor of 81 (N^4) on the number of two-electron integrals, which constitutes a substantial reduction. By employing such strategies, the complexity of material simulations can be significantly managed, allowing us to perform accurate predictions without overwhelming computational resources.

The standard way to obtain the exponents and contraction coefficients is to perform Self-Consistent-Field calculations to determine basis functions suitable for describing exact Hartree-Fock atomic orbitals. Thus, an approximate atomic basis function is expanded using a set of primitive Gaussians, which are advantageous for computational reasons.

An interesting implication of this method is that although many primitive Gaussian functions may be necessary to represent an atomic orbital adequately, their relative weights remain largely unchanged when atoms form molecules. This allows us to determine these weights from prior calculations and the quantum chemistry code will only adjust the overall scale factor for the contracted Gaussian function in our extended calculations. In calculations such as the ones performed in this work, we get our basis functions for the atomic species from the literature and may use them (almost) directly in our molecular calculations, after a preliminary evaluation.

This contraction scheme can be applied to solid-state physics. In this context, we have a reference unit cell with a certain number of non-equivalent atoms. Each of these atoms gets assigned a set of Gaussian-Type Orbitals (GTOs), which are built from contractions of Gaussian primitives. Let's call the number of these GTOs p.

Next, we need to convert these GTOs into something that's useful for studying crystals. We do this by forming Gaussian-type Bloch functions (GTBFs), which are also Np in number. Each GTBF is constructed using a formula:

$$\phi_{i,\mathbf{k}}(\mathbf{r}) = \sum_{\mathbf{t}} \varphi_a^{\mathbf{t}}(\mathbf{r} - \mathbf{r}_a - \mathbf{t}) \exp(i\mathbf{k}\mathbf{t}) \tag{A.3}$$

where the $\mathbf{r}_a$ are the coordinates of the basis atom in the reference zero cell with which φ_a is associated. In fact, there are no practical differences in the form of the basis set input compared to the molecular case, as the transformation of the one-electron basis functions to their Bloch form is done internally after the definition of the localized atomic functions. However, the exponents and contraction coefficients in the two cases will generally be rather different, and with some exceptions such as molecular crystals and certain covalent systems, molecular basis sets are not directly transferable to the study of crystalline solids.

To help with computational efficiency, computer programs group atomic orbitals belonging to a given atom into shells. A shell contains all atomic orbitals with the same n and l quantum numbers - for example, all d functions in a $3d$ shell. This arrangement helps us to simplify the total charge density into shell charge distributions, which is handy when we're dealing with bi-electronic integrals and long-range interactions.

This can be further reduced using one neat trick taken from Pople-type basis sets. Some atomic orbitals may be grouped based on their principal quantum number into shells, for example, a $2sp$ shell. In such a shell, both $2s$ and $2p$ functions share the same set of exponents α_j but have different contraction coefficients d_j. This way, we cut down on the number of extra functions we need to calculate electron integrals. Interestingly, sp shell structures can save up to four times the CPU time compared to when s and p have different exponents. However, this isn't a one-size-fits-all solution.

In some cases, the *sp* shells can limit the form of basis functions. In computer codes such as CRYSTAL, one will define the parameters grouped into such shells.

See, for example, how these definitions are used in the basis set input used for fluorine:

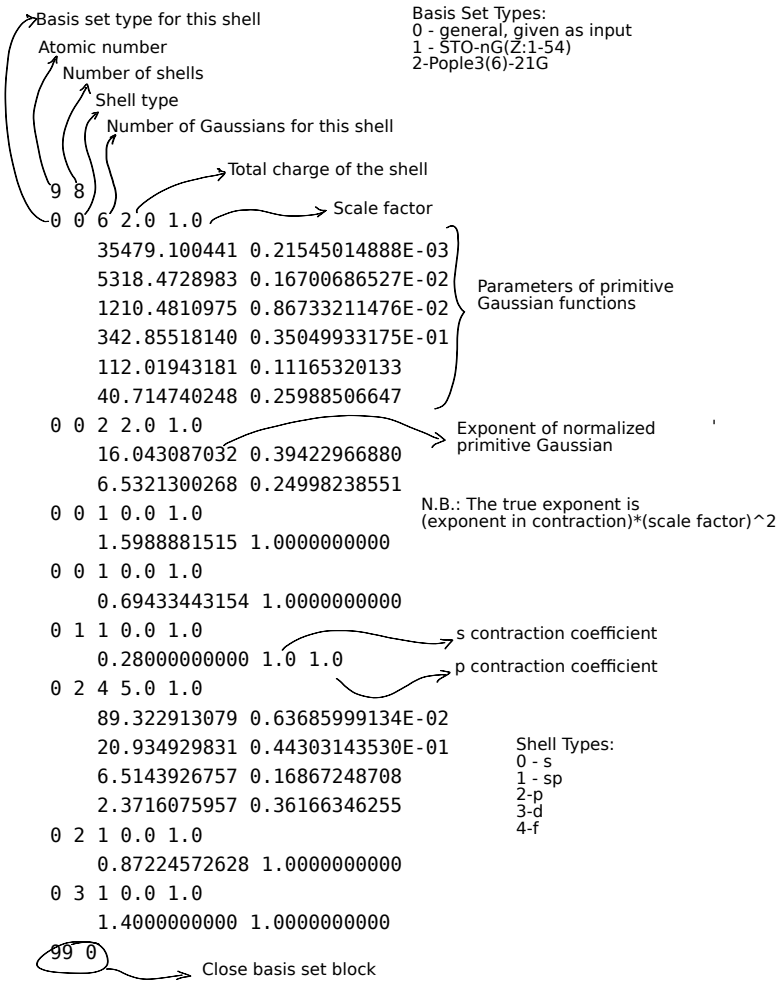

fluorine - TZVP basis from
https://pubs.acs.org/doi/suppl/10.1021/acs.jpcc.5b03433/suppl_file/jp5b03433_si_001.pdf

B

Computational details - CRYSTAL17

B.1 Gaussian Basis set

We used the following TZVP basis set in our DFT calculations [23], here presented in CRYSTAL17 format.

```
9 8
0 0 6 2.0 1.0
   35479.100441 0.21545014888E-03
   5318.4728983 0.16700686527E-02
   1210.4810975 0.86733211476E-02
   342.85518140 0.35049933175E-01
   112.01943181 0.11165320133
   40.714740248 0.25988506647
0 0 2 2.0 1.0
   16.043087032 0.39422966880
   6.5321300268 0.24998238551
0 0 1 0.0 1.0
   1.5988881515 1.0000000000
0 0 1 0.0 1.0
   0.69433443154 1.0000000000
0 1 1 0.0 1.0
   0.28000000000 1.0 1.0
0 2 4 5.0 1.0
   89.322913079 0.63685999134E-02
   20.934929831 0.44303143530E-01
   6.5143926757 0.16867248708
   2.3716075957 0.36166346255
0 2 1 0.0 1.0
   0.87224572628 1.0000000000
0 3 1 0.0 1.0
   1.4000000000 1.0000000000
99 0
```

The following Fluorine aug-cc-pVTZ-CDF [54, 55] basis set was used for the SCF calculation used as starting point for the QMC calculations

```
209 12
0 0 10 2.0 1.0
   74.89951 -0.002468
   46.74199  0.019169
   29.16436 -0.081152
   18.19700  0.213929
   11.37305 -0.254988
   3.96885  -0.064450
   2.04155   0.236186
   0.91037   0.462394
   0.41030   0.379259
   0.18153   0.090351
0 2 10 5.0 1.0
   67.31505 -0.001110
   42.08949  0.007863
   26.31654 -0.034263
   16.18931  0.078927
   5.97723   0.112359
   2.90851   0.189780
   1.43846   0.276085
   0.68046   0.314725
   0.30498   0.240771
   0.12804   0.074778
0 0 1 2.0 1.0
    2.3857   1.0
0 0 1 0.0 1.0
    0.3392   1.0
0 2 1 0.0 1.0
    0.843    1.0
0 2 1 0.0 1.0
    0.2591   1.0
0 3 1 0.0 1.0
    3.1164   1.0
0 3 1 0.0 1.0
    0.8721   1.0
0 4 1 0.0 1.0
    1.9082   1.0
0 0 1 0.0 1.0
    0.1598   1.0
0 3 1 0.0 1.0
    0.2812   1.0
0 4 1 0.0 1.0
    0.7007   1.0
```

B.2 Convergence tests

Convergence tests were performed to evaluate the effect of the main CRYSTAL settings for structure optimization on the α-F_2 $C2/c$ crystal structure, namely TOLDEG, TOLDEX, and MAXTRADIUS. TOLDEG defines the tolerance for the root-mean-square of the energy gradient in each self-consistent field cycle. The potential energy surface (PES) of molecular crystals often exhibits a flat landscape, so very tight tolerances on the gradient must be used. Otherwise, the algorithm may converge prematurely. The tolerance on the maximum gradient component is 1.5 times the value of TOLDEG. TOLDEX defines the root-mean-square threshold for atomic displacements for the optimization cycles. Just as with TOLDEG, the maximum tolerance for an atomic displacement is 1.5 times the value of TOLDEX. Lastly, the MAXTRADIUS keyword defines the maximum trust radius allowed in search of the minimum in the potential energy surface. This parameter, whose default value is 4.0 in CRYSTAL17, is essential for optimizing the structure of molecular crystals having a flat energy hypersurface. The trust region is the region of the objective function (the potential energy, in our case) that will be approximated by a simpler (usually quadratic) model. The step size of the optimization algorithm (changes in lattice parameters and atomic positions in our case) varies inversely proportional to the curvature (the Hessian, in higher dimensions) at the current position on the energy hypersurface. In flat regions with small curvature, the step size tends to be large, and the algorithm may miss a minimum due to an oversized step. MAXTRADIUS limits the size of the step in the minimization algorithm. However, reducing MAXTRADIUS comes with the risk of a slower convergence of the optimization algorithm. We tested the convergence of the energy and the structural parameters after optimization by varying TOLDEG (3×10^{-5}, 10^{-5}, and 5×10^{-6}), TOLDEX (1.2×10^{-3}, 5×10^{-5}, and 10^{-5}), and MAXTRADIUS (0.25, 0.1, and 0.05). Notice that even the least strict conditions tested are already much more stringent than the default values (3×10^{-4}, 1.2×10^{-3}, and 4.0 for TOLDEG, TOLDEX, and MAXTRADIUS, respectively). In fact, we chose to be rigorous in this aspect precisely because we are dealing with a molecular crystal with a possibly flat energy hypersurface around the global minimum. The optimization convergence tests were performed using the experimentally determined structure for α-F_2 relaxed using the default CRYSTAL17 optimization parameters as the starting point.

B.3 Structure optimization

We chose very strict convergence criteria for crystal structure optimization of fluorine $C2/c$ and $Cmce$ phases, namely TOLDEG 0.00001, TOLDEX 0.0001, TOLDEE 11, and MAXTRADIUS 0.01. For the calculation of the

static energies of the optimized structures, the chosen conditions were XXLGRID, TOLDEE 12, TOLINTEG 10 10 10 20 40, and SHRINK 11 11 5. These conditions were chosen to ensure an energy convergence within 1.5 μE_h/atom, which is actually smaller than the expected accuracy of DFT calculations. Furthermore, these same conditions were also employed in obtaining the parameters of the Vinet equation of state for the $C2/c$ and $Cmce$ fluorine crystal structures.

C

Additional figures and plots

C.1 Different choice of repeating unit for Lv et al.

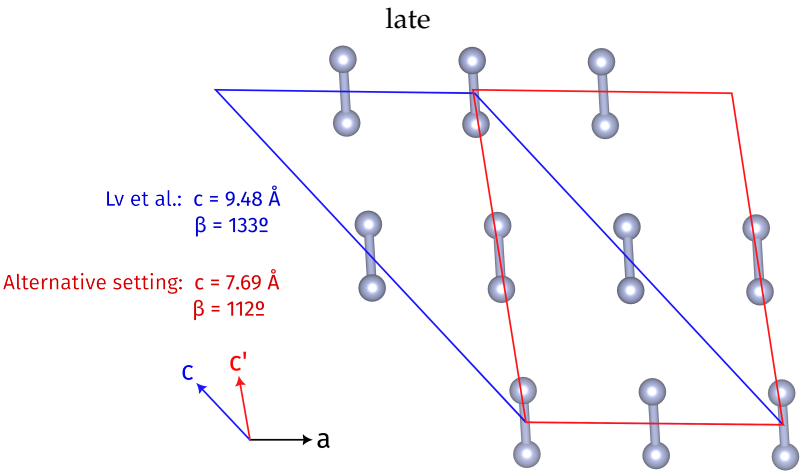

Figure C.1: Diagram showing a different choice of the repeating unit for the lattice of α-F_2. The original choice (blue) results in larger β and c parameters. The alternative choice (red) can be used to compare the results obtained in this work.

C.2 Lattice parameters and atomic positions

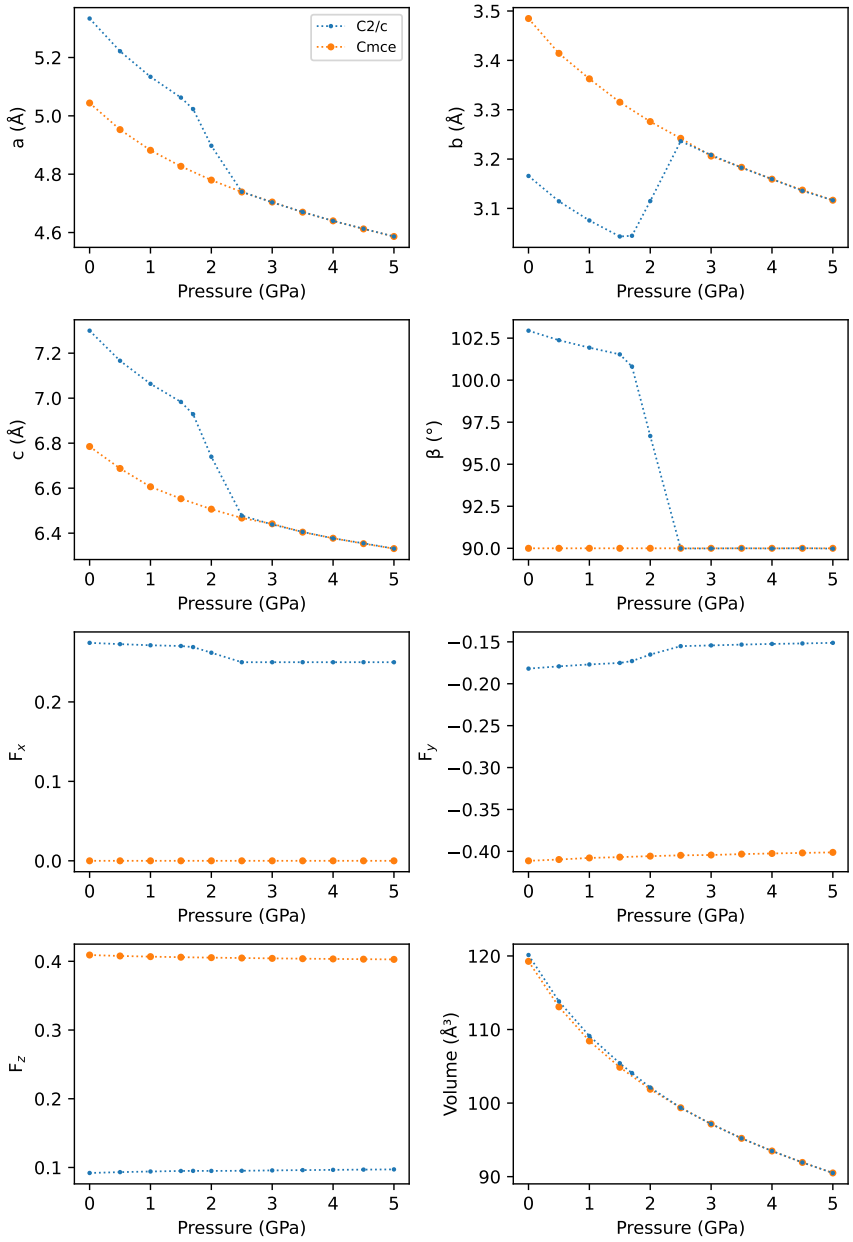

Figure C.2: Lattice parameters and atomic positions of the fluorine structures as a function of the pressure imposed in the optimization. The constant pressure optimization minimizes the static enthalpy (no zero-point energy)

C.3 Contributions to Total Energy

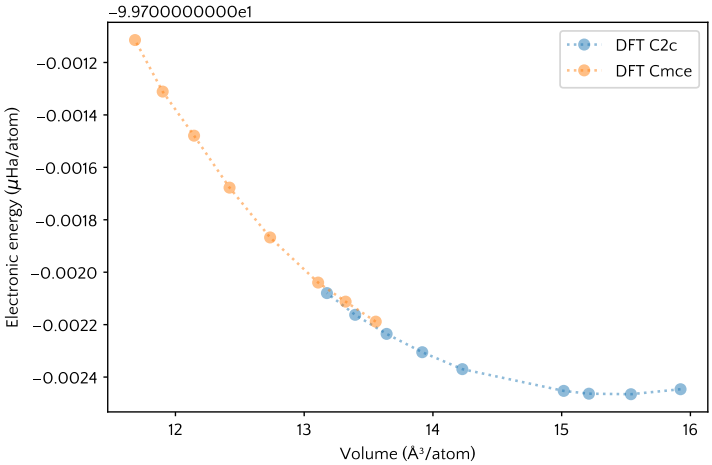

(a) Electronic (potential) energy.

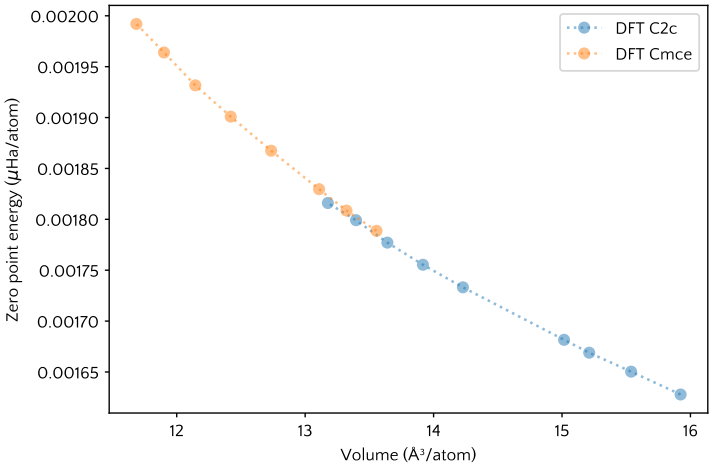

(b) Zero point energy.

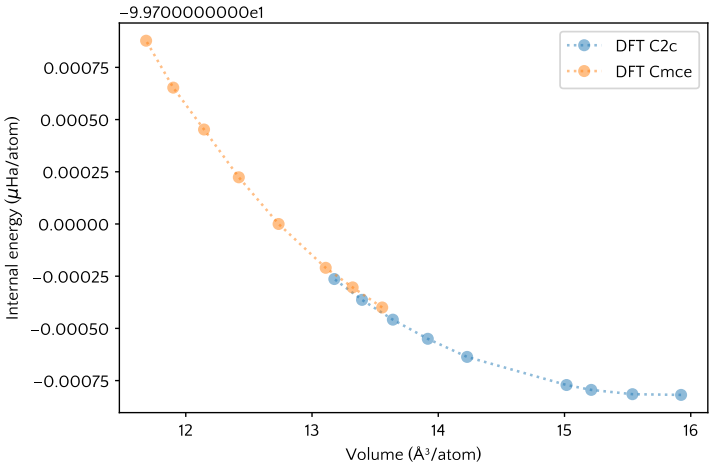

(c) Internal energy.

Figure C.3: Contribution to total energy as a function of volume. Circles are the DFT data calculated at the PBE0+D3(ABC)/TZVP level of theory. Dotted lines are a guide to the eyes.

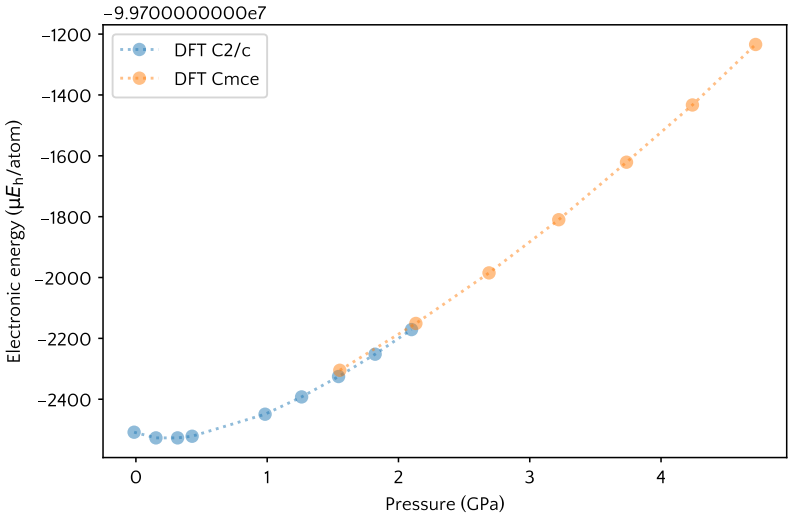

(a) Electronic (potential) energy.

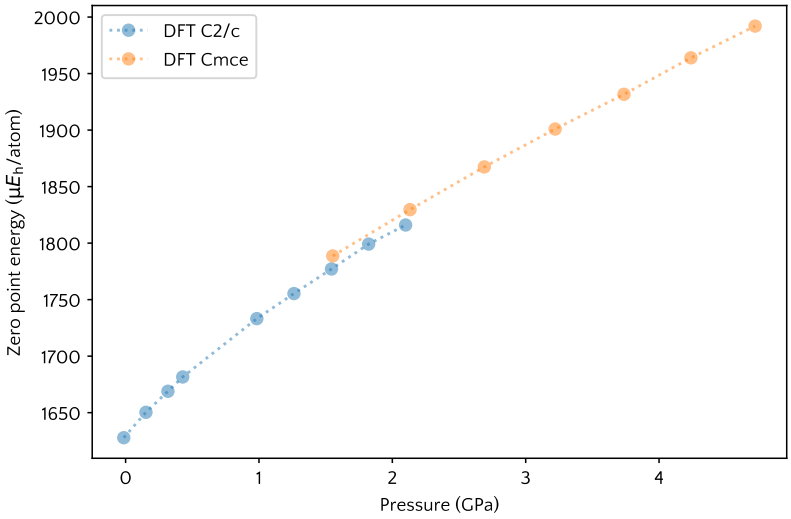

(b) Zero point energy.

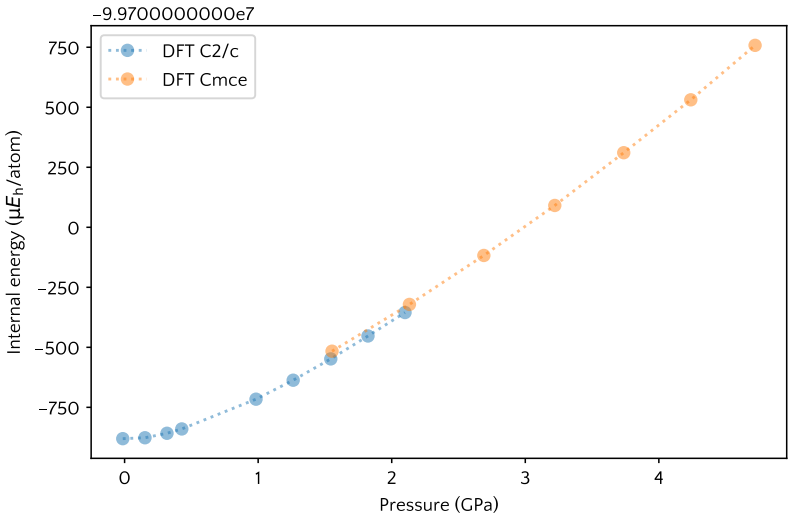

(c) Internal energy.

Figure C.4: Contributions to total energy as a function of pressure. Circles are the DFT data calculated at the PBE0+D3(ABC)/TZVP level of theory. Volume was converted to pressure for each phase using their respective fitted Birch-Murnahan equation of state. Dotted lines are a guide to the eyes.

C.4 Phonon dispersion spectra

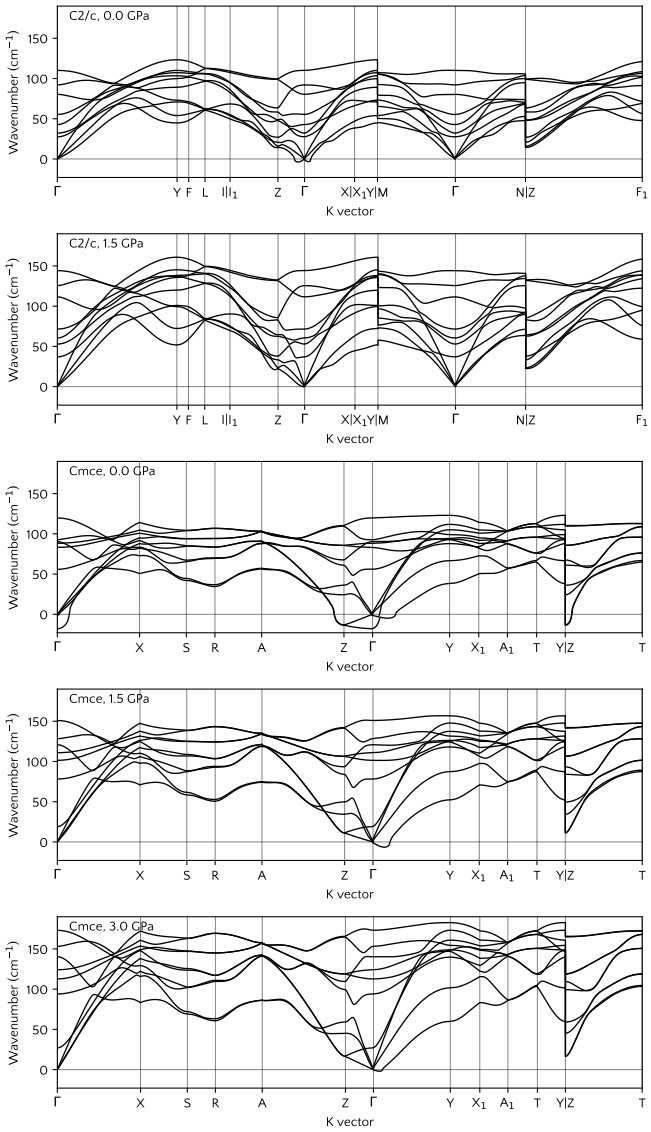

Figure C.5: Evolution with pressure of the phonon dispersion spectra of the librational modes for the fluorine $C2/c$ and $Cmce$ structures.

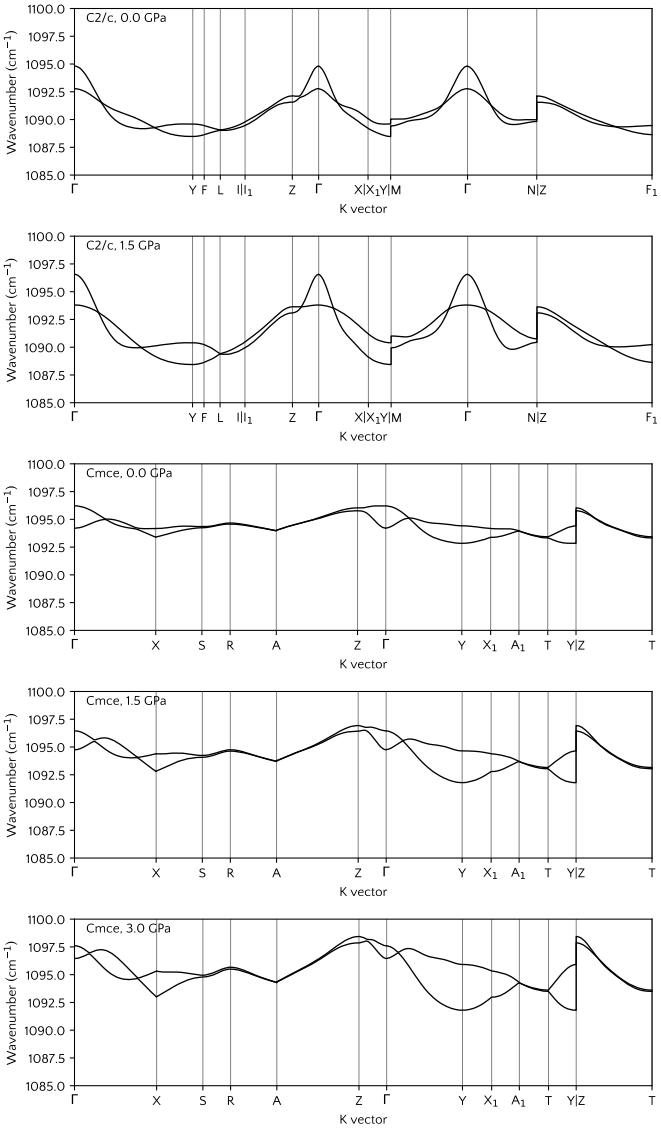

Figure C.6: Evolution with pressure of the phonon dispersion spectra of the vibrational modes for the fluorine C2/c and $Cmce$ structures.

C.5 Gradient of the energy along the unstable mode of the $Cmce$ at the Γ-point

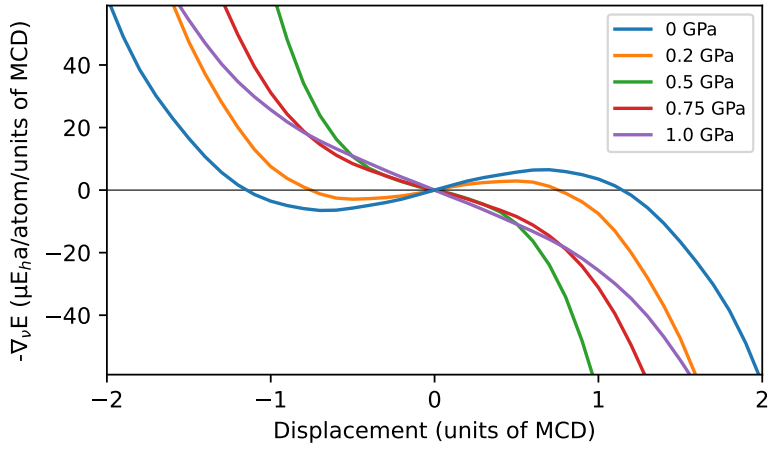

Figure C.7: Gradient of the potential energy with respect to displacement along the eigenvector *versus* displacement along the eigenvector of the Γ-point mode of imaginary frequency for the $Cmce$ fluorine structure at zero and 0.75 GPa.

Bibliography

Here are the references in citation order.

[1] G. L. Rech et al. 'Pressure-induced second-order phase transition in fluorine'. In: *Physical Chemistry Chemical Physics* 25 (2023), pp. 9935–9943. DOI: 10.1039/D2CP05635F (cited on page xvii).

[2] J. Ben et al. 'Thermal expansion of continuous random networks of carbon'. In: *Journal of Non-Crystalline Solids* 576 (2022), p. 121260. DOI: 10.1016/j.jnoncrysol.2021.121260 (cited on page xvii).

[3] L.M. Leidens et al. 'Different desorption rates prompting an indirect isotopic effect on nanoscale friction'. In: *Applied Surface Science Advances* 7 (2022), p. 100201. DOI: https://doi.org/10.1016/j.apsadv.2021.100201 (cited on page xvii).

[4] D. Cassol et al. 'Influence of an over calcined calcium oxide-based shrinkage-compensating admixture on some properties of a self-compacting concrete'. In: *Matéria (Rio de Janeiro)* 27 (2022). DOI: 10.1590/1517-7076-RMAT-2022-0171 (cited on page xviii).

[5] G. L. Rech et al. 'Fitting of interatomic potentials by a differential evolution algorithm'. In: *Computational Materials Science* 187 (2021), p. 109929. DOI: 10.1016/j.commatsci.2020.109929 (cited on page xviii).

[6] D. Matté et al. 'Molecular dynamics simulations of the isotopic effect on nanoscale friction'. In: *Applied Physics A* 127.9 (2021), p. 657. DOI: 10.1007/s00339-021-04803-3 (cited on page xix).

[7] G. L. Rech and C. A. Perottoni. 'Density functional theory plane-wave/pseudopotential calculations of the equation of state of rhenium in the terapascal regime'. In: *Journal of Physics: Conference Series* 1609.1 (2020), p. 012014. DOI: 10.1088/1742-6596/1609/1/012014 (cited on page xix).

[8] G. L. Rech, J. E. Zorzi, and C. A. Perottoni. 'Equation of state of hexagonal-close-packed rhenium in the terapascal regime'. In: *Physical Review B* 100.17 (2019), p. 174107. DOI: 10.1103/PhysRevB.100.174107 (cited on page xix).

[9] J. Emsley. *Nature's Building Blocks: An A-Z Guide to the Elements*. Oxford University Press, 2003, pp. 145–150 (cited on pages 1, 2).

[10] Georgius Agricola, Herbert Clark Hoover, and Lou Henry Hoover. *De Re Metallica: Translated from the First Latin Edition of 1556*. Dover, 1950 (cited on page 1).

[11] Henri Moissan. 'Action d'un courant électrique sur l'acide fluorhydrique anhydre'. In: *Comptes rendus hebdomadaires des sé, ances de l'Académie des sciences* 102 (1886), pp. 1543–1544 (cited on page 1).

[12] Thomas A O'Donnell. *The Chemistry of Fluorine: Comprehensive Inorganic Chemistry*. Vol. 5. Elsevier, 2017 (cited on page 1).

[13] *The nobel prize in chemistry 1906*. URL: https://www.nobelprize.org/prizes/chemistry/1906/summary/ (cited on page 1).

[14] William M Haynes. 'CRC handbook of chemistry and physics'. In: (2016) (cited on page 2).

[15] Truman H Jordan, William E Streib, and William N Lipscomb. 'Single-Crystal X-Ray Diffraction Study of β-Fluorine'. In: *The Journal of Chemical Physics* 41.3 (1964), pp. 760–764 (cited on page 2).

[16] David A Young. *Phase diagrams of the elements*. Univ of California Press, 1991 (cited on page 2).

[17] Lothar Meyer, CS Barrett, and Sandra C Greer. 'Crystal Structure of α-Fluorine'. In: *J. Chem. Phys.* 49.4 (1968), pp. 1902–1907 (cited on pages 2, 3, 47, 50).

[18] Linus Pauling, Ian Keaveny, and Arthur B Robinson. 'The crystal structure of α-fluorine'. In: *J. Solid State Chem.* 2.2 (1970), pp. 225–227 (cited on pages 2, 47).

[19] D Schiferl et al. 'Raman spectra and phase diagram of fluorine at pressures up to 6 GPa and temperatures between 10 and 320 K'. In: *J. Chem. Phys.* 87.5 (1987), pp. 3016–3021. DOI: 10.1063/1.453700 (cited on pages 2, 60, 61).

[20] David A. Young. *Phase diagrams of the elements*. Technical report. United States: Lawrence Livermore Laboratory, Sept. 1975. DOI: 10.2172/4010212 (cited on page 2).

[21] Michal H Kolar and Pavel Hobza. 'Computer modeling of halogen bonds and other σ-hole interactions'. In: *Chem. rev.* 116.9 (2016), pp. 5155–5187 (cited on page 3).

[22] Ludovic Troian-Gautier et al. 'Halide photoredox chemistry'. In: *Chem. Rev.* 119.7 (2019), pp. 4628–4683 (cited on page 3).

[23] Stefan Mattsson et al. 'The Crystal Structure of α-F_2: Solving a 50 Year Old Puzzle Computationally'. In: *Chem. Eur. J.* 25.13 (2019), pp. 3318–3324 (cited on pages 3, 51, 55, 71).

[24] Qianqian Lv et al. 'Crystal structures and electronic properties of solid fluorine under high pressure'. In: *Chin. Phys. B* 26.7 (2017), p. 076103 (cited on pages 4, 47, 48).

[25] C Shimomura et al. 'Structure analysis of high-pressure metallic state of iodine'. In: *Phys. Rev. B* 18.2 (1978), p. 715 (cited on page 4).

[26] Pedro Borlido et al. 'Large-scale benchmark of exchange–correlation functionals for the determination of electronic band gaps of solids'. In: *J. Chem. Theory Comput* 15.9 (2019), pp. 5069–5079 (cited on page 4).

[27] Mark A Olson et al. 'Prediction of chlorine and fluorine crystal structures at high pressure using symmetry driven structure search with geometric constraints'. In: *J. Chem. Phys.* 153.9 (2020), p. 094111 (cited on page 4).

[28] Defang Duan et al. 'Multistep dissociation of fluorine molecules under extreme compression'. In: *Phys. Rev. Lett* 126.22 (2021), p. 225704 (cited on page 5).

[29] Christian Tantardini, Faridun N Jalolov, and Alexander G Kvashnin. 'Crystal Structure Evolution of Fluorine under High Pressure'. In: *The Journal of Physical Chemistry C* 126.27 (2022), pp. 11358–11364 (cited on pages 5, 47, 48).

[30] Sergei I Ivlev et al. 'The Crystal Structures of α-and β-F_2 Revisited'. In: *Chem. Eur. J.* 25.13 (2019), pp. 3310–3317 (cited on pages 5, 42, 47).

[31] Stefan Grimme et al. 'A consistent and accurate ab initio parametrization of density functional dispersion correction (DFT-D) for the 94 elements H-Pu'. In: *J. Chem. Phys.* 132.15 (2010), p. 154104 (cited on pages 5, 41).

[32] Jonas Moellmann and Stefan Grimme. 'DFT-D3 study of some molecular crystals'. In: *J. Phys. Chem. C* 118.14 (2014), pp. 7615–7621 (cited on pages 5, 41).

[33] WMC Foulkes et al. 'Quantum Monte Carlo simulations of solids'. In: *Rev. Mod. Phys.* 73.1 (2001), p. 33 (cited on pages 5, 43).

[34] Luke Shulenburger and Thomas R. Mattsson. 'Quantum Monte Carlo applied to solids'. In: *Phys. Rev. B* 88 (24 Dec. 2013), p. 245117. DOI: 10.1103/PhysRevB.88.245117 (cited on page 5).

[35] N. D. Drummond, M. D. Towler, and R. J. Needs. 'Jastrow correlation factor for atoms, molecules, and solids'. In: *Phys. Rev. B* 70 (23 Dec. 2004), p. 235119. DOI: 10.1103/PhysRevB.70.235119 (cited on pages 6, 43).

[36] Andrea Zen et al. 'Fast and accurate quantum Monte Carlo for molecular crystals'. In: *Proc. Natl. Acad. Sci. U.S.A.* 115.8 (2018), pp. 1724–1729 (cited on page 6).

[37] R.G. Littlejohn. *Physics 221AB - Quantum Mechanics, University of California, Berkeley*. https://bohr.physics.berkeley.edu/classes/221/1920/221.html. Accessed: 2023-05-06. 2022 (cited on page 10).

[38] Pierre Hohenberg and Walter Kohn. 'Inhomogeneous electron gas'. In: *Physical review* 136.3B (1964), B864 (cited on page 23).

[39] Wolfram Koch and Max C Holthausen. *A chemist's guide to density functional theory*. John Wiley & Sons, 2015 (cited on page 23).

[40] Walter Kohn and Lu Jeu Sham. 'Self-consistent equations including exchange and correlation effects'. In: *Phys. Rev.* 140.4A (1965), A1133 (cited on pages 24, 28).

[41] Ralf Stowasser and Roald Hoffmann. 'What do the Kohn-Sham orbitals and eigenvalues mean?' In: *J. Am. Chem. Soc.* 121.14 (1999), pp. 3414–3420 (cited on page 25).

[42] John P Perdew and Yue Wang. 'Accurate and simple analytic representation of the electron-gas correlation energy'. In: *Physical review B* 45.23 (1992), p. 13244 (cited on page 28).

[43] John P Perdew, Kieron Burke, and Yue Wang. 'Generalized gradient approximation for the exchange-correlation hole of a many-electron system'. In: *Physical review B* 54.23 (1996), p. 16533 (cited on page 28).

[44] John P Perdew, Kieron Burke, and Yue Wang. 'Erratum: Generalized gradient approximation for the exchange-correlation hole of a many-electron system [Phys. Rev. B 54, 16 533 (1996)]'. In: *Physical Review B* 57.23 (1998), p. 14999 (cited on page 28).

[45] John P Perdew, Matthias Ernzerhof, and Kieron Burke. 'Rationale for mixing exact exchange with density functional approximations'. In: *J. Chem. Phys.* 105.22 (1996), pp. 9982–9985 (cited on pages 28, 41).

[46] Stefan Grimme et al. 'Dispersion-corrected mean-field electronic structure methods'. In: *Chem. Rev.* 116.9 (2016), pp. 5105–5154 (cited on pages 29, 41).

[47] Stefan Grimme, Stephan Ehrlich, and Lars Goerigk. 'Effect of the damping function in dispersion corrected density functional theory'. In: *J. Comput. Chem.* 32.7 (2011), pp. 1456–1465 (cited on pages 29, 30, 41).

[48] Antti J Karttunen, Tommi Tynell, and Maarit Karppinen. 'Atomic-level structural and electronic properties of hybrid inorganic–organic ZnO: hydroquinone superlattices fabricated by ALD/MLD'. In: *J. Phys. Chem. C* 119.23 (2015), pp. 13105–13114 (cited on page 41).

[49] Carlo Adamo and Vincenzo Barone. 'Toward reliable density functional methods without adjustable parameters: The PBE0 model'. In: *J. Chem. Phys.* 110.13 (1999), pp. 6158–6170 (cited on page 41).

[50] Axel D Becke. 'A multicenter numerical integration scheme for polyatomic molecules'. In: *J. Chem. Phys.* 88.4 (1988), pp. 2547–2553 (cited on page 42).

[51] R Dovesi et al. 'CRYSTAL17 User's Manual'. In: (2018) (cited on pages 42, 43, 55, 56).

[52] R J Needs et al. 'Continuum variational and diffusion quantum Monte Carlo calculations'. In: *J. Phys.: Condens. Matter* 22.2 (2010), p. 023201. DOI: 10.1088/0953-8984/22/2/023201 (cited on page 43).

[53] See https://casinoqmc.net/pseudo_lib/f/2/pp_crystal (cited on page 43).

[54] See https://casinoqmc.net/pseudo_lib/f/2/f_tnbasis_crystal.txt (cited on pages 43, 71).

[55] Jiawei Xu et al. 'Correlation Consistent Gaussian Basis Sets for H, B–Ne with Dirac–Fock AREP Pseudopotentials: Applications in Quantum Monte Carlo Calculations'. In: *J. Chem. Theory Comput.* 9.5 (2013), pp. 2170–2178 (cited on pages 43, 71).

[56] Wahyu Setyawan and Stefano Curtarolo. 'High-throughput electronic band structure calculations: Challenges and tools'. In: *Comput. Mater. Sci.* 49.2 (2010), pp. 299–312 (cited on page 44).

[57] Hendrik J Monkhorst and James D Pack. 'Special points for Brillouin-zone integrations'. In: *Phys. Rev. B: Condens. Matter* 13.12 (1976), p. 5188 (cited on page 44).

[58] TM Niemczyk, RR Getty, and GE Leroi. 'Vibrational spectra of solid fluorine'. In: *J. Chem. Phys.* 59.10 (1973), pp. 5600–5604 (cited on page 50).

[59] Mihail Bogojeski et al. 'Quantum chemical accuracy from density functional approximations via machine learning'. In: *Nat. Commun.* 11.1 (2020), pp. 1–11 (cited on page 50).

[60] Francis Birch. 'Finite elastic strain of cubic crystals'. In: *Phys. Rev.* 71.11 (1947), p. 809 (cited on page 52).

[61] Ross J. Angel, Matteo Alvaro, and Javier Gonzalez-Platas. 'EosFit7c and a Fortran module (library) for equation of state calculations'. In: *Z. Krist. Cryst. Mater.* 229.5 (2014), pp. 405–419. DOI: 10.1515/zkri-2013-1711 (cited on page 52).

[62] Jan Řezáč. 'Description of halogen bonding in semiempirical quantum-mechanical and self-consistent charge density-functional tight-binding methods'. In: *J. Comput. Chem* 40.17 (2019), pp. 1633–1642 (cited on pages 57, 58).

[63] H. T. Stokes, D. M. Hatch, and B. J. Campbell. *ISOSUBGROUP, ISOTROPY Software Suite*. https://iso.byu.edu. (cited on page 58).

[64] Harold T Stokes and Dorian M Hatch. 'COPL: program for obtaining a complete list of order parameters for a group-subgroup crystalline phase transition'. In: *J. Appl. Crystallogr.* 35.3 (2002), pp. 379–379 (cited on page 58).

[65] Dorian M Hatch and Harold T Stokes. 'Complete listing of order parameters for a crystalline phase transition: A solution to the generalized inverse Landau problem'. In: *Phys. Rev. B: Condens. Matter* 65.1 (2001), p. 014113 (cited on page 58).

[66] E K H Salje. *Phase Transitions in Ferroelastic and Co-elastic Crystals: An Introduction for Mineralogists, Material Scientists and Physicists*. Cambridge University Press, 1990 (cited on page 59).

[67] Michael A Carpenter, E K H Salje, and Ann Graeme-Barber. 'Spontaneous strain as a determinant of thermodynamic properties for phase transitions in minerals'. In: *Eur. J. Mineral.* (1998), pp. 621–691 (cited on page 59).